

Experimental Quantification of the Variability of the Raindrop Size Distribution at Small Scales

THÈSE N° 5271 (2012)

PRÉSENTÉE LE 17 FÉVRIER 2012

À LA FACULTÉ DE L'ENVIRONNEMENT NATUREL, ARCHITECTURAL ET CONSTRUIT
LABORATOIRE DE TÉLÉDÉTECTION ENVIRONNEMENTALE
PROGRAMME DOCTORAL EN ENVIRONNEMENT

ÉCOLE POLYTECHNIQUE FÉDÉRALE DE LAUSANNE

POUR L'OBTENTION DU GRADE DE DOCTEUR ÈS SCIENCES

PAR

Joël JAFFRAIN

acceptée sur proposition du jury:

Prof. M. Parlange, président du jury
Prof. A. Berne, directeur de thèse
Dr U. Germann, rapporteur
Dr P. Molnar, rapporteur
Prof. J. A. Smith, rapporteur



ÉCOLE POLYTECHNIQUE
FÉDÉRALE DE LAUSANNE

Suisse
2012

It is a truism that wherever there is no precipitation,
there is also not much of a hydrological cycle.
— Wilfried Brutsaert, *Hydrology An Introduction* (2005)

To my parents and my future wife...

Acknowledgements

I am used to compare a PhD to a marathon so that to finish both, you need to be strongly motivated, to run fast enough to be competitive and to keep in mind that you need to be able to reach the end of the race. I have started my "marathon" in September 2007 and as the first PhD student arrived in the Laboratoire de Télédétection Environnementale (LTE), I am proud today to see that I have actively taken part in the development of our lab. This work, like many others, will not have been possible without the support from many people.

First of all, I would like to express my deep thanks to my PhD advisor Alexis Berne for his trust during these 4 years. Despite an "all the days" busy schedule, he has always found the time required to follow and discuss my work, providing important comments that considerably help reaching a high degree of quality. Many thanks as well to Marc Schleiss, a colleague, friend and roommate during the conferences, for his help for the deployment of the sensors, his grateful discussions on DSD measurement issues and of course for all these nice and funny moments shared during conferences.

The design and the set up of a network of disdrometers, which is the first of its kind, would not have been possible without our electronical engineer André Studzinski, who can be seen as the "father of the network". It was a pleasure to work with André on this project, and I would like to thank him for his involvement, his patience, his happiness and our interesting discussions on the improvement of data acquisition and transmission. Another key person in the realization of this network is Flavio Comino, the mechanical engineer. The great quality and precision of his work always made as fast as possible is greatly acknowledge. The help of Florian Pantillon and Yann Chavaillaz, i.e., short term LTE collaborators (civil service), in the maintenance of the network was greatly appreciated.

Furthermore, I would like to strongly acknowledge here the members of my comity, namely: Marc Parlange (EPFL-EFLUM), James Smith (Princeton University), Urs Germann (MeteoSwiss) and Peter Molnar (ETHZ), for there availability to evaluate this work and their helpful comments and discussions that help to improve its quality.

Special thanks are dedicated to all the past and actual members of the LTE: Alexis, Alina, André, Blandine, Dany, Florian, Jacopo, Marc 1, Marc 2, Samuel, Tobias, Xavier and Yann, that make every day this place so pleasant to work. On the same way, thanks to the "corridor's colleagues"

Acknowledgements

for the coffee breaks that help to stay awake during these long working hours. In particular, I would like to mention Jéré (who was as well my previous roommate) and Quentin, which one is always in to have a beer. Thanks a lot for these long Friday evenings at the nearby Satellite bar (even if we have missed couple of times the last metro...).

On a more personal point of view, I would like to thanks my family for the constant support and in particular my parents and grandparents for teaching me basic qualities that help me to successfully fulfill this PhD, e.g., the will, the motivation and the perseverance. A special thank is dedicated here to my father with who I learned the basic notions of electronic that were intensively used in this project. In addition, as I am not the first one in the family to obtain a PhD degree, I have really benefited from the experience and the useful comments from my older brother Jérôme (also called Jay). With these few lines Jay, thanks a lot for your advertisements even if (unfortunately) I did not follow all of them (e.g., "do not stop practicing sport..."). Thanks to my younger brother Johann ("Juan") for the organization of the airsoft parties which considerably helped to sweep out the stress.

Finally, as the PhD deadline was approaching, the stress and the working hours increased considerably. For this, and of course for all the additional related annoyances, I need to acknowledge herein the patience of my future wife Marina. Her comforting words and her happiness have strongly helped to keep on my motivation. Many thanks for being part of that.

Financial support:



FONDS NATIONAL SUISSE
SCHWEIZERISCHER NATIONALFONDS
FONDO NAZIONALE SVIZZERO
SWISS NATIONAL SCIENCE FOUNDATION

The author greatly acknowledges financial support (grants 200021-118057/1 and 200020-132002) from the Swiss National Science Foundation (SNSF).

Lausanne, 15th of January 2012

J. J.

Remerciements

J'ai pour habitude de comparer la thèse de doctorat à un marathon car les deux nécessitent une forte motivation, un esprit de compétition et de garder à l'esprit que vous devez être en mesure de passer la ligne d'arrivée. J'ai commencé mon "marathon" en septembre 2007 au sein du Laboratoire de Télédétection Environnementale (LTE) de l'Ecole Polytechnique Fédérale de Lausanne (EPFL). Étant le premier doctorant arrivé au sein du laboratoire, je suis fier aujourd'hui d'avoir contribué à son développement. Ce travail, comme beaucoup d'autres, n'aurait pas été possible sans le soutien et la collaboration de nombreuses personnes.

Tout d'abord, je tiens à exprimer mes plus profonds remerciements à mon directeur de thèse, Alexis Berne, pour la confiance qu'il m'a accordé au cours de ces 4 années. Malgré un emploi du temps plus que chargé, il a toujours trouvé le temps nécessaire pour suivre et discuter mon travail. Ses commentaires ont permis d'atteindre un niveau de qualité élevé. Merci à mon collègue, ami et colocataire de chambre lors des conférences, Marc Schleiss pour son aide lors du déploiement des instruments, ses discussions sur les problèmes liés à la mesure de la granulométrie des pluies et bien sûr pour ces moments partagés lors des conférences.

La conception et la réalisation d'un réseau de disdromètres, le premier de son type, n'aurait pas été possible sans notre ingénieur électronicien André Studzinski qui peut être vu comme le "père du réseau". J'ai grandement apprécié de travailler à ses côtés sur ce projet et je souhaite donc vivement le remercier pour son investissement, sa patience, sa bonne humeur et pour nos longues discussions sur l'amélioration de notre système d'acquisition de données. Une autre personne clé sur cet aspect technique est notre ingénieur mécanicien Flavio Comino qui se doit d'être remercier pour son travail de qualité, toujours d'une précision stupéfiante dans un laps de temps très court. Enfin, l'aide de Florian Pantillon et Yann Chavaillaz, ayant tous deux fait leur service civile au sein de notre labo, pour la maintenance du réseau a été grandement appréciée.

C'est avec grand plaisir que j'adresse mes remerciements aux différents membres de mon comité, à savoir, Marc Parlange (EPFL-EFLUM), James Smith (Université de Princeton), Urs Germann (MeteoSuisse) et Peter Molnar (École Polytechnique de Zurich-ETHZ), pour le temps consacré à évaluer ce travail ainsi que leurs commentaires et discussions.

J'adresse toute ma gratitude aux membres (actuel et passé) du LTE, à savoir : Alexis, Alina,

Remerciements

André, Blandine, Dany, Florian, Jacopo, Marc 1, Marc 2, Samuel, Tobias, Xavier et Yann, qui ont fait de cet endroit une place où il est si plaisant de travailler. Je ne peux évidemment pas oublier les (nombreux) "collègues de couloir" pour les pauses café qui ont permis de rester éveillé pendant ces longues heures de travail (pas uniquement en fin de thèse). En particulier, je tiens à mentionner Jérémy (également mon ancien colocataire) et Quentin, lequel se dévoue toujours pour venir boire une bière (entre autre) à vos côtés. Merci à vous deux pour ces longues soirées du vendredi au bar Satellite (même si nous avons raté plusieurs fois le dernier métro...).

Sur un plan plus personnel, je souhaite remercier ma famille pour le soutien constant au cours de ces 4 années et en particulier mes parents (Denise et Yves) et mes grands-parents (Françoise et Charles) pour m'avoir inculqué des qualités telles que, entre autre, la volonté, la motivation et la persévérance, qui m'ont aidé à achever avec succès cette thèse. J'adresse un petit clin d'oeil à mon père avec qui j'ai appris les bases de l'électronique qui ont été largement mises à contribution dans ce projet. De plus, n'étant pas le premier de la famille à obtenir une thèse, j'ai bénéficié de l'expérience et des commentaires de mon grand frère Jérôme (surnommé "Jay"). Jay, par ces quelques lignes, je te remercie pour tes mises en garde judicieuses même si (malheureusement) je ne les ai pas toutes suivies (par exemple "n'arrête pas la pratique du sport, surtout en fin de thèse..."). Merci à mon petit frère Johann ("Juan") pour l'organisation de nos parties d'airsoft qui ont considérablement aidé à évacuer le stress.

Enfin, il est vrai qu'avec la fin de thèse approchante, le stress et les horaires de travail ont augmenté. Merci à ma "moitié" (et future femme) Marina pour sa patience et son soutien de tous les jours. Ses mots réconfortants et sa joie de vivre m'ont fortement aidé à garder ma motivation.

Support financier :



FONDS NATIONAL SUISSE
SCHWEIZERISCHER NATIONALFONDS
FONDO NAZIONALE SVIZZERO
SWISS NATIONAL SCIENCE FOUNDATION

L'auteur tient à exprimer toute sa gratitude au Fond National Suisse pour le support financier (bourses 200021-118057/1 et 200020-132002).

Lausanne, 15 janvier 2012

J. J.

Abstract

Reliable quantitative precipitation estimation is crucial to better understand and eventually prevent water-related natural hazards (floods, landslides, avalanches, ...). Because rainfall is highly variable in time and space, precipitation monitoring and forecasting is a complex task. In addition, the variability of rainfall at small scales (for instance within the radar pixel) is still poorly understood. Knowledge of the rain drop size distribution (DSD) is of primary concern for precipitation estimation and in particular weather radar.

To better understand the variability of the DSD at small scales, a network of optical disdrometers (Parsivel) has been designed and set up. The instruments are fully autonomous in term of power supply and data transmission. The network of 16 disdrometers has been deployed over a typical operational weather radar pixel ($1 \times 1 \text{ km}^2$) in Lausanne, Switzerland, for 16 months collecting DSD data at a high temporal resolution (30 s).

The sampling uncertainty associated with Parsivel measurements has been quantified for different quantities related to the DSD, using a 15-month data set collected by two collocated disdrometers.

Using a geostatistical approach, and in particular variograms, the spatial structure of quantities related to the DSD has been quantified. The analyses have been conducted on 36 rainfall events that have been grouped according to three types of rainfall (i.e., convective, transitional and frontal). It shows a significant variability, i.e., larger than the one induced by the sampling process, of the different quantities of interest. The observed spatial structure is significant for temporal resolution below 30 min from which it is difficult to distinguish between the natural variability and the one induced by the sampling process.

The impact of the observed variability of the DSD on radar rainfall estimators is investigated focusing on two different radar power laws (the classical Z - R law for conventional radar and the R - K_{dp} law for polarimetric radar). The parameters of the power laws are estimated at different spatial scales: at the single station scale, at the aggregate of stations scale (aggregate of point measurements) and at the pixel area scale (average over all the stations). First, it shows clear distinct groups of power law parameters according to the type of rainfall. Moreover, the observed variability of these parameters is significantly larger than the variability induced by the sampling process of the instruments. The observed variability in power law parameters can be responsible for deviation in terms of rain amounts at the single station scale ranging from -5 to +15% the one estimated at the pixel (average) scale.

Abstract

The original contributions in this work are: (1) the design and deployment of an innovative network of autonomous disdrometers Parsivel over a typical operational weather radar pixel (1 km^2), (2) the quantification of the sampling uncertainty associated with Parsivel measurements, (3) the quantification of the spatial variability of different quantities related to the DSD within this typical radar pixel and (4) the quantification of the influence of this spatial variability of the DSD on radar rainfall estimation (for conventional and polarimetric radar).

For illustration, the results are important: (i) to illustrate the added value of the network of disdrometer that has been designed and the interest for various environmental fields (meteorology, hydrology, risks of water-related natural hazards, ...), (ii) for a better knowledge of the spatial variability of the DSD at different scales which should helps improving radar rainfall estimation, (iii) for the quantification of the errors associated with the extension of relationships derived at a specific location to larger domains (e.g., pixel) and (iv) for the ground validation of numerical weather model.

KEYWORDS: raindrop size distribution, network of disdrometers, variability of precipitation, spatial structure of rainfall, radar rainfall estimation, spatial representativity.

Résumé

Des estimations fiables des précipitations sont d'une importance capitale afin de mieux comprendre et éventuellement de mieux prévenir les événements extrêmes liés à l'eau (inondations, glissements de terrain, avalanches, ...). Du fait de la variabilité des précipitations dans le temps et dans l'espace, la mesure et la prévision des pluies sont des tâches complexes, d'autant que la variabilité des pluies est toujours mal connue à petite échelle (par exemple, à l'échelle de la maille radar). Une meilleure connaissance de la variabilité de la granulométrie des pluies (DSD en anglais) est cruciale pour les estimations des pluies par les radars météorologiques.

Afin de mieux comprendre la variabilité de la granulométrie des pluies à petite échelle, un réseau de disdromètres optiques (Parsivel) a été développé et construit. Les instruments sont totalement autonomes en terme d'alimentation et de transfert de données. Le réseau de 16 instruments a été déployé à Lausanne, Suisse, couvrant une surface d'environ $1 \times 1 \text{ km}^2$ correspondant à une maille de radar opérationnel. Le réseau a collecté des mesures de la granulométrie des pluies à haute résolution temporelle (30 s) pendant 16 mois.

Afin d'obtenir des analyses fiables, l'incertitude d'échantillonnage associée à la mesure du Parsivel a été quantifiée à partir d'un jeu de données collecté par deux instruments co-localisés sur une durée de 15 mois.

La *structure spatiale*¹ de différentes quantités reliées à la granulométrie des pluies est quantifiée en utilisant une approche géostatistique (i.e., variogrammes). Une sélection de 36 événements pluvieux, lesquels ont été groupé en fonction de 3 types d'évènement (i.e., convectif, transitionnel et frontal), est utilisée pour les analyses. Ces dernières montrent une variabilité significative, c'est à dire plus grande que celle induite par le processus d'échantillonnage, pour des résolutions temporelles inférieures à 30 min. Pour des pas de temps supérieurs à 30 min, la distinction n'est plus possible entre la variabilité naturelle et celle induite par le processus d'échantillonnage.

L'impact de cette variabilité sur les estimations des pluies au moyen des radars météorologiques est également analysé. Deux lois sont considérées : la relation $Z-R$ pour les radars conventionnels et la relation $R-K_{dp}$ pour les radars polarimétriques. Les paramètres de ces deux relations sont calculés à différentes résolutions spatiales : (i) pour chaque instrument (mesure ponctuelle), (ii) pour un ensemble constitué des mesures de tous les instruments

¹on parle de structure spatiale dans un jeu de données lorsque ces données montrent une organisation dans l'espace et non pas une distribution aléatoire.

Résumé

(agrégat de points) et *(iii)* pour la maille radar (moyenne de tous les instruments). Les analyses montrent, dans un premier temps, une nette distinction des valeurs obtenues en fonction du type d'évènement. De plus, la variabilité observée dans les paramètres calculés pour ces 2 lois est plus forte que celle induite par l'échantillonnage. Enfin, cette variabilité peut se traduire, en terme de cumul de pluie, par des erreurs d'estimation de l'ordre de -5 à +15%.

Les contributions principales de ce travail sont : (1) la conception et la réalisation d'un réseau de disdromètres autonomes et son déploiement sur une maille typique d'un radar opérationnel, (2) la quantification de l'erreur d'échantillonnage associée à la mesure du Parsivel, (3) la quantification de la variabilité spatiale de la granulométrie des pluies sur une maille radar et (4) l'influence de cette variabilité sur les estimations radar au moyen de lois puissances tel que la loi $Z-R$ (radar conventionnel) et la loi $R-K_{dp}$ (radar polarimétrique).

Les résultats présentés sont importants, entre autre, pour : *(i)* démontrer le potentiel de ce réseau de disdromètres pour différentes disciplines environnementales (météorologie, hydrologie, étude des évènements extrêmes liés à l'eau, ...), *(ii)* une meilleure compréhension de la variabilité de la granulométrie des pluies à différentes échelles dans le but d'améliorer la mesure des pluies, *(iii)* la quantification de l'erreur associée au changement de support (de l'échelle ponctuelle à l'échelle d'une maille radar) et *(iv)* la validation au sol de modèles de prévision des pluies.

MOTS CLÉS : granulométrie des pluies, réseau de disdromètres, variabilité des précipitations, structure spatiale des pluies, estimation radar, représentativité spatiale

Contents

Acknowledgements	v
Remerciements	vii
Abstract (English/Français)	ix
List of figures	xx
List of tables	xxi
List of symbols	xxiii
List of acronyms	xxvii
1 Introduction	1
1.1 Rationale	1
1.2 Precipitation microphysics	2
1.3 The concept of raindrop size distribution	3
1.4 Radar precipitation estimation	5
1.5 State-of-the-art	7
1.6 Objectives	10
2 A network of autonomous disdrometers	13
2.1 Introduction	13
2.2 Parsivel disdrometer	14
2.3 Autonomous station	16
2.4 Network	17
2.5 Data management	19
2.6 Applications	19
2.6.1 Method and Data Set	20
2.6.2 Sampling uncertainty	22
2.6.3 Variability of quantities related to the DSD	23
2.7 Summary and Conclusion	27

3	Sampling uncertainty	29
3.1	Introduction	29
3.2	Experimental Setup	30
3.3	Comparison between optical disdrometers and tipping-bucket rain gauges	36
3.4	Quantification of the sampling uncertainty	39
3.4.1	Integral quantities related to the DSD	39
3.4.2	Method	40
3.4.3	Sampling uncertainty associated with total drop concentration estimates	44
3.4.4	Sampling uncertainty associated with median-volume diameter estimates	44
3.4.5	Sampling uncertainty associated with rain rate estimates	45
3.4.6	Sampling uncertainty associated with radar reflectivity estimates	47
3.4.7	Sampling uncertainty associated with differential reflectivity estimates	50
3.5	Conclusion	52
4	Spatial structure of the DSD at the radar subgrid scale	55
4.1	Introduction	55
4.2	Experimental set up and data set	56
4.3	Methods	59
4.3.1	Framework and Assumptions	59
4.3.2	Variogram estimation	61
4.3.3	Spatial correlation estimation	62
4.4	Results	64
4.4.1	Spatial correlations	64
4.4.2	Variograms	65
4.5	Applications: the spatial representativity issues	69
4.6	Conclusion	73
5	Influence on radar rainfall estimators	75
5.1	Introduction	75
5.2	Experimental set up and data set	76
5.3	Methods	77
5.3.1	Pre-processing	77
5.3.2	R , Z and K_{dp} calculation	77
5.3.3	Power-law fitting	78
5.3.4	Sampling uncertainties	80
5.4	Results	80
5.4.1	Z - R relationships	80
5.4.2	R - K_{dp} relationships	81
5.4.3	Impacts on rain amount estimation	83
5.4.4	Influence of the temporal resolution	84
5.5	Summary and conclusion	86

6 Perspectives and additional field campaigns	89
6.1 Introduction	89
6.2 Variability of the DSD for Mediterranean region	89
6.3 Variability of the DSD as a function of the altitude	92
6.4 The use of commercial microwave links for rainfall monitoring in urban area .	93
7 Summary and Conclusions	97
A Electronic diagram: Solar control	103
B Electronic diagram: Station power control	105
C Electronic diagram: RS485 to RS232TTL converter	107
D Electronic diagram: FIFO	109
E Calculation of the relative sampling uncertainty	111
F Experimental values of the sampling uncertainty	113
Bibliography	126
Curriculum Vitae	127

List of Figures

1.1	A static picture of the microstructure of rainfall.	4
1.2	Global daily merged precipitation for January (top) and July (bottom). These maps are from the Global Precipitation Climatology Project (GPCP) Monthly rainrate climatology [Huffman et al., 2001]. source: http://precip.gsfc.nasa.gov/	8
2.1	The optical disdrometer Parsivel [®] (OTT). The measuring principle is based on laser attenuation when a particle crosses the beam.	15
2.2	A wireless autonomous station for DSD measurement. The station consists of a Parsivel, an electronic unit managing power and data transmission, a battery and a solar panel.	16
2.3	The network of 16 Parsivels deployed over EPFL campus ($\sim 1 \times 1 \text{ km}^2$) in Lausanne, Switzerland.	18
2.4	Top: mean rain rate over the 16 stations of the network at a 30 s temporal resolution for the selected rain period. Bottom: corresponding mean (black) and individual (grey) rain amounts.	21
2.5	DSD spectrum integrated over the selected period. The points figures the center of Parsivel diameter classes.	22
2.6	Coefficient of variation (CV) of N_t as a function of the mean N_t values (\bar{N}_t) for the selected rain period. Blue lines figure the sampling uncertainty associated with CV values. Red lines figure the one associated with \bar{N}_t values. When the sampling uncertainty in CV and \bar{N}_t is below 0.1%, the error bars are not visible.	25
2.7	Same as Figure 2.6 for D_m	26
2.8	Same as Figure 2.6 for R	26
3.1	The experiment involves two parallel Parsivels (right), two TB rain gauges (in white in the bottom left corner of the picture) and a weather station (center). Parsivel 01 is the closest to the solar panel while Parsivel 02 is the closest to TB rain gauges. The third disdrometer (Parsivel 03), perpendicular to the others, was later deployed in order to investigate the effect of wind on Parsivel measurements.	31
3.2	Rain rate differences between Parsivel 01 and 03 as a function of wind speed (top) and wind direction (bottom). The dashed line figures the linear regression.	32

List of Figures

3.3 Scatterplot of the rain rate provided by Parsivel 01 (R) versus the one derived from the DSD (R') at a 300-s temporal resolution. The dashed (solid) line figures the 1-1 (regression) line. 34

3.4 Mean rain rate (top) for each type of instruments. Cumulative rain amounts (bottom) recorded by each Parsivel and each TB rain gauge. Both plots correspond to a temporal resolution of 300 s over the 15 months of the experiment. 35

3.5 300-s DSD spectrum of each disdrometer averaged over the 15 months of the experiment. The X axis corresponds to the drop diameter using the center of Parsivel classes. The Y axis is the number of drops in log scale. 36

3.6 Scatterplot of the rain rate recorded by Parsivel 01 and 02 (top) and comparison of rain rates recorded by Parsivel 01 and TB rain gauge 02 at a temporal resolution of 300 s. 38

3.7 Differences between rain rate values recorded by the two Parsivels ($R_{01} - R_{02}$) over the 15 months at a temporal resolution of 300 s. 39

3.8 Distribution of $\epsilon_i(D_0)$ values for D_0 between 0.6 and 0.7 mm at a temporal resolution of 60 s. Solid vertical line represents the mean while dashed vertical lines represents the 10% and 90% quantiles. 42

3.9 Relative sampling uncertainty [-] as a function of the number of collocated disdrometers and the temporal resolution for R values between 0.1 and 2 mm h⁻¹. The number of collocated instrument has a significant impact on $\sigma_{\epsilon_{S_k}}$ (top) while the relative uncertainty σ_{ω}^r does not significantly depend on the number of sensors deployed (bottom). 43

3.10 Relative sampling uncertainty associated with estimates of total concentration of drops from a single Parsivel as a function of total drop concentration and temporal resolution. The white area corresponds to pixels with less than 30 values to estimate $\sigma_{\omega(N_i)}^r$. X-axis is logarithmic. Note that the color scale stops at 0.30 while contour lines figures the whole range of values. 45

3.11 Same as Figure 3.10 for the median-volume diameter estimated from a single Parsivel. 46

3.12 Median of the number of drops with $D > D_0$ measured by both Parsivels over the 15 months as a function of D_0 classes. N depends on the sampling area (54 cm²) and the considered temporal resolution (here 60 s). 47

3.13 Same as Figure 3.10 for rain rate measurements of a single Parsivel (top) and a single TB rain gauge (bottom). 48

3.14 Median of the number of drops measured by both Parsivels (top) and mean diameter [mm] (bottom) over the 15 months as a function of R classes. N depends on the sampling area (54 cm²) and the considered temporal resolution (here 60 s). For consistency with Figure 3.13, statistical descriptors associated with classes characterized by less than 30 measurements are not drawn. 49

3.15 Same as Figure 3.10 for the radar reflectivity at horizontal polarization estimated from a single Parsivel at X-band. 50

3.16 Same as Figure 3.14 for Z_h 51

3.17	Same as Figure 3.10 for the differential reflectivity estimated from a single Parsivel at X-band.	52
3.18	Same as Figure 3.14 for Z_{dr}	53
4.1	Radar rain-rate map to illustrate a convective (top) and a frontal (bottom) rainfall event. The black and white cross (at about X=530 km and Y=150 km) denotes the position of the network of disdrometers.	57
4.2	Drop size spectra integrated over all events within each group of rainfall types (i.e., convective, transitional and frontal). The symbols indicate the center of Parsivel diameter classes.	58
4.3	Distribution of \bar{R} values (i.e., averaged over the network) in linear space (top) and logarithmic space (bottom) for the convective rainfall group.	60
4.4	Spatial correlation $\rho(h)$ (\circ) and associated empirical model $\hat{\rho}(h)$ (solid line) for R for the convective rainfall types at a 60-s temporal resolution.	63
4.5	Sample variogram and fitted linear variogram model for N_t for the three rainfall types at a 60-s temporal resolution. The units associated with $\gamma(h)$ are m^{-6} . The X axis shows the interdistance h classes (m).	65
4.6	Same as Figure 4.5 for D_m . The units associated with $\gamma(h)$ are mm^2	67
4.7	Same as Figure 4.5 for R . The units associated with $\gamma(h)$ are $mm^2 h^{-2}$	67
4.8	Influence of the temporal resolution on the nugget (top) and slope (bottom) parameters of the linear variogram model for the different types of rainfall. . .	69
4.9	Same as Figure 4.8 for D_m	70
4.10	Same as Figure 4.8 for R	71
4.11	Standard deviation of σ_{ϵ_i} for N_t (top), D_m (middle) and R (bottom) as a function of domain size at a 60-s temporal resolution. X axes present the length of the side of the considered square domain.	72
5.1	Z - R scatterplot from Station 10 for the transitional period at C-band at a 60-s temporal resolution. Blue crosses (red circles) denote time steps during which at least one drop in the diameter class centered on 6.5 (5.5) mm has been recorded.	78
5.2	Z_A - R_A scatterplot and the fitted Z_A - R_A (solid line) and R_A - Z_A (dashed line) relationships for the transitional rainfall type at C-band and at a 60-s temporal resolution.	79
5.3	Fitted a and b parameters of the Z - R (top) and R - Z (bottom) relationships for the convective (circles), transitional (diamonds) and frontal (triangles) types of rainfall at C-band and at a 60-s temporal resolution. Dotted lines figure the associated uncertainty. The A (P) point denotes the a and b values at the pixel (aggregate of points) scale.	81
5.4	Same as Figure 5.3 for the c and d parameters of the R - K_{dp} relationship at C-band.	82
5.5	Same as Figure 5.4 at X-band.	83

List of Figures

5.6	Rainfall amounts estimated from $Z-R$ (circles), $R-Z$ (triangles) and $R-K_{dp}$ (crosses) power laws for each type of rain at C-band frequency. For comparison purposes, rain amounts are normalized by the respective areal rain amount. Black (green) symbols denote the rain amounts associated with the average $A(P)$ relationships.	84
5.7	Same as Figure 5.3 for $R-Z$ relationship at C-band and a temporal resolution of 30 min.	85
5.8	Influence of the temporal resolution on the average relative uncertainty of the power law parameters derived at the single point (instrument) scale for $R-Z$ (left) and $R-K_{dp}$ (right) relationships for each type of rainfall. Solid (dashed) line represents the average relative uncertainty on a and c (b and d).	86
6.1	Regional situation of the HPicoNet network in Ardèche, France. Blue circles denote the operational rain gauge network while the pink bars present the HPicoNet network. (courtesy of Gilles Molinié, LTHE, Grenoble).	90
6.2	Example of experimental setup during the HPicoNet campaign on the roof of a school in Lavedieu, Ardèche, France. The setup consists of a 1000 cm ² tipping-bucket rain gauge (left), an optical disdrometer Parsivel (back-right) and an induction ring (front-right).	91
6.3	The experimental setup deployed in Davos, Switzerland in order to investigate the influence of the altitude on the variability of the drop size distribution.	92
6.4	The 2D-Video Disdrometer deployed at the Weissfluhjoch experimental site (WSL-SLF) at 2543 m height in Davos, Switzerland.	93
6.5	The COMMON field campaign involves a microwave link deployed over a 1.85 km distance, 5 autonomous disdrometers deployed at 4 sampling locations and 3 tipping bucket rain gauges (courtesy of Marc Schleiss, EPFL-LTE).	95
A.1	Picture of the electronic circuit controlling the power provided by the solar panel to the battery.	103

List of Tables

3.1	Number of particles N detected by Parsivel 01 integrated over the 15 months as a function of drop sizes at 60 s temporal resolution. The corresponding quantiles as well as the maximum number of particles measured per spectrum at 60 s and 600 s are provided as a function of drop size.	35
3.2	Correlation coefficient (ρ) and ratio of means (rm) between rain rate measurements from single instrument. P (TB) denotes Parsivel (TB rain gauge) and the index is the reference of the instrument.	37
4.1	Statistics of the three different groups of rainfall events at a 60-s temporal resolution.	58
4.2	c_0 , h_0 and s_0 estimates for rain rate R as proposed by Ciach and Krajewski [2006] and Villarini et al. [2008] at 1 and 15 min temporal resolutions. The third column shows the results from the present study for convective, transitional and frontal rainfall events respectively.	64
4.3	Variations of the two parameters (nugget and slope) of the linear variogram model as a function of rainfall type for each quantity of interest at a 60-s temporal resolution. The coefficient of determination ρ^2 between the experimental variogram values and the associated linear model is as well presented. For transitional and frontal groups, values in brackets shows the values of the parameters expressed as a percentage of the ones for the convective group.	68
5.1	Statistics of the three different groups of rainfall events at a 60-s temporal resolution.	76
E1	Relative sampling uncertainty associated with N_t estimates.	113
E2	Relative sampling uncertainty associated with D_0 estimates.	113
E3	Relative sampling uncertainty associated with R estimates.	114
E4	Relative sampling uncertainty associated with Z_h estimates (in dBZ) at X- (9.4 GHz), C- (5.6 GHz) and S-band (2.8 GHz) respectively.	115
E5	Relative sampling uncertainty associated with Z_{dr} estimates (in dB) at X- (9.4 GHz), C- (5.6 GHz) and S-band (2.8 GHz) respectively.	116

List of symbols

a	prefactor of the Z - R relationship [mm ^{6-b} h ^b m ⁻³]	6
a_h	specific attenuation at horizontal polarization [dB km ⁻¹]	83
A	attenuation factor in radar equation [-]	6
b	exponent of the Z - R relationship [-]	6
c	prefactor of the R - K_{dp} relationship [mm km ^d h ⁻¹ deg ^{-d}]	75
c_A	prefactor (R - K_{dp}) estimated at the pixel scale [-]	82
c_0	nugget parameter of $\hat{\rho}(h)$	63
C	constant depending on the characteristics of the radar (radar equation) [-]	6
$C_U(h)$	covariance of U for the distance lag h	59
$C_Y(h)$	covariance of Y for the distance lag h	59
CV	coefficient of variation (or normalized standard deviation) [-]	24
d	exponent of the R - K_{dp} relationship [-]	75
d_A	exponent (R - K_{dp}) estimated at the pixel scale [-]	82
D	drop diameter [mm]	4
D_0	median-volume diameter [mm]	24
D_m	mass-weighted diameter [mm]	24
D_{max}	maximum drop diameter recorded [mm]	??
E	expectation	61
f	probability density function	23
G	gain of the radar antenna [-]	5
h	distance separation vector [m]	61
h_0	e-folding distance of $\hat{\rho}(h)$ [m]	63
K	refractive factor of liquid water [-]	6
K_{dp}	specific differential phase [° km ⁻¹]	7
$K_{dp,A}$	specific differential phase at the pixel scale [° km ⁻¹]	83
L	length of Parsivel laser beam [mm]	15
m	complex refractive index of water [-]	77
$m_{i,t}$	quantity measured by station i at time step t	23
$\hat{m}_{i,t}$	simulated $m_{i,t}$ values for station i at time step t	80
m_U	mean of U	59
m_Y	mean of Y	59
$\bar{m}_{E,t}$	arithmetic mean of $m_{i,t}$ for i in the ensemble E (i.e., S_k or n)	40

List of symbols

M_i^a	average of all the simulated values for the simulation i over the domain	70
M_i^p	value simulated at the pixel in the center of the field for the simulation i	70
M_t	real value of the variable at time t	41
n_s	number of samples	44
$N(D)$	concentration of drops with a diameter D [$\text{m}^{-3} \text{mm}^{-1}$]	4
N_h	number of pairs separated by a distance approximately equal to h	61
N_t	total concentration of drops [m^{-3}]	23
\bar{P}_r	integrated (over all hydrometeors) power returned to the radar [W]	5
P_t	transmitted power [W]	5
Q_p	quantile with a probability $p \in]0, 1[$	61
r	distance (range) from the radar to the target [m]	5
rm	ratio of means [-]	37
R	rain rate [mm h^{-1}]	6
\hat{R}	simulated rain rate [mm h^{-1}]	80
R_A	pixel average rain rate (i.e., over the 16 stations) [mm h^{-1}]	79
$\Re()$	real part of a complex number	77
s_0	correlogram shape parameter of $\hat{\rho}(h)$	63
S_{eff}	effective Parsivel sampling area [mm^2]	15
$S_{hh vv}$	forward scattering amplitudes at horizontal/vertical polarization [m]	77
S_k	Subset of k instruments among n	40
$U(x)$	stationary random function	59
$u(x)$	regionalized variable	61
$v(D)$	the terminal velocity of a drop of diameter D [m s^{-1}]	6
W	width of Parsivel laser beam [mm]	15
x	position vector in space domain	59
$Y(x)$	logarithm of $U(x)$	59
Z	radar reflectivity factor [$\text{mm}^6 \text{m}^{-3}$]	5
Z_A	pixel average reflectivity (i.e., over the 16 stations) [$\text{mm}^6 \text{m}^{-3}$]	79
Z_{dr}	differential reflectivity [dB]	7
Z_h	radar reflectivity at horizontal polarization [$\text{mm}^6 \text{m}^{-3}$]	7
Z_v	radar reflectivity at vertical polarization [$\text{mm}^6 \text{m}^{-3}$]	7
α	prefactor of the a_h - K_{dp} relationship [$\text{dB deg}^{-\beta} \text{km}^{\beta-1}$]	83
β	exponent of the a_h - K_{dp} relationship [-]	83
$\gamma(h)$	sample variogram at the inter-distance h	61
$\hat{\gamma}(h)$	sample variogram estimator	61
$\hat{\gamma}_p(h)$	quantile variogram estimator	61
$\varepsilon_{S_k,t}$	normalized difference between $\bar{m}_{S_k,t}$ and $\bar{m}_{n,t}$	41
$\varepsilon_i^r(M)$	relative error between M_i^p and M_i^a	70
λ	wavelength of the transmitted signal [cm]	5
σ_B	backscattering cross-section [cm^2]	6
σ_{B_h}	backscattering cross-section at horizontal polarization [cm^2]	77
$\sigma_{B,i}$	backscattering cross-section of the target i [cm^2]	5

σ_U	standard deviation of U	59
σ_Y	standard deviation of Y	59
$\sigma_{\varepsilon_{S_k}}$	standard deviation of ε_{S_k}	41
$\sigma_{\varepsilon_i^r}$	standard deviation of ε_i^r	70
σ_{ω_i}	standard deviation of ω_i	23
σ_{ω}^r	relative sampling uncertainty	41
ρ^2	coefficient of determination	66
$\rho_{i,j}(h)$	Pearson correlation coefficient for the pair of instrument (i, j)	62
$\hat{\rho}(h)$	modified-exponential parametric correlation model	62
$\hat{\rho}_{\log}(h)$	logarithmic transform of $\hat{\rho}(h)$	63
$\omega_{i,t}$	sampling uncertainty associated with the measurement process	41
χ_1^2	chi-square variable with one degree of freedom	61

List of acronyms

2DVD	2D-Video Disdrometer	5
COMMON	COMmercial Microwave link for urban rainfall MONitoring	94
DBS	Dual Beam Spectropluviometer	15
DSD	(rain)Drop Size Distribution	4
EAWAG	Swiss Federal Institute of Aquatic Science and Technology	94
EPFL	École Polytechnique Fédérale de Lausanne	19
FIFO	First In First Out	17
GCM	Global Climate Model	2
GPCP	Global Precipitation Climatology Project	7
GPM	Global Precipitation Measurement	102
GPRS	General Packet Radio Service	19
GPS	Global Positioning System	19
HYMEX	HYdrological cycle in Mediterranean EXperiment	89
JW	Joss-Waldvogel electromechanical disdrometer	5
nlS	Nonlinear Least Squares function of the <i>R-cran</i> software	63
LTE	Laboratoire de Télédétection Environnementale	91
LTHE	Laboratoire d'étude des Transferts en Hydrologie et Environnement	91
PARSIVEL	PARticle SIze and VELOCITY	14
POSS	Precipitation Occurrence Sensing System	5
SLF	WSL-Institut für Schnee- und LawinenForschung	92
TB	Tipping-Bucket rain gauge	21
UWM	EAWAG-Urban Water Management	94
WSL	eidg. forschungsanstalt für Wald, Schnee und Landschaft	92

1 Introduction

1.1 Rationale

The hydrological cycle, i.e., the transport of water through the different components (land, ocean and atmosphere), is a key phenomenon in the complex equilibrium of the Earth. The precipitation, i.e., the atmospheric water (liquid and solid) that reaches the Earth's surface, is a crucial component of the hydrological cycle. During the last decade, the number of studies investigating the impacts of climate change on the Earth system is constantly increasing. While large uncertainties remain on the magnitude of the future changes, most of the assessments indicate that future increase of global temperature is '*very likely*' [Trenberth et al., 2007]. Instrumental observations over the past 150 years clearly indicate that temperatures at the surface of the Earth have risen with important regional variations [Huntington, 2006]. During the last decade, various analyses have pointed a significant intensification of the Earth's water cycle as a response to climate change [see Huntington, 2006, and references herein]. Because it is affecting the whole system, changes are expected on atmospheric circulation, atmospheric moisture and precipitation as a consequence.

Anthropogenic air pollution (aerosols, dust, black carbon) can have a strong impact on the radiative budget of the Earth. This impact is twofold as it is related to (*i*) the optical properties of aerosols, which can absorb or scatter the incoming (from the sun) and outgoing radiations (from the Earth) and (*ii*) their indirect effect on cloud properties. Indeed, an increase of the concentration of air pollutants, and consequently of *cloud condensation nuclei*¹, tends to increase the concentration of cloud droplets to the detriment of their sizes [Ramanathan et al., 2001] as the water vapour has much more nuclei on which to condense (see Section 1.2). Due to the smaller cloud droplets size, the collision efficiency decrease dramatically which tends to suppress rainfall in urban and industrial polluted areas [e.g., Rosenfeld, 2000]. However, further analyses have highlighted that the decrease of rainfall in polluted areas is not systematic as it can be responsible for an invigoration of cloud convection and a delay in precipitation

¹ *cloud condensation nuclei* is a generic term to denotes all the solid particles and gaseous aggregates on which the water vapour is condensing during the cloud droplets generation.

[Rosenfeld et al., 2008].

Observations over the last decades have pointed that these changes in precipitation are occurring in the amount, the intensity, the frequency and the duration of precipitation [Frei et al., 1998; Trenberth et al., 2007; CH2011, 2011]. However, most of Global Climate Models (GCM) succeed in approximately reproducing the observed intensity or frequency patterns of rainfall but not both at the same time [Sun et al., 2005].

Such modifications of the characteristics of precipitation is likely to have a significant impact on water resources [e.g., Vörösmarty et al., 2000] and water quality [Whitehead et al., 2009], in particular with the increase of water use [Kundzewicz et al., 2007]. For instance, simulations of impacts of climate change on groundwater storage highlight possible shifts or declines of seasonal groundwater recharges [e.g., Eckhardt and Ulbrich, 2003]. In addition, especially for countries producing part of their electrical consumption using hydraulic power², it can have a dramatic influence on the hydroelectric production and hence on the human activity. An additional consequence of a warmer climate could be an increase of precipitation extreme [Frei et al., 1998; Trenberth et al., 2003; Groisman et al., 2005] and most probably an increase of floods and droughts [Wetherald and Manabe, 2002; Milly et al., 2002].

All together, these possible disturbances of the Earth's water cycle can have strong societal impacts [IPCC, 2007]. For instance, modifications of the hydrological cycle can have dramatic impacts on food production [Easterling et al., 2007] and human health, such as deaths occurring during heatwaves, water-borne diseases related to the increase in extreme rainfall [Confalonieri et al., 2007] and release of pollutants washed from soils [Kundzewicz et al., 2007].

In this context, reliable estimation of precipitation is of primary importance. In order to gain a better understanding of the characteristics and the distribution of precipitation, a brief description of precipitation microphysics is helpful.

1.2 Precipitation microphysics

Precipitation results from the combination of various microphysical processes. A brief overview of the principal processes involved in the formation of precipitation is provided hereafter. To initiate the process, air masses have to reach and exceed the saturation with respect to water vapour. This is called the *supersaturation*. Usually, this condition can be fulfilled when air masses are cooled down (below the dew-point), as the water-holding capacity of air decreases with its temperature. Various mechanisms can help cooling down air masses among which the upward motion of air to a higher elevation is the main mechanism. As the air mass is lifted, the decrease of pressure involves the expansion and the adiabatic cooling of the air mass.

²About 57% of the Swiss electricity is produced by hydroelectric power, i.e., by dams holding huge reservoirs, by run-of-river stations that use the natural river flow or by pumped-storage stations (sources: <http://www.uvek.admin.ch/themen/energie/00672/00884/>).

1.3. The concept of raindrop size distribution

The initiation step is the condensation of water vapour to form cloud droplets (typical size is $50\ \mu\text{m}$). In clean air, condensation occurs through random collisions between water molecules to create pure embryonic water droplets. This phenomenon is called *homogeneous* or *spontaneous* nucleation. As homogeneous nucleation requires a high degree of supersaturation, it is rarely fulfilled in natural condition. Nevertheless, natural air contains a large concentration of hygroscopic microscopic particles, called *aerosols*. Aerosols include dust, smoke, salts and chemical compounds. For instance, the average concentration of aerosols over ocean (land) is about 1 (5-6) million aerosols per litre [Barry and Chorley, 2003]. Because the condensation of water on an already existing nucleus requires a lower degree of supersaturation than the homogeneous nucleation, the *heterogeneous* nucleation is the main process in natural conditions. Once initiated, cloud droplets continue to grow through condensation. This process is however too slow to produce drops large enough to fall (raindrops with a typical size between 0.1 and 10 mm) and additional processes are required. Various theories have been suggested to explain the growth of cloud droplets such as the coalescence by electrical attraction, the saturation of cold versus warm droplets or the use of condensation nuclei exceptionally large [Barry and Chorley, 2003]. Current theories are in favour of collision and coalescence processes. Large drops sweep out the smaller ones during their fall by collision and the swept drops are then integrated to the bigger ones by coalescence. However, when drops become too heavy to be maintained aloft by air turbulences, they start to fall down.

Air can be forced to rise by being heated from below, by moving over mountains (called *orographic* precipitation, see [Roe, 2005]) or by frontal activity [Brutsaert, 2005]. Two general cases, that will be used in this thesis, can be roughly separated. When air masses are in more 'stable' condition with weak vertical motions, it may result in what is called *frontal* precipitation. It is usually characterized by weak rain during relatively long durations (typically few 10 of hours) with a wide spatial coverage. On the other hand, when the vertical motions are strong with strong vertical gradients of temperature, it may generate *convective* precipitation. Contrary to frontal one, convective precipitation is characterized by strong rain over short duration and relatively short spatial extension (one or a few convective cells). In Switzerland, with a continental temperate climate, frontal precipitation mainly occurs in winter while convective precipitation occurs in summer.

Investigations of solid precipitation (snow, hail) are beyond the scope of this thesis, and the focus will be on liquid precipitation (rainfall) in the following.

1.3 The concept of raindrop size distribution

At the scale of a few meters and above, rainfall is usually seen as a continuous process because the focus is on the average properties of rainfall over large time intervals and large areas (i.e., region, country, continent). A fundamental integral quantity of rainfall for hydrological studies is the *rain rate* (usually denoted R) which is the flux of atmospheric water arriving on a surface. The associated units are mm h^{-1} . Hydrologists usually focus their attention on the rain rate

which is a macroscopic property of rainfall.

At smaller scales (i.e., below 1 m), the rainfall consists of individual *raindrops* with different sizes, shapes, fall velocities, as suggested by the various processes involved in precipitation formation (see Section 1.2). The information on raindrop characteristics is called the *microstructure of rainfall*. Figure 1.1 presents a schematic illustration of the microstructure of rainfall. Due to the large number of raindrops in a given volume, which can be up to several

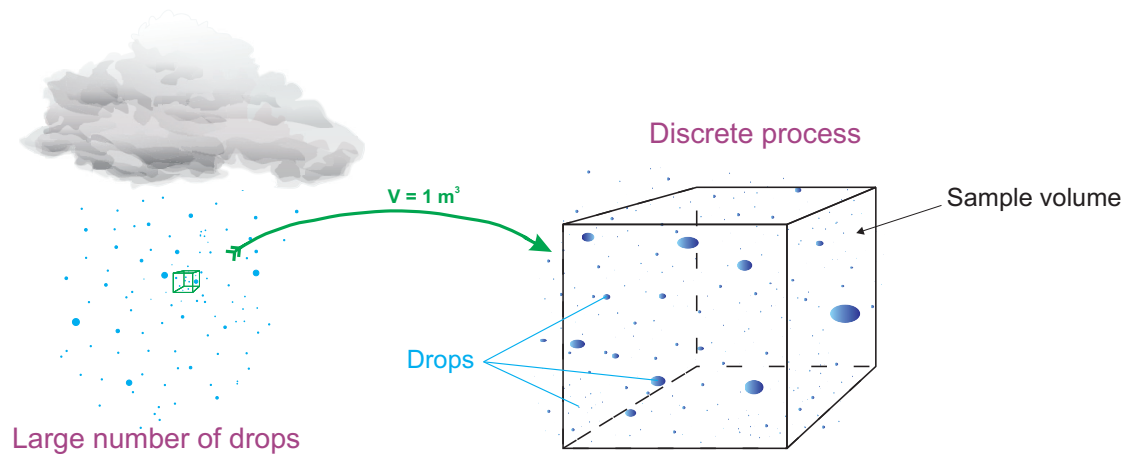


Figure 1.1: A static picture of the microstructure of rainfall.

thousands drops per cubic meter, the current technology (instruments, computers) does not permit to keep track of all the characteristics of individual raindrops. To summarize this information, a statistical approach is usually considered with the concept of (*rain*)*drop size distribution* (denoted DSD in the following) which is the number of raindrops per cubic meter as a function of their respective *equivolume diameter*³. From this information, it is possible, at least for rain, to retrieve information on the shape [e.g., Andsager et al., 1999] and fall speed [e.g., Beard, 1977] of raindrops.

The DSD is denoted $N(D)$ as it expresses a concentration of drops (or number of drops in a given volume) according to their equivolume diameter D and the associated units are $\text{m}^{-3} \text{mm}^{-1}$. DSD information is of primary importance for many environmental applications. Most of these are focused on weather related investigations such as cloud/precipitation microphysical processes [e.g., Pruppacher and Klett, 1997], numerical weather modelling [Michaelides et al., 2009] and weather radar applications [e.g., Marshall and Palmer, 1948; Bringi and Chandrasekar, 2001].

In addition, many natural processes occurring at the ground require knowledges of the DSD. For instance, information on the kinetic energy of raindrops (provided by the DSD) is essential for investigations on interception of rainfall by vegetation canopy [Keim et al., 2006; Nanko et al., 2010], soil infiltration [Agassi et al., 1994] and erosion [e.g., Salles et al., 2002; Assouline, 2009].

³the *equivolume diameter* corresponds to the diameter of a sphere of equal volume.

The instrument devoted to the collection of DSD samples at the ground is called a *disdrometer*. Different types of disdrometers have been developed over the last decades. The most popular one is the Joss-Waldvogel (JW hereafter) electromechanical disdrometer [Joss and Waldvogel, 1967] developed about 40 years ago. In 1990, the Atmospheric Environment Service of Canada has developed an automated present weather sensor called Precipitation Occurrence Sensing System (POSS) [Sheppard, 1990]. Acoustic technology has been as well considered to design disdrometers [Nystuen, 2001; Henson et al., 2004]. With the great improvement of optical technologies during the last decades, optical disdrometers, such as the spectropluviometer [Campos and Zawadzki, 2000; Salles and Creutin, 2003], the Thies and the Parsivel [Löffler-Mang and Joss, 2000] disdrometer, are becoming more popular. Such disdrometers provide information on the size of drops in 1D (the one orthogonal to the laser beam) which implies some assumptions on the shape of drops [e.g., Andsager et al., 1999]. On the other hand, a 2D-Video disdrometer (2DVD hereafter) has been developed [Kruger and Krajewski, 2002] which consists of 2 orthogonal line-scan cameras sampling at a high frequency. It provides information on the shape (i.e., shadowed area) of the particle in the 2 dimensions. Nevertheless, while the added value of such instrument is widely recognized, the calibration, maintenance and pre-filtering process of the 2DVD is more constraining [Kruger and Krajewski, 2002].

As presented earlier in this section, DSD information is of primary interest for many environmental fields. As the present thesis focuses on weather radar applications, a brief insight into the methods considered for radar measurement of rainfall is relevant.

1.4 Radar precipitation estimation

A convenient and widely used tool to monitor precipitation is weather radar (for RAdio Detec-tion And Ranging) which can be installed at the ground level or on-board of space platforms. Radar is a remote sensing instrument that allows acquiring information on remote targets (hydrometeors in the case of weather radar) without any physical contact. The radar approach is based upon the transmission of an electromagnetic signal at such a wavelength that it will interact with all falling hydrometeors in the scanned volume. The receiver of the radar then measures the signal backscattered by all individual particles. The averaged power returned to the radar \bar{P}_r [W], which is integrated over all the hydrometeors that have been illuminated by the signal, is expressed as [Battan, 1973, p.31]:

$$\bar{P}_r = \frac{P_t G^2 \lambda^2 10^8}{(4\pi)^3 r^4} \sum_{i=0}^n \sigma_{B,i} \quad (1.1)$$

where P_t is the transmitted power [W], G is the gain of the antenna [-], λ is the wavelength [cm] of the transmitted signal, r is the range (distance) to the target [m] and $\sigma_{B,i}$ is the backscattering cross-section [cm²] of the target i . It is clearly emphasized in Eq 1.1 that the received power is a function of the radar characteristics (P_t , G , λ) and the hydrometeors (σ_B). To ease comparison between measurements collected by radars with different characteristics, \bar{P}_r [W] can be related to the *radar reflectivity factor* Z [mm⁶ m⁻³], considering a volume

Chapter 1. Introduction

homogeneously filled by raindrops, through [Battan, 1973, p.43]:

$$\bar{P}_r = \frac{C|K|^2 ZA}{r^2} \quad (1.2)$$

where $|K|^2$ [-] is the refractive factor of liquid water (equal to 0.93), C [-] is a constant depending on the characteristics of the radar ($=\frac{P_r G^2 \lambda^2}{(4\pi)^3}$) and A [-] is a term which takes into account possible attenuation (equal to 1 for non attenuated signal). In Eq 1.2, all the characteristics of the radar are contained in C while hydrometeors properties are in $|K|^2$ and Z .

The radar reflectivity factor Z [$\text{mm}^6 \text{m}^{-3}$] can be expressed as a function of the DSD:

$$Z = \frac{\lambda^4 10^6}{\pi^5 |K|^2} \int_0^{\infty} N(D) \sigma_B(D) dD \quad (1.3)$$

where $\sigma_B(D)$ is the backscattering cross-section [cm^2] of a drop of diameter D [mm]. This equation highlights that Z is only depending of hydrometeors characteristics ($N(D)$, $\sigma_B(D)$). Under Rayleigh approximation⁴, Eq 1.3 can be simplified to:

$$Z = \int_0^{\infty} D^6 N(D) dD \quad (1.4)$$

Similarly, the rain rate R [mm h^{-1}] is an integrated quantity of the DSD:

$$R = 6\pi \times 10^{-4} \int_0^{\infty} D^3 v(D) N(D) dD \quad (1.5)$$

where $v(D)$ [m s^{-1}] is the terminal velocity of a drop of diameter D [mm].

Both quantities can be related to each other through a power law usually of the form

$$Z = aR^b \quad (1.6)$$

where a and b are two parameters highly sensitive to the geographical location and the type of rainfall. Usually, this power law is parametrized using measurements collected at the ground by a unique (or a few) instrument(s). If the instrument deployed at the ground is a rain gauge, the rain rates collected by the rain gauge are compared to simultaneous radar measurements (Z). On the other hand, if the instrument deployed at the ground is a disdrometer, then both quantities can be directly calculated from the collected DSD. Nevertheless, due to the spatial variability of rainfall, these two approaches raise the question of the adequacy of using a and b values derived from point measurement, with a spatial representativity in the order of m^3 , to calculate rain rates at the radar sampling volume scale (about km^3).

⁴which holds for particles small with respect to the incident wavelength.

More recently, polarimetric techniques have been developed in order to collect additional information on the 2D-shape of hydrometeors. Similarly to the Z - R relationship for conventional weather radar, a power law relationship ties R and the specific differential phase K_{dp} [$^{\circ} \text{ km}^{-1}$]. More complex polarimetric radar algorithms have been also developed for rainfall estimation such as: R as a function of Z and the differential reflectivity Z_{dr} [dB]⁵, R as a function of K_{dp} and Z_{dr} [Bringi and Chandrasekar, 2001] or R as a function of Z , K_{dp} and Z_{dr} [Ryzhkov et al., 2005].

1.5 State-of-the-art

Anyone having a look on a map showing the global distribution of precipitation over the Earth will note that precipitation is not uniformly distributed over the Earth. For illustration, Figure 1.2 shows the monthly rain rate climatology from the Global Precipitation Climatology Project (GPCP) for January and July to illustrate the distribution of global precipitation during austral summer and winter respectively. Figure 1.2 clearly highlights how the precipitation are non-uniformly distributed in space and in time (in this case between seasons). This non uniform distribution of precipitation can be observed at different spatial (continent, country, region, ...) and temporal (annual, seasonal, monthly, hourly) scales. As highlighted in Section 1.2, the combination of the various mechanisms in the formation of precipitation (air circulation, water vapour content, aerosols concentration, ...) leads to a variability of drop shape, size, fall speed, ...which makes difficult rainfall monitoring (see Section 1.4 on radar rainfall estimation). In this context, the quantification of the spatial variability of the DSD is crucial. The DSD is highly variable in time and space [Jameson and Kostinski, 2001] although the quantification of this variability is not, so far, widely documented at all scales. Uijlenhoet et al. [2003b] have highlighted a significant variability in the concentration of drops, the mean raindrop sizes and the raindrop size distributions between different types of rainfall (namely, convective, transitional and stratiform) in a mesoscale squall line in Mississippi. Additional studies have investigated the variability of the DSD as a function of rainfall type [Tokay and Short, 1996; Uijlenhoet, 2001; Uijlenhoet et al., 2003a].

From a microphysical point of view, additional studies have examined radar power laws according to three microphysical modes: (*i*) all the variability of the DSD is controlled by variation in the concentration of drops, (*ii*) on the opposite, all variability of the DSD is controlled by variation in the raindrop size, and (*iii*) the variability is controlled by both [Smith and Krajewski, 1993; Uijlenhoet et al., 2003a; Steiner et al., 2004; Prat and Barros, 2009]. However, the microphysical interpretation of the Z - R relationship coefficients is affected by significant uncertainties [Steiner et al., 2004].

⁵the differential reflectivity Z_{dr} is a polarimetric quantity providing information on the average shape of hydrometeors. It is expressed as: $10 \log_{10} \left(\frac{Z_h}{Z_v} \right)$ where Z_h (Z_v) is the radar reflectivity at horizontal (vertical) polarization.

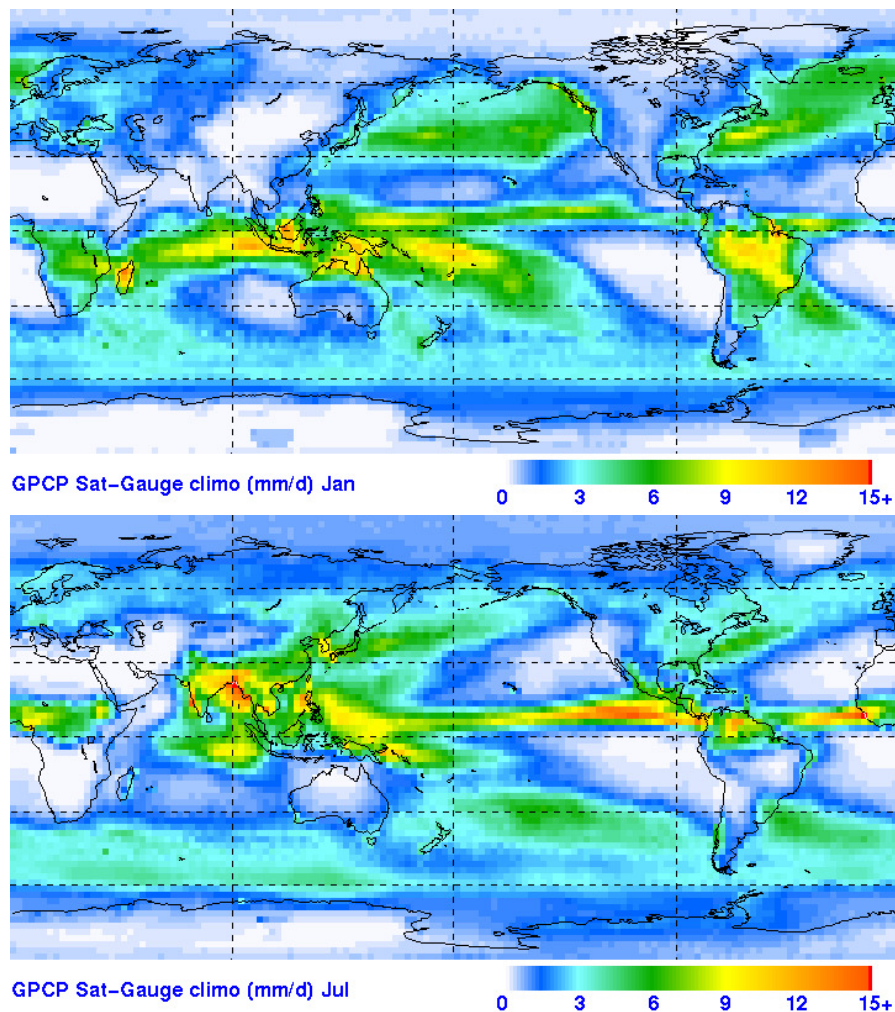


Figure 1.2: Global daily merged precipitation for January (top) and July (bottom). These maps are from the Global Precipitation Climatology Project (GPCP) Monthly rainrate climatology [Huffman et al., 2001]. source: <http://precip.gsfc.nasa.gov/>

Like for any physical parameter, the fluctuations observed at the ground level result from the combination of two signals: the natural variability of the physical process, of interest for hydrological studies, and the sampling fluctuations inherent to the measuring process by the instrument [Gertzman and Atlas, 1977]. The difficulty to distinguish between those two signals is particularly emphasized when using instruments of different types [Miriovsky et al., 2004]. For example, Krajewski et al. [2006] point out significant differences (in the order of 15% on rain amounts) between collocated instruments that are of different types. As a consequence, the sampling uncertainty associated with rainfall measurements is a crucial issue. Several studies have highlighted the significant sampling errors associated with rain gauges [e.g., Habib et al., 2001b; Ciach, 2003] and disdrometers [e.g., Gage et al., 2004; Berne and Uijlenhoet, 2005a; Tokay et al., 2005], which can be responsible for part of the observed variability of the parameters of radar power laws [Ciach and Krajewski, 1999].

Recall that radar power laws used for the estimation of rainfall are usually parametrized using DSD measurements collected at the ground level by a unique disdrometer which, like any other point measurement, has a limited spatial representativity (a few m^3). Indeed, such radar power laws are affected by errors inherent to the sampling properties that relate Z (the radar reflectivity at the surface) to the radar reflectivity aloft [Krajewski and Smith, 2002]. This scaling issue is risen by the spatial variability of the DSD which has a strong influence on such power law [Uijlenhoet, 2001; Lee and Zawadzki, 2005]. This is translated into a wide variety of a and b values in the literature that has already been reported by Battan [1973] about 40 years ago⁶. During the last decades, additional studies have completed this variability of a and b parameters [e.g., Doelling et al., 1998; Atlas et al., 1999; Chapon et al., 2008]. It has been shown in the literature that these parameters are strongly sensitive to various factors. About 30 years ago, Joss and Gori [1978] have shown the influence of the DSD sample size while Campos and Zawadzki [2000] have highlighted that the parameters are strongly sensitive to the type of instrument considered. Moreover, the method for data analysis (type of regression, choice of the dependent variable) can play a significant role in this variability of a and b values [Ciach and Krajewski, 1999; Chapon et al., 2008]. Additional sources are erroneous measurements [Steiner et al., 1999] and measurement uncertainties affecting integral quantities of the DSD [Ciach and Krajewski, 1999; Campos and Zawadzki, 2000]. In addition, the temporal and spatial resolution of the data have a strong influence on the derived Z - R parameters [Morin et al., 2003; Steiner and Smith, 2004; Mapiam et al., 2009].

The sampled DSDs obtained from disdrometer data is discrete, corresponding to the number of classes imposed by the instrument. To overcome this rather artificial quantization, continuous distribution can be fitted on the measured DSD spectra. Different parametrizations⁷ of the DSD have been proposed in the literature, such as the *exponential* distribution [Marshall and Palmer, 1948], the *lognormal* form [Feingold and Levin, 1986] or the *gamma* distribution [Ulbrich, 1983; Willis, 1984]. However, as suggested by Smith and Kliche [2005], DSD parametrization requires large DSD samples for a sufficient accuracy.

As highlighted earlier, knowledge of the spatial variability of rainfall, and in particular of the DSD, is important. This requires spatially distributed measurements from networks of instruments. As rain gauge is still by far the most commonly used instrument to measure rainfall, especially by operational weather services, previous analyses of the spatial structure of rainfall using network of rain gauges have been reported in the literature [Habib et al., 2001a; Ciach and Krajewski, 2006; Villarini et al., 2008; Tokay et al., 2010]. Moreover, the spatial distribution and the number of instruments within the network are sensitive parameters, in particular for investigations on the statistics of extreme rainfall [Blumenfeld and Skaggs, 2011]. Nevertheless, rain gauge only provide information about the rain rate and rain amount which are integral quantities of the DSD.

⁶Battan has listed about 69 different Z - R relationship [see Battan, 1973, p. 90-92].

⁷The mathematical description of a discrete natural phenomena through a continuous distribution is called *parametrization*.

During the last decade, a few studies have investigated the spatial variability of the DSD using spatially distributed measurements. For instance, Lee et al. [2009] has reported a significant variability of the DSD for a 1.3 km distance using four Precipitation Occurrence Sensor Systems (POSS) which can lead to an average error of about 25% in the estimate of rainfall accumulation at the event scale. A similar experiment has been conducted using three Joss-Waldvogel disdrometers over a straight line of about 1.7 km [Tokay and Bashor, 2010], but the authors have reported lower differences in rain accumulations (about 5%). A set up consisting in 16 laser disdrometers deployed at 8 sampling locations over a 4×4 km² area has been reported recently [Tapiador et al., 2010]. Nevertheless, the analyses were limited to some integral quantities of the DSD, namely the rain rate and the radar reflectivity, rather than on the DSD itself. Moreover, the sampling uncertainty associated with the instrument has not been taken into account and is crucial for a reliable and accurate quantification [Miriovsky et al., 2004].

1.6 Objectives

As highlighted in the previous sections, while the variability of the DSD can have a significant influence on radar rainfall estimation, it is still poorly documented and understood. As most of the (few) previous studies investigating the spatial variability of the DSD are focusing on scales larger than 1 km, this thesis aims at investigating this issue at scales below 1 km, which is about the typical size of an operational weather radar pixel. Consequently, the spatial scale of observation considered in this thesis is below 1 km. According to the subdivision of Orlanski [1975], for scale of observation of the atmosphere in the range 200 m to 2 km, the associated nomenclature should be '*micro α scale*'. In this thesis it will be shortened by *microscale*.

The quantification of the spatial variability of the DSD using an experimental approach requires the use of DSD measurements spatially distributed. However, when this project was initiated, in mid-2007, previous studies have been conducted using DSD data collected by a few disdrometers (typically 3-4) rather than by a real network of disdrometers [Miriovsky et al., 2004; Lee et al., 2009; Tokay and Bashor, 2010]. Moreover, the disdrometers used in previous studies were of different types [Miriovsky et al., 2004; Lee et al., 2009] that are affected by different sampling uncertainties which disturb the estimation of the natural DSD variability. Consequently, the first step of this project was to **design and build a network of identical disdrometers that can be easily deployed**, i.e., using autonomous disdrometers, in different locations and configurations, i.e., with station of relatively modest size. The description of this network, that have been completely built in house, is presented in details in Chapter 2 and the associated electronic diagrams are provided in Appendix (A to D) for interested readers.

As suggested in Section 1.5, and because the errors associated with the sampling process of the instruments can be significant, **the sampling uncertainty associated with our DSD measurements should be quantified** prior to use the data collected by the network. To address this issue, an experiment involving collocated measurements has been set up for about 15

months. The details on the set up as well as the statistical methods considered to quantify this sampling uncertainty are presented in Chapter 3.

As soon as the two previous objectives have been fulfilled, the scientific question of the natural variability of the DSD at 1 km^2 scale can be rigorously addressed. **Chapter 4 aims at answering the question: *Is there any spatial organization of DSD fields or are they randomly distributed?*** In order to address this question, a geostatistical approach is considered in Chapter 4. Variograms (see Section 4.3.1 for a definition) of different quantities related to the DSD are computed as a function of the temporal resolution. Chapter 4 concludes with an example of application: the quantification of the error associated with the extension from point measurements to areal estimates due to the spatial structure of the DSD.

Highlighting that at a 1 km^2 scale the DSD fields are organized, the remaining question is *What is the influence of this spatial variability of the DSD on radar rainfall estimates?* **Chapter 5 is investigating this issue by analysing the evolution of radar rain rate estimations (Z-R and R- K_{dp} power laws) with the scale of observation (from point DSD measurements to areal estimates).** Similarly to Chapter 4, this chapter concludes by presenting the typical error associated with the extension of radar power laws parametrized at point scale (instrument) to areal scale.

Perspectives for futures works and additional field campaigns focusing on different scales and types of precipitation are presented in Chapter 6. Finally, a summary and conclusions are provided in Chapter 7.

2 A network of 16 autonomous disdrometers¹

2.1 Introduction

The (rain)drop size distribution (DSD hereafter) is a statistical way to summarize the information about the microstructure of rain and is consequently of primary importance for many environmental fields such as investigation on cloud/precipitation microphysical processes [e.g., Pruppacher and Klett, 1997], numerical weather modeling [e.g., Michaelides et al., 2009], weather radar applications [e.g., Marshall and Palmer, 1948; Bringi and Chandrasekar, 2001] and soil erosion due to the impact of raindrops [e.g., Salles et al., 2002; Assouline, 2009]. The DSD is highly variable in time and space [Jameson and Kostinski, 2001], and this variability has a key influence on the uncertainty affecting radar rain-rate estimates.

Previous studies have investigated the effect of the temporal variability of the DSD on radar rain-rate estimates for different types of rain events (stratiform, transition phase, convective) [e.g., Tokay and Short, 1996; Uijlenhoet et al., 2003b; Lee and Zawadzki, 2005]. This variability can result in important biases in rain rate estimates (in the order of 40%) especially if the physical processes involved are not well identified [Lee and Zawadzki, 2005].

DSD spectra can be collected at the ground level using disdrometers (electro mechanical, acoustic or optical types). Such measurements provide point information with a limited spatial representativity for the surrounding area. The spatial variability of the DSD can be investigated using multiple measurements distributed in the same area. Miriovsky et al. [2004] highlighted the difficulty to distinguish between the natural variability of the DSD and instrumental effects, in particular when using instruments of different types. Further analyses [e.g., Krajewski et al., 2006] pointed out the significant discrepancies between measurements from collocated disdrometers of different types. More recently, the variability of the DSD over a distance of 1.3 km was shown to yield an average error of 25% in the estimation of rain accumulation [Lee et al., 2009]. Tokay and Bashor [2010] also investigated the spatial variability of the DSD over 2 km using 3 disdrometers. Nevertheless, because of the limited spatial distribution of the

¹This chapter is adapted from Jaffrain, J., A. Studzinski, and A. Berne (2011): A network of disdrometers to quantify the small-scale variability of the raindrop size distribution. *Water Resour. Res.*, **47**, doi:10.1029/2010WR009872.

instruments in these two studies, the collected data were not sufficient to fully characterize and understand the spatial variability of the DSD.

More recently, the deployment of a network of 16 disdrometers distributed at 8 sampling locations over a $4 \times 4 \text{ km}^2$ area has been reported [Tapiador et al., 2010]. The analyses were however focused on the rain rate and the radar reflectivity rather than on the DSD itself, and the uncertainty associated with each sensor was not taken into account.

The main objective of this first chapter is to explain the design and the set up of a network of identical disdrometers over an area of $1 \times 1 \text{ km}^2$, corresponding to a typical pixel of an operational weather radar, in order to collect DSD observations which enable quantitative analysis of the spatial variability of the DSD within a weather radar pixel. Moreover, the sampling uncertainty associated with disdrometer measurements is taken into account in the analyses. The network architecture and its components are detailed in Sections 2.2 to 2.5. As an illustration of the added value of the network approach, the spatial variability of the DSD is analysed in Section 2.6 for a period of 1.5 month corresponding to frontal rainfall.

2.2 Parsivel disdrometer

Due to its capabilities, i.e., a high temporal sampling resolution (down to 10 s), the identification of the type of precipitation, the compacity of the sensor and its (relatively) limited cost, Parsivel[®] (1st generation, manufactured by OTT) was selected as disdrometer to build this network. Parsivel is an optical disdrometer [Löffler-Mang and Joss, 2000] providing DSD measurements as well as integrated DSD parameters, i.e., rain rate, radar reflectivity factor and information on precipitation type.

The instrument, presented in Figure 2.1, consists of a transmitter and a receiver separated by a 54 cm^2 horizontal laser beam. At the receiver, the laser signal is converted into a voltage by a photodiode. The measuring principle is based on the attenuation of the signal when a particle crosses the sampling laser beam [Löffler-Mang and Joss, 2000]. The size of the drop along the horizontal axis is estimated from the maximum attenuation of the signal. Then the equivolumetric diameter D of the drop is calculated from different axis ratios (defined here as vertical/horizontal) assuming the shape of the particle is known. Drops smaller than 1 mm are assumed to be spherical (axis ratio = 1). For drops between 1 and 5 mm, the axis ratio varies linearly from 1 to 0.7. For drops with a diameter larger than 5 mm, the axis ratio is set to 0.7. Finally, the terminal fall velocity of the drop is estimated from the time for the particle to go out of the beam. Parsivel retrieval rationale is explained in details in Battaglia et al. [2010].

The instrument provides the number of drops according to their respective equivolumetric diameter and fall speed. The ranges of sizes (from 0 to 25 mm) and velocities (from 0 to 20 m s^{-1}) are each divided into 32 non-equidistant classes. Due to their low signal-to-noise ratio, the two first classes of diameter are always empty (from 0 to 0.25 mm). In order to limit the influence of particles partly detected by the laser beam, the drop concentration should



Figure 2.1: The optical disdrometer Parsivel® (OTT). The measuring principle is based on laser attenuation when a particle crosses the beam.

be calculated using an effective sampling area (denoted S_{eff}), which can be estimated as a function of drop diameter [Löffler-Mang and Joss, 2000; Battaglia et al., 2010]:

$$S_{eff}(D_i) = L \times \left(W - \frac{D_i}{2} \right) . \quad (2.1)$$

L (W) is the length (width) of the laser beam, i.e 180 mm (30 mm) in the case of OTT-Parsivel and D_i is the center of the i^{th} diameter class. S_{eff} is consequently smaller than the physical sampling area (54 cm²).

There exist two types of Parsivel. The one developed by PMTech [Löffler-Mang and Joss, 2000] and the one manufactured by OTT, used in this study. The sampling area (48 cm² for PMTech version) and the type of laser are the two major differences between those two types. Unfortunately, no comparison of collocated measurements from the two types of Parsivel has been reported in the literature so far. Cross-comparison of PMTech-Parsivel measurements with other disdrometers, i.e., 2D-Video Disdrometer (2DVD) and Dual Beam Spectropluviometer (DBS), shows in general good agreements [Krajewski et al., 2006] although some discrepancies are observed in particular for small drops. These discrepancies between instruments are larger during intense rainfall events (R greater than 20 mm h⁻¹). Compared to rain gauges, OTT-Parsivel and other disdrometers generally report higher rain rates although they are consistent with each other [Vuerich et al., 2009]. Due to its capabilities to distinguish between solid and liquid precipitation, Parsivel disdrometer was also used for snow studies [PMTech type: Löffler-Mang and Blahak, 2001; Yuter et al., 2006; Battaglia et al., 2010][OTT type: Egli et al., 2009; Matrosov et al., 2009].

Chapter 2. A network of autonomous disdrometers

The main limitations of Parsivel are: (i) the limited sampling area, (ii) the possibility to have multiple drops passing through the sampling area at the same time and (iii) the axis ratio considered for drop equivolumetric diameter retrieval. The limited sampling area of Parsivel (54 cm^2) has been design to reduce the probability of multiple drops at the same time. However, multiple drops at a time can happen, especially when rain drop concentration is large. This results in artificially larger drops with unrealistic associated fall velocities. In addition, the splashing of drops on the head of the sensor can induce non-natural small drops. Due to the shape of the instrument, strong wind might have an effect on Parsivel measurements, in particular for small drops [Chvíla and Sevrúk, 2008]. Finally, the axis ratio model assumed in Parsivel equivolumetric retrieval (mentioned above), compared to other models such as Andsager et al. [1999] may account for part of the differences observed between Parsivel and other instruments (rain gauges, 2D-Video disdrometer).

2.3 Autonomous station

In order to be easily deployed in different configurations at different locations, the disdrometers have to be designed for an autonomous functioning in terms of power supply as well as data transmission and storage. In the following, the term *station* denotes the ensemble formed by a Parsivel and all the associated components required for energy and data management presented hereafter. A complete autonomous station is presented in Figure 2.2.

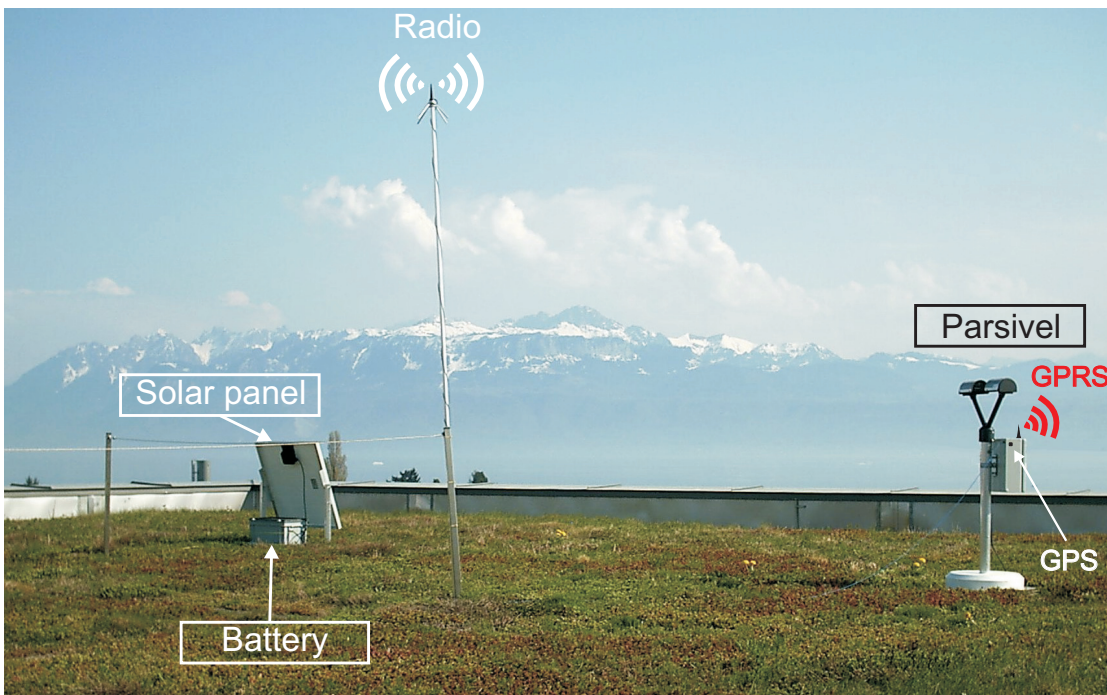


Figure 2.2: A wireless autonomous station for DSD measurement. The station consists of a Parsivel, an electronic unit managing power and data transmission, a battery and a solar panel.

Power is provided by a 12 V battery connected to a solar panel of about 0.48 m² providing a maximum power of 65 W. Because the voltage provided by the solar panel can be larger than 12 V (depending on solar radiation and the altitude of the station) and in order to increase the lifetime of the battery, charge cycles are controlled by an electronic circuit (see Diagram in Appendix A). The voltage of the system is one of the parameters used for the monitoring of a station. In order to reduce wind disturbance potentially induced by the solar panel, the latter can be deployed away from the sensor (typically 5-10 m). The electronic unit has been completely designed and built in-house. It consists of three main parts: the *power*, the *data* and the *modem* units.

The *power* unit is managing the power supplied to the electronic unit, i.e., shutting down the station properly if the voltage provided by the battery is below 11 V. Inversely it switches the station on when the power is high enough for more than one hour in order to avoid electrical hysteresis. Additional details as well as the electronic diagram for this unit is presented in Appendix B.

The *data* unit controls data collection and converts serial binary data signal from RS485 (Parsivel output) to RS232TTL (data logger input). At each time step, the *data* unit collects and stores the measurements in a buffer memory (denoted as FIFO for First In First Out) until the remote logger queries those data via radio communication. Moreover, this buffer memory gives the opportunity to repeat the data transmission process in case of disturbance in the communication. The electronic diagrams of the RS485-RS232TTL converter and the FIFO are presented in Appendix C and D respectively.

Finally, the *modem* unit is in charge of transferring the data to the remote logger. The modem is a common long range radio modem of 500 mW (YLY-TRM8053-500-05 from the Swiss company Y-Lynx[®]) transmitting data at frequencies between 868 and 870 MHz, depending on the channel and the group of sensors considered. According to the manufacturer, the radio modem can transmit data up to 20 km if the transmitter and the receiver are in line-of-sight and separated by a flat and obstacle-free area. The possible range of distances between the transmitter and the receiver in a more complex and realistic area with buildings and/or vegetation is considered to be about a few km. Using directional antenna improves the communication and makes possible larger distance lags.

2.4 Network

The network consists of 16 stations designed for an autonomous functioning in terms of power supply and data transfer, providing real-time DSD information as well as quantities derived from the DSD (e.g., rain rate, radar reflectivity factor), identification of precipitation type and additional technical information about the sensor at a temporal resolution of 30 s. This number of sensors results from a trade-off between having a sufficient density of sensors for reliable spatial investigations and limiting the cost of the network. With 16 stations and in this configuration, interdistances range from 85 to 800 m. For instance, interdistances between

Chapter 2. A network of autonomous disdrometers

100 and 200 m (600-800 m) have a minimum of 21 (15) pairs per time step. Assuming the spatial structure is constant over a few min, 16 disdrometers are enough to reliably quantify the spatial variability of the DSD by combining data collected at a 30 s temporal resolution over short time periods (typically few min).

For data storage, the Campbell Scientific® data logger CR1000 was selected because of its capabilities to manage different analog inputs. The CR1000 is equipped with a CompactFlash memory module CFM100 and a 2 GB card. For cost reasons, all the 16 stations of the network could not be equipped with a data logger. Consequently, the network is organized around four data loggers, each one managing data from four stations. The network is hence divided in four groups of 4 stations. Each group is lead by the station equipped with the data logger, named *master station*. To avoid interference during transmission, each group is using its own range of frequencies. Within the considered range of frequencies, different channels have been defined in order to switch between channels in case of disturbance in the radio transmission. The station identifiers are composed of two numbers: the first one corresponds to the number of the group (from 1 to 4) and the second one indicates the number of the station within this group (from 0 to 3). The station “0” of each group is the master station while the three others stations of the group are named *slave stations*. The organization of the different groups within the network is presented in Figure 2.3.



Figure 2.3: The network of 16 Parsivels deployed over EPFL campus ($\sim 1 \times 1 \text{ km}^2$) in Lausanne, Switzerland.

Within a time step of 30 s, the master station successively queries data from the three slaves of the same group through radio communication. In case of transmission failure, the master can repeat up to 8 times the operation corresponding to a maximum duration of 3 s per station using a different channel at each repetition. The collection phase can last up to 12 s in total.

2.5 Data management

The remaining 18 s (within a 30 s time step) are devoted to the transmission of the 4 measurements (from one master and the 3 associated slave stations) to a remote web server centralizing data using GPRS (General Packet Radio Service, a standard service for mobile phone communication) connection. The temporal resolution of the network is driven by GPRS capabilities. The GPRS module needs up to 15 s to fully transmit the data to the remote server. The memory card is not required when using GPRS but is used as backup if problems occur with GPRS communication. Given the size of a complete measurement, about 5 KB for each sensor, the autonomy of the 2 GB memory card in case of data transmission failure is about 30 days. The clock of each data logger is synchronized every day at midnight using the GPS (Global Positioning System) receiver included in the GPRS module.

Hence, the remote server receives data from the 4 master stations every 30 s. The last transmitted data are visible on the server web page in order to check that all data were successfully transmitted. Once a day, data are remotely downloaded and stored. Data from each station of the network are then controlled and an email alert is sent if a station is not providing data. Using the combination of GPRS and radio communication, stations can be remotely reset and reboot. Daily quality control is very useful to quickly detect technical failures within the network.

2.6 Applications

The network was fully deployed over the campus of the Swiss Federal Institute of Technology in Lausanne (EPFL being the french acronym), Switzerland, in March 2009. The 16 stations were regularly distributed on the roofs of EPFL buildings in order to cover an area of about $1 \times 1 \text{ km}^2$ (Figure 2.3). To prevent possible wind disturbances induced by the buildings (“edge effects”), the stations were deployed as far as possible from the edges of the roofs. Local winds have usually limited speed (usually below 5 m s^{-1}) which have been shown to have negligible effect on DSD measurements (see Section 3.2). Higher wind speeds can have an influence on Parsivel measurements (as well as on rain gauges), but it is beyond the scope of this paper to thoroughly investigate this issue. All the Parsivels in the network were deployed so that the line between the 2 sensor heads was perpendicular to the prevailing wind. So Parsivel measurements will be supposed to be at least representative of the true rainfall.

Because of maintenance work on the roofs of EPFL buildings, this deployment ended in July

2010². The network has been running in this configuration for 16 months and has collected about 540 hours of rain corresponding to a total rain amount of about 820 mm on average. In order to keep this paper short, one period representative of frontal rain events has been selected to illustrate the measurement capabilities of the network of disdrometers.

2.6.1 Method and Data Set

The selected period, from the 26th of March 2010 to the 6th of May 2010, is mainly dominated by frontal rainfall (as seen from visual inspection of operational radar rain-rate maps). In the following, a rainfall event is defined as a continuous rainy period of at least 15 min surrounded by continuous dry periods of at least 15 min. The selected period corresponds to 14 rain events lasting 53 h overall, for a total mean rain amount of about 93 mm. The rain rate values averaged over the 16 stations of the network as well as the associated mean and individual rain amounts are presented in Figure 2.4. The maximum difference in terms of rain amount between individual stations is about 26 mm for the period, which corresponds to 24% of the maximum rain amount recorded by an individual station.

The DSD spectrum integrated over the period is presented in Figure 2.5. It has to be noticed that drops bigger than 7 mm (upper limit of the diameter class centered on $D=6.5$ mm) have been recorded over the network but have been filtered out because they do not seem to be very realistic. Their influence appears to be limited due to their very low number (30 such drops have been collected by the network over the considered, corresponding to less than 2 drops per station on average). Moreover, in order to remove outliers induced by instrument limitations (rain splashing, multiple drops at a time) and non-meteorological sources of error (insects, spiders, ...), a filter based on a velocity-diameter relationship have been applied on DSD measurements. Similarly to Kruger and Krajewski [2002], but using the drop velocity model proposed by Beard [1977], drops with a measured velocity that deviates more than 60% from the theoretical velocity are disregarded. This threshold (60%) has been estimated by comparing rain rate values derived from collocated Parsivels and tipping-bucket rain gauges during 15 months [Jaffrain and Berne, 2011]. The filter removes between 10 and 32% of the total number of particles detected depending on the considered station, which represents at most only 5% of the total rain amount recorded over the period.

Data have been selected in order to have all the 16 stations providing a measurement (i.e., no missing measurement due to data transmission failure is allowed) at all time steps. Moreover, non-rainy periods, defined as periods during which less than 3 stations record a positive rain rate at the same time, were not included in the analyses. According to this definition, about 9% of the total number of measurements (collected at 30 s temporal resolution) are rainy. Finally, in order to remove the effect of very small rain rates, only time steps for which all stations record a rain rate $R \geq 0.1 \text{ mm h}^{-1}$ are considered, which corresponds to about 70% of the rainy

²The 16-months data set, which consists of DSD measurements at a 30-s temporal resolution, is easily available for the scientific community. For further information, please visit the Laboratoire de Télédétection Environnemental, EPFL-LTE, Lausanne, Switzerland (<http://lte.epfl.ch>).

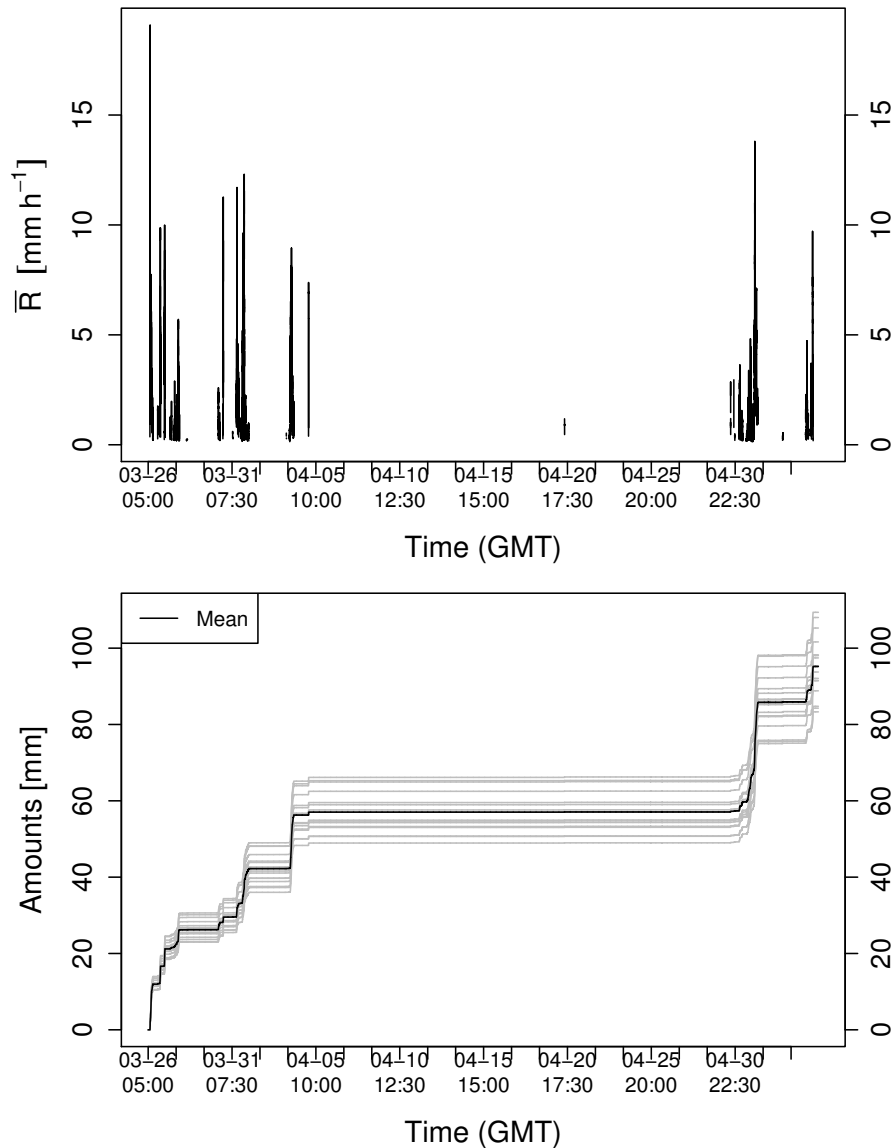


Figure 2.4: Top: mean rain rate over the 16 stations of the network at a 30 s temporal resolution for the selected rain period. Bottom: corresponding mean (black) and individual (grey) rain amounts.

measurements, but to 98.9% of the total amount for the period of interest.

In addition, a tipping-bucket (TB) rain gauge was deployed at about 5 m from Station 43 of the network (see Figure 2.3). Comparison between Parsivel and rain gauge data shows a very good agreement for the presented period (difference of about 3% in the total amount). Parsivel 43 (TB rain gauge) has recorded 87.5 mm (85.3 mm) of total rain amount. The very good agreement in terms of rain amount between Parsivel and TB rain gauge for this period indicates that Parsivel measurements and hence the derived variability of the different

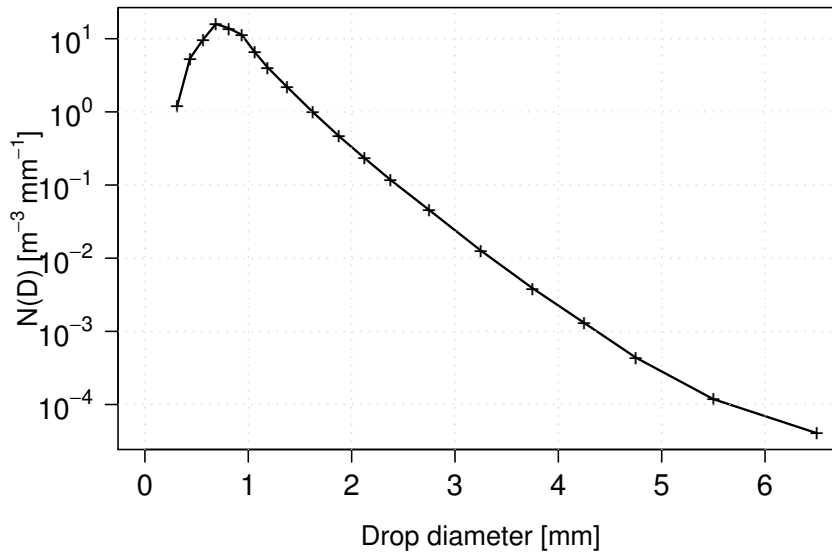


Figure 2.5: DSD spectrum integrated over the selected period. The points figures the center of Parsivel diameter classes.

quantities of interest can reasonably be supposed reliable. It must be noted however that this very good agreement can not rule out possible biases in the concentration of small drops, as they have limited if not negligible influence on rain rate. Similar comparisons have been conducted as well for a period of about 10 events mostly dominated by convective rainfall but the agreement between Parsivel and TB rain gauge is less good (deviation of about 33% in total amount). Wind is likely playing a major role in these discrepancies between the two types of instruments [Vuerich et al., 2009]. Further investigations are needed to better understand these differences, but are beyond the scope of this paper and consequently this convective period has not been included in the present study. It must be noted that such disagreement between Parsivels and rain gauges did not happen during the 15 months considered for the quantification of the sampling uncertainty associated with Parsivel measurements [Jaffrain and Berne, 2011].

Possible biases mentioned earlier (not included in the sampling uncertainty) could have an influence on the estimated variability values. If such biases are constant over the network, the proposed approach still provides a reliable order of magnitude of the variability.

2.6.2 Sampling uncertainty

Like any measurement of a physical process, DSD measurements from Parsivel are affected by an uncertainty associated with the sampling process of the instrument. Because this sampling uncertainty can be of the same order as the natural signal variability, it should be taken into account for any analysis based on Parsivel measurements [Miriovsky et al., 2004]. The

sampling uncertainty associated with measurements from a single Parsivel has been quantified for different quantities related to the DSD (e.g., total concentration of drops, mass-weighted diameter, rain rate) using a data set collected by two collocated Parsivels for a duration of 15 months. Because the sampling uncertainty may vary with the magnitude of the quantity of interest, it was estimated for a range of values as well as for different temporal resolutions. The reader is referred to the Chapter 3 (or Jaffrain and Berne [2011]) for more details on the quantification of the sampling uncertainty associated with Parsivel measurements.

A reliable statistical analysis of the spatial variability of the DSD as seen by the network of disdrometers must take into account the combination of sampling uncertainties associated with all Parsivels of the network. Because the sampling uncertainty is varying with the magnitude of the quantity of interest, it can not be assumed uniform over the network, and analytical estimation is not tractable. The sampling uncertainty at the network scale is hence estimated using a stochastic simulation approach.

In the following, the quantity of interest measured by station i at time step t is denoted $m_{i,t}$. The sampling uncertainty associated with this measurement (from the individual station i at time step t) can be considered as a white noise [Jaffrain and Berne, 2011] and is hence characterized by its standard deviation $\sigma_{\omega,i}$. At each time step and for all stations, 500 values of $m_{i,t}$ are generated from a normal distribution centered on $m_{i,t}$ with a variance equal to $\sigma_{\omega,i}^2$. At each time step t , the sampling uncertainty affecting a given statistical descriptor of the DSD measurements collected by the 16 stations (e.g., coefficient of variation) is quantified as the 80% confidence interval calculated from the 500 simulations. A sensitivity analysis was performed to determine a suitable number of simulations and it appears that 500 is a good trade-off between convergence and computation time. It should be noted that this approach is based on the assumption that the sampling uncertainty in the observation of each instrument is independent in space. This assumption is difficult to demonstrate as it required collocated measurements distributed in space (at each sampling point of the network).

2.6.3 Variability of quantities related to the DSD

The DSD, denoted $N(D)$ [$\text{m}^{-3} \text{mm}^{-1}$], can be seen as the product of the total concentration of drops N_t with a probability density function $f(D)$:

$$N(D) = N_t f(D) \quad . \quad (2.2)$$

The total concentration of drops N_t [m^{-3}] is the sum of the DSD over the range of sampled drop diameters:

$$N_t = \int_{D_{min}}^{D_{max}} N(D) dD \quad . \quad (2.3)$$

Chapter 2. A network of autonomous disdrometers

A commonly used first-order statistical descriptor of the probability density function $f(D)$ is the mass-weighted diameter D_m [mm] [Bringi and Chandrasekar, 2001] which is the ratio of the 4th and the 3rd moment of the DSD:

$$D_m = \frac{\int_{D_{min}}^{D_{max}} N(D) D^4 dD}{\int_{D_{min}}^{D_{max}} N(D) D^3 dD} . \quad (2.4)$$

D_m is less affected by the quantization of diameter sizes in disdrometer data than the median-volume diameter (D_0) which represents the diameter that divides the volume of water contains in the sampling volume into two equal parts.

An essential quantity related to the DSD is the rain rate R [mm h⁻¹] (flux of water through a given surface):

$$R = 6\pi 10^{-4} \int_{D_{min}}^{D_{max}} N(D) v(D) D^3 dD \quad (2.5)$$

where $v(D)$ is the terminal fall velocity [m s⁻¹] of a drop with a diameter D . According to Eq 2.2, the variability of the DSD at the radar pixel scale can be quantified (at the first order) focusing on N_t and D_m . Moreover, because the rain rate is of primary interest for many applications, the variability of R within a typical weather radar pixel is also quantified for illustration. Other quantities like radar observables for instance, could also be studied in the same way, but such analyses are not presented to keep this paper short. The coefficient of variation (CV), defined as the standard deviation normalized by the mean between the 16 stations, of all quantities is calculated at each time step to quantify the relative variability of the DSD within a radar pixel ($\sim 1 \times 1 \text{ km}^2$).

Total concentration of drops

The relative variability of N_t averaged over the selected period (dominated by frontal events) is about 23%. Figure 2.6 presents the scatterplot of CV values as a function of the corresponding N_t values averaged over the 16 stations (denoted \bar{N}_t).

The highest values of variability are observed for small N_t values, i.e., below 400 m⁻³, with CV values reaching 80%. For N_t values above 400 m⁻³, the observed relative variability is between 8 and 40%. Sampling uncertainty values associated with CV estimates (in blue in Figure 2.6) are close to zero (between 0.01 and 1%) with decreasing uncertainty for increasing N_t values. Uncertainties associated with \bar{N}_t estimates are plotted in red but are not visible because they are very small. Figure 2.6 clearly shows that the measured spatial variability of N_t across the

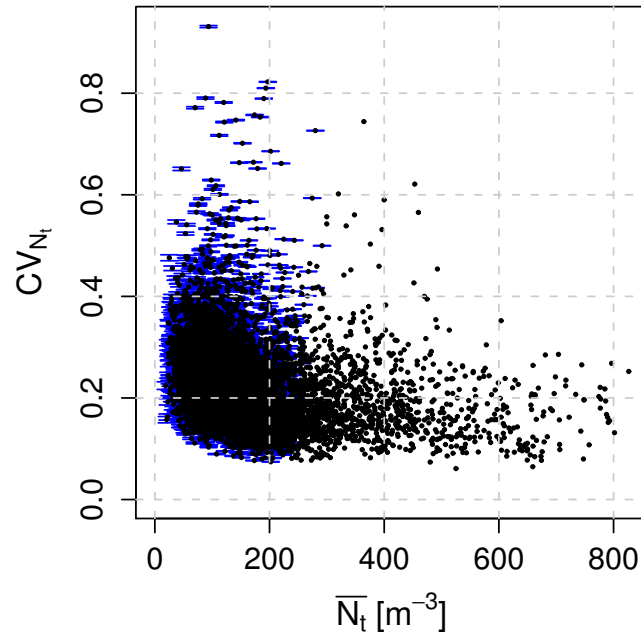


Figure 2.6: Coefficient of variation (CV) of N_t as a function of the mean N_t values (\bar{N}_t) for the selected rain period. Blue lines figure the sampling uncertainty associated with CV values. Red lines figure the one associated with \bar{N}_t values. When the sampling uncertainty in CV and \bar{N}_t is below 0.1%, the error bars are not visible.

network is significant, the natural variability of N_t being larger than the variability due to the sampling uncertainty.

Mass-weighted diameter

Figure 2.7 presents $CV(D_m)$ values as a function of \bar{D}_m . The variability of D_m over the network is between 3 and 60%. Similarly to Figure 2.6, uncertainty values associated with $CV(D_m)$ and \bar{D}_m are plotted in blue and red respectively. Contrary to N_t , globally the CV values tend to increase with \bar{D}_m . As for N_t , the DSD measurements from the network show that the natural variability of D_m is significant at the radar pixel scale. The same analysis on the median volume diameter D_0 produced very similar results.

Rain rate

Figure 2.8 presents the CV values as a function of \bar{R} . Rain rate exhibits CV values between 9% and 121%. Higher CV values are observed for low mean rain rates. The relative variability of R is decreasing with increasing rain rates. For \bar{R} values above 15 mm h^{-1} , the relative variability is below 29%. Small CV estimates are affected by the highest sampling uncertainty values (in blue in Figure 2.8). The uncertainty is decreasing for increasing \bar{R} values. Very low uncertainty

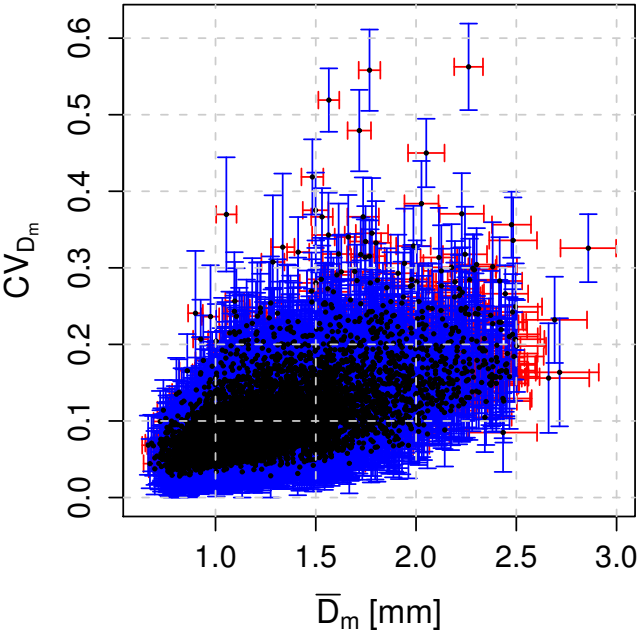


Figure 2.7: Same as Figure 2.6 for D_m .

values are not visible in Figure 2.8. A significant amount of variability of R that can not be explained by the sampling process alone is observed within the monitored area.

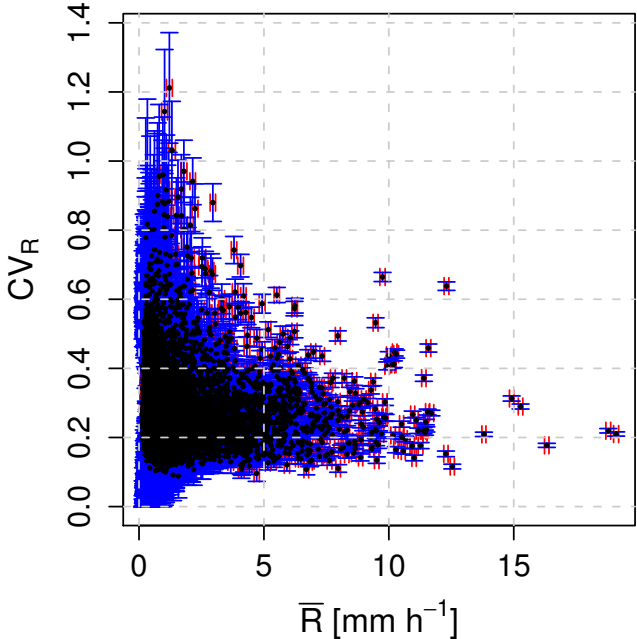


Figure 2.8: Same as Figure 2.6 for R .

2.7 Summary and Conclusion

A wireless network of 16 optical disdrometers (Parsivel) has been designed and deployed over EPFL campus in Lausanne, Switzerland. This network was fully autonomous in terms of power supply as well as data transmission and storage. Each station was connected to a battery and a solar panel. The combination of radio communication and GPRS allowed a real-time remote access to the data. A web server was centralizing the data from the 16 disdrometers. Data quality was automatically controlled daily and an email alert is sent in case of technical failure of a station. Daily data quality control is very useful to quickly detect and fix technical problems within the network.

The network has been running for 16 months collecting 540 h of rain corresponding to a total rain amount of 820 mm on average. A preliminary analysis of a period representative of different frontal rain events (corresponding to 53 h of rain and 93 mm of total amount) is presented to illustrate the measurement capabilities of the network. The spatial variability of the DSD at the radar pixel scale is quantified as the coefficient of variation (between the 16 stations) of the total concentration of drops N_t , the mass-weighted diameter D_m and the rain rate R .

Overall, the collected data set indicates a significant variability of the DSD, even at such a small scale (1x1 km²), that can not be explained by the sole uncertainty associated with the sampling process of the instrument. On average, it is for the selected period in the order of 20% for N_t , 10% for D_m and 30% for R . This analysis demonstrates the capacity of the presented network of disdrometers to capture and quantify the natural variability of the DSD.

Thanks to the data collected by this network of disdrometers, it will be possible to quantitatively analyse the spatial and temporal variability of the DSD at the weather radar pixel scale. In addition, the effect of this variability on the empirical power laws used in weather radar data processing will be investigated. These two questions are of primary importance for the quantification of the uncertainty associated with rainfall estimates from remote sensing techniques.

3 Sampling uncertainty associated with Parsivel measurements¹

3.1 Introduction

The microstructure of rainfall, i.e., the characteristics of individual raindrops, is controlled by the complex interactions between cloud microphysics and atmosphere dynamics [Testik and Barros, 2007]. The microstructure of rainfall is of primary importance for remote sensing of precipitation but also for numerical weather modeling, rainfall infiltration or soil erosion [e.g., Salles et al., 2002]. In the present paper, the focus is on weather radar remote sensing and therefore the size, shape and fall velocity of raindrops are of particular interest. The shape and fall velocity of a raindrop can be accurately derived from its equivolumetric diameter [e.g., Beard, 1977; Andsager et al., 1999]. Therefore, a fundamental property of rainfall for the investigation of its microstructure is the (rain)drop size distribution (DSD hereafter). Rain, and hence DSD, is highly variable in time and space at inter/intra event scales as well as for different geographic locations [Tokay and Short, 1996; Jameson and Kostinski, 2001; Uijlenhoet et al., 2003b; Miriovsky et al., 2004; Lee and Zawadzki, 2005; Lee et al., 2009].

In order to further our understanding of the microstructure of rainfall, reliable DSD measurements are of primary importance. Information about the DSD is usually collected at ground level using disdrometers. Different types of disdrometers have been developed. The Joss-Waldvogel electromechanical disdrometer [Joss and Waldvogel, 1967] is the most popular sensor to collect DSD measurements. Numerous studies have compared JW disdrometer measurements with those of other instruments as rain gauge [Tokay et al., 2001, 2003, 2005; Sieck et al., 2007], optical spectropuviometer [Campos and Zawadzki, 2000; Salles and Creutin, 2003], micro-rain radar [Peters et al., 2005], POSS Doppler radar [Sheppard and Joe, 1994; Campos and Zawadzki, 2000] or 2D-video disdrometer [Tokay et al., 2001]. The fluctuations observed at the ground level result from the combination of two signals: the natural variability of the physical process and the sampling fluctuations induced by the instrument [e.g., Gertzman and Atlas, 1977]. Numerous studies have pointed out the difficulties to distinguish

¹This chapter is adapted from Jaffrain, J. and A. Berne (2011): Experimental quantification of the sampling uncertainty associated with measurements from Parsivel disdrometers. *J. Hydrometeor.*, **12** (3), doi:10.1175/2010JHM1244.1

between these two sources of variability in rainfall observations [e.g., Joss and Waldvogel, 1969; Gertzman and Atlas, 1977; Smith et al., 1993; Gage et al., 2004; Miriovsky et al., 2004; Berne and Uijlenhoet, 2005a; Uijlenhoet et al., 2006].

Any analysis of the DSD variability must take into account the sampling uncertainty associated with DSD measurements, in order to better characterize the natural variability of the DSD, which is the environmental phenomenon of interest. For instance, Krajewski et al. [2006] pointed out the observed significant differences between DSD measurements from disdrometers of different types deployed in the same 100 m² area. Such strong instrumental differences can lead to significant differences in higher-order moments of DSD and must be quantified and integrated in DSD analyses.

The optical disdrometer considered in this study is the Parsivel (OTT[®]), described by Löffler-Mang and Joss [2000]. In previous studies, Parsivel was mostly used to investigate snowfall measurements [Löffler-Mang and Blahak, 2001; Yuter et al., 2006; Tokay et al., 2007; Egli et al., 2009] because of the capability of the instrument to distinguish between solid and liquid precipitation. Recently, a critical evaluation of Parsivel snow measurements based on the comparison with a collocated 2D-Video disdrometer was presented by Battaglia et al. [2010].

This chapter aims at quantifying and characterizing the sampling uncertainty associated with the Parsivel disdrometer in rain. In this context, the sampling uncertainty is defined as the uncertainty due to the limited sampling area of the Parsivel which collects measurements about a spatially and temporally varying process (rainfall). Two collocated Parsivels will sample two distinct subsets of the same population of raindrops, and will hence provide slightly different measurements [Steiner et al., 2003; Berne and Uijlenhoet, 2005a]. This sampling uncertainty does not include all sources of error [Jones et al., 1997], like for example errors related to signal processing issues and limited representativity. Therefore the present approach is different from investigations about the "total" uncertainty affecting rainfall gauges [e.g., Sevruk et al., 2009], which have to deal with the issue of the impossible access to the true rainfall characteristics.

The experimental set up and the data set are described in Section 3.2. Section 3.3 presents the comparison between rain rate measurements from disdrometers and from nearby tipping-bucket rain gauges. The sampling uncertainty associated with Parsivel measurements is quantified for the total concentration of drops, the median-volume diameter, the rain rate, the radar reflectivity and the differential reflectivity in Section 3.4. Summary and conclusions are finally provided in Section 3.5.

3.2 Experimental Setup

Following the approach proposed in previous works [Gage et al., 2004; Tokay et al., 2005; Krajewski et al., 2006; Sieck et al., 2007], two Parsivels (Parsivel 01 and Parsivel 02) were collocated (about 50 cm apart) and deployed at EPFL campus in Lausanne, Switzerland, from late January 2008 to mid-April 2009 (about 15 months). A third one (Parsivel 03) has been

3.2. Experimental Setup

deployed perpendicularly to the two previous ones in order to investigate the effect of the wind on Parsivel measurements. Additional meteorological information was provided by a weather station deployed a few meters away. A picture of the experimental set up is presented in Figure 3.1. In agreement with the local climatology, the wind speeds observed during rainfall



Figure 3.1: The experiment involves two parallel Parsivels (right), two TB rain gauges (in white in the bottom left corner of the picture) and a weather station (center). Parsivel 01 is the closest to the solar panel while Parsivel 02 is the closest to TB rain gauges. The third disdrometer (Parsivel 03), perpendicular to the others, was later deployed in order to investigate the effect of wind on Parsivel measurements.

were limited (below 6 m s^{-1}). Figure 3.2 presents the rain rate differences between Parsivel 01 and 03 as a function of wind speed and direction. As highlighted by the negligible values of the correlation coefficient (-0.08 and -0.05 respectively), the comparison of measurements from the two orthogonal Parsivels did not show a significant influence of the wind (speed and direction) on the deviation of the rain rate measurements from collocated Parsivels. Similar results were obtained when comparing Parsivel 02 and 03.

Moreover, the negligible influence of the wind on Parsivel measurements (in our context) is also indicated by the identical correlation coefficients ($= 0.98$) observed between the different Parsivel pairs (orthogonal or not). The ratio of the average rain rate are also similar with values of 0.92 , 0.89 and 0.96 for the pair 01-02, 01-03 and 02-03 respectively. It has to be noticed that wind effect is investigated for collocated Parsivels at the same height, consequently wind influence on Parsivels at different locations and elevations is not considered in the present paper. Because of a later deployment and of technical problems, Parsivel 03 has missed about 140 h of rain, that is about 20% of the rainy period recorded by Parsivel 01 and 02 and a loss of about 170 mm of rain amount. Because the data set is large, considering two or three Parsivels leads to similar results (see Section 3.4.2). Consequently, data from Parsivel 03 have not been considered in the analyses presented hereafter.

Similarly, two collocated tipping-bucket (TB) rain gauges have been deployed nearby the

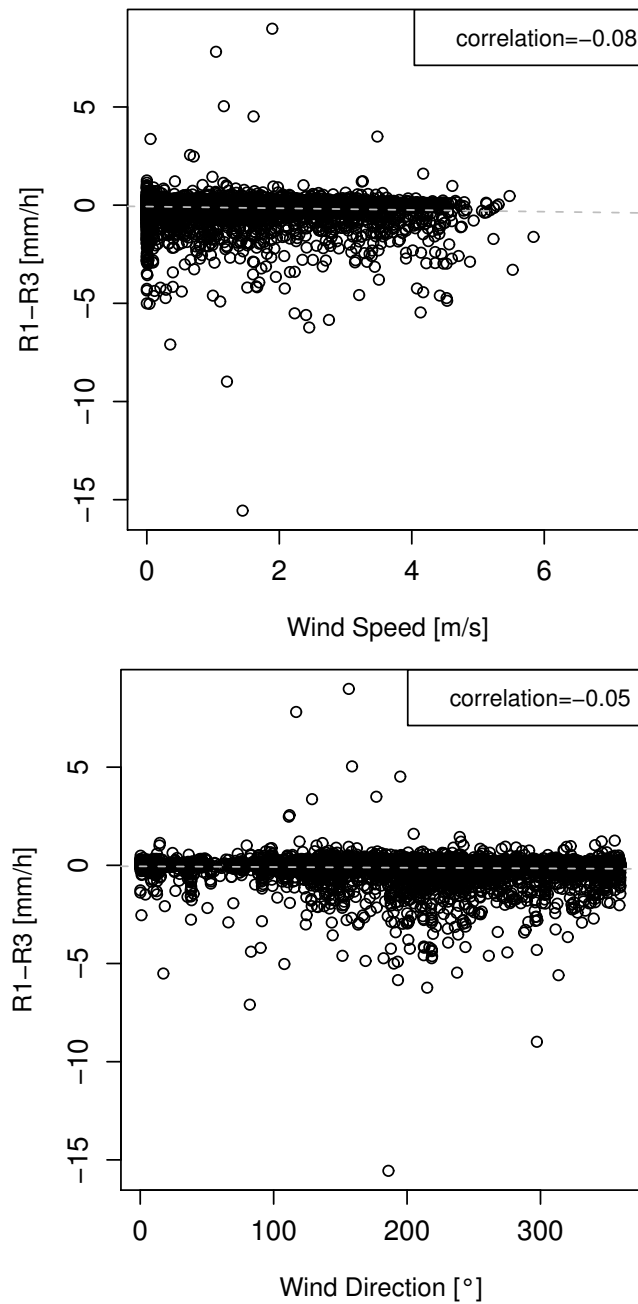


Figure 3.2: Rain rate differences between Parsivel 01 and 03 as a function of wind speed (top) and wind direction (bottom). The dashed line figures the linear regression.

pair of Parsivels (about 3 m away), providing independent measurements of rain rates and rain amounts (Figure 3.1). The Précis Mécanique[®] tipping-bucket rain gauges (model 3029), with a catching area of 400 cm², are connected to data loggers that record tipping times (corresponding to 0.1 mm) with an accuracy of 0.1 s. From visual inspection, splashing does not seem to have a significant impact on TB rain gauges measurements. Because the focus of

the present work is on the sampling uncertainty, the fact that our experimental setup does not strictly follow the recommendations from the World Meteorological Organization [WMO, 2008] is not considered as an issue.

Parsivel is an optical disdrometer (see Section 2.2 for more details) providing drop counts as a function of their size and terminal fall velocity. These measurements are stored in a 32×32 matrix corresponding to 32 non-equidistant classes of diameter (from 0 to 25 mm) and 32 non-equidistant classes of fall speed (from 0 to 22.4 m s^{-1}). All drops in a given class are assigned the values corresponding to the center of the size and velocity classes. Due to their low signal-to-noise ratio, the first two classes of diameter (0.062 and 0.187 mm) are always empty. Therefore, sampled diameters start at the lower bound of the third class, i.e., 0.25 mm. As highlighted in Section 2.2, concentration of drops are calculated using the effective sampling area S_{eff} (see Eq2.1).

Because our investigations focus on rainfall, solid or mixed precipitation is disregarded. The rainy periods, i.e., as soon as a strictly positive rain rate is recorded by at least one of the Parsivels, represent about 990 h of rain. In order to avoid the effect of very weak rainfall on the statistical descriptors, data have been filtered: only time steps for which both Parsivels measure a rain rate R larger than 0.1 mm h^{-1} are considered. For consistency, the same time steps are considered for TB rain gauges. It has to be noticed that the employed filter ($R > 0.1 \text{ mm h}^{-1}$) will remove different time steps depending of the temporal resolution considered. At a time resolution of 20 s, this threshold of 0.1 mm h^{-1} removes about 27% of the rainy measurements. This proportion increases to 48% for a 1-h time step. Nevertheless, the removed time steps represent a loss of only 2 and 3% of the total rain amount at 20 s and 1 h respectively.

To identify and remove suspicious measurements (due to splashing, multiple drops at a time, margin fallers, insects, spiders, ...), a filter based on drop velocity-diameter relationship, similar to the one used by Kruger and Krajewski [2002] and Thurai and Bringi [2005], is applied to the raw Parsivel measurements (32×32 drop counts). The drop velocity model is taken from Beard [1977]. After comparison with the rain gauges in terms of rain amount, the tolerance around this model is set to 60%. Finally, only drops satisfying the equation:

$$|v(D)_{meas} - v(D)_{Beard}| \leq 0.6 v(D)_{Beard} \quad (3.1)$$

are considered, where $v(D)_{meas}$ is the velocity measured by Parsivel and $v(D)_{Beard}$ is the velocity for a drop of diameter D according to Beard's model. Such filter removes about 25% of the total number of particles detected. The filtered drops are mainly below 0.5 mm (about 71%) and between 0.5 and 1 mm (about 28%). In term of rain amount, the filtered drops represent only 3.5% of the total rain amount recorded over the period.

All the estimates of DSD/rainfall variables used in the present study are calculated from DSDs expressed as concentrations of drops per diameter classes (expressed in $\text{m}^{-3} \text{ mm}^{-1}$), computed from the filtered raw DSDs. Figure 3.3 presents the scatterplot of the rain rate computed from DSD (denoted by R') versus the rain rate provided by Parsivel (denoted by R) at a time

resolution of 300 s. The correlation coefficient is about 1 and the ratio of the means is about 1.04. R' is slightly lower than R because of a larger number of time steps with rain rate values below 0.5 mm h^{-1} . Figure 3.3 shows the very good agreement between R' and R , and results

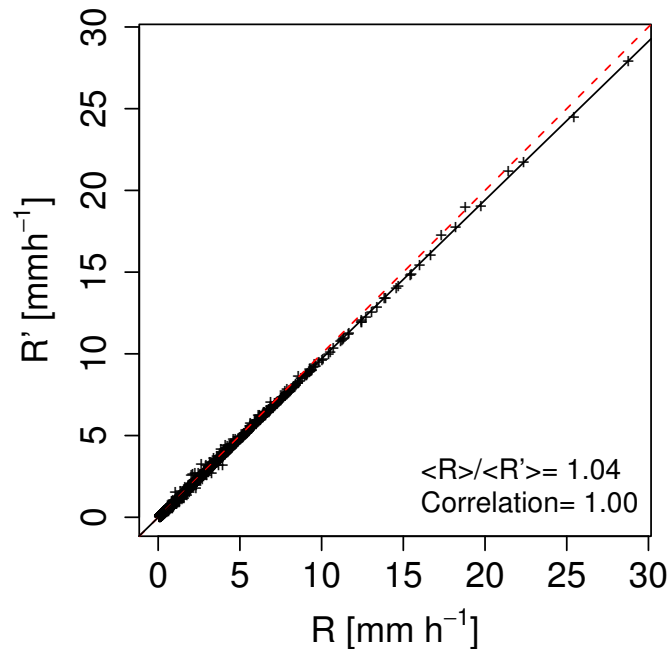


Figure 3.3: Scatterplot of the rain rate provided by Parsivel 01 (R) versus the one derived from the DSD (R') at a 300-s temporal resolution. The dashed (solid) line figures the 1-1 (regression) line.

obtained in this study for R' will be assumed valid for R (as this parameter is likely to be more frequently employed by Parsivel users).

The data set involved in this study (after filtering process) corresponds to about 725 h of rainfall over 15 months from the 19th of January 2008 to the 14th of April 2009. The average rain amount measured by the two Parsivels (TB rain gauges respectively) is about 900.3 (941.2) mm. Figure 3.4 presents the average rain rate from the two Parsivels and the two rain gauges, as well as the cumulative amount for each sensor at a time resolution of 300 s. It indicates that this data set corresponds to light and moderate rainfall with limited maximum rain rate (below 40 mm h^{-1}). Figure 3.5 shows the concentration of drops at 300 s averaged over 15 months for each Parsivel. It shows a slight underestimation of the concentration of drops recorded by Parsivel 01 compared to Parsivel 02 for drops between 1.8 and 5 mm. This underestimation explains the slightly lower rain amount recorded by Parsivel 01 over the 15 months.

Parsivel 01 (02) detected 20 (24) drops in the class 6.5 mm, 10 (12) in the class 7.5 mm and 1 (2) in the class 8.5 and 9.5 mm. Drops larger than 7 mm are considered as unrealistic and were removed from the data set. Nevertheless, their influence on the results are negligible because of their very low numbers (≤ 15). Table 3.1 presents the total number of drops measured by

3.2. Experimental Setup

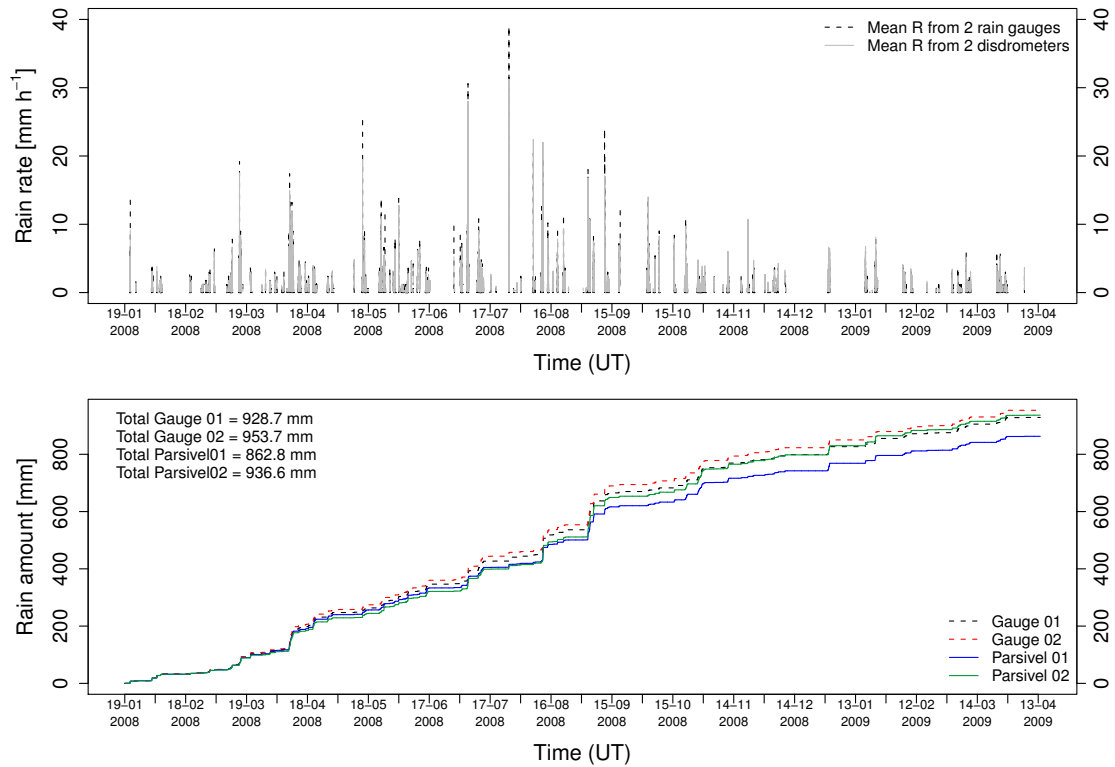


Figure 3.4: Mean rain rate (top) for each type of instruments. Cumulative rain amounts (bottom) recorded by each Parsivel and each TB rain gauge. Both plots correspond to a temporal resolution of 300 s over the 15 months of the experiment.

Parsivel 01 over the 15 months as well as some statistics on drop sizes at 60 s temporal resolution. The 90% quantile of D is about 1.375 mm, which highlights the limited number of big

Table 3.1: Number of particles N detected by Parsivel 01 integrated over the 15 months as a function of drop sizes at 60 s temporal resolution. The corresponding quantiles as well as the maximum number of particles measured per spectrum at 60 s and 600 s are provided as a function of drop size.

D [mm]	≤ 0.5	0.5-1	1-1.5	1.5-2	2-3	3-4	4-5	5-6	6-7
N measured	675357	5443282	1637031	321842	98418	7277	772	72	20
Quantile	8.3%	74.0%	94.0%	98.4%	99.9%	-	-	-	-
$N_{max}(D)/\text{spectrum, 60 s}$	453	1466	582	319	211	52	14	2	2
$N_{max}(D)/\text{spectrum, 600 s}$	3060	9948	3558	1519	859	172	54	6	2

drops in the data set. These statistics are very similar for Parsivel 02. Because the experiment lasted 15 months, the derived statistics are assumed to be robust and representative of the local climatology.

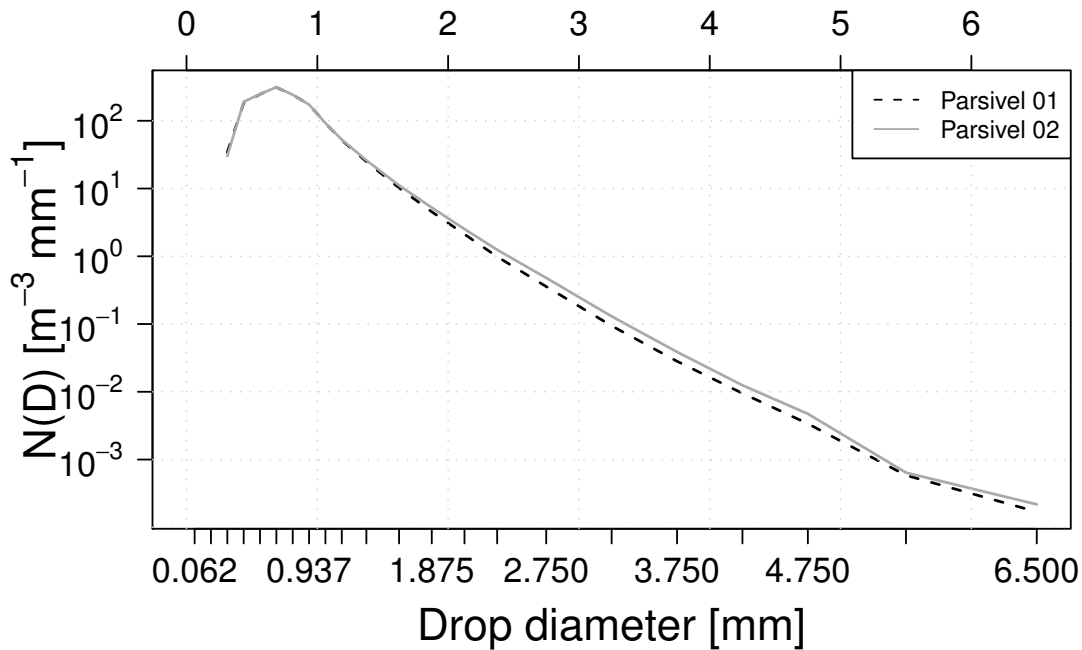


Figure 3.5: 300-s DSD spectrum of each disdrometer averaged over the 15 months of the experiment. The X axis corresponds to the drop diameter using the center of Parsivel classes. The Y axis is the number of drops in log scale.

3.3 Comparison between optical disdrometers and tipping-bucket rain gauges

Prior to the quantification of the sampling uncertainty, Parsivel and gauge rain-rate values are compared to check if there is any significant bias in Parsivel measurements, considering rain gauge as the reference instrument. For rain gauge measurements, the intensity resolution, 0.1 mm per tip, is too coarse for time steps shorter than 5 min (one tip over 5 min corresponds to 1.2 mm h^{-1}) which will be the temporal resolution for the comparison of Parsivel and rain gauge data in this section. From Figure 3.4, we see that the two Parsivels have collected 863.2 and 937.3 mm respectively, that is a difference of about 8%. The two TB rain gauges have collected 928.7 and 953.7 mm respectively, that is a difference of about 3%. On average, Parsivel and TB rain gauges have recorded total rain amounts of 900.3 and 941.2 mm respectively, corresponding to a difference of 4.3% over 15 months. Moreover, considering individual disdrometers and TB rain gauges, the maximum deviation in terms of rain amount between an individual Parsivel and an individual TB is about 9.5% which is reasonable with respect to the 15 months the experiment lasted.

It has been shown in previous studies that Parsivel tends to overestimate rain rate compared to rain gauges [Vuerich et al., 2009]. In the present study however, both Parsivels recorded lower rain amounts compared to the TB rain gauges. This could be explained by: (i) the

3.3. Comparison between optical disdrometers and tipping-bucket rain gauges

rather limited values of the measured rain rates during the 15 months considered, as for limited rain rate values the deviation is less pronounced (see Vuerich et al. [2009]); (ii) the fact that the considered rain rate is directly derived from the DSD and not the one provided by the instrument (which is about 4% larger, see Figure 3.3); (iii) the influence of the drop velocity-diameter filtering process.

Figure 3.6 presents the scatterplot of the rain rates recorded by Parsivel 01 and 02 as well as the comparison between rain rates recorded by Parsivel 01 and TB rain gauges 02 (the 2 sensors between which the bias is the largest) at a resolution of 300 s. The other comparisons between individual sensors show similar agreements, with lower bias however. Table 3.2 summarizes the values of the correlation coefficient and the ratio of mean rain rates associated with the different combinations of two instruments. The correlation coefficient is about 0.98 and the ratio of means is about 0.92 for rain rates measurements between the two Parsivels, showing that they are in very good agreement. The ratio of means between Parsivels 01 and 03 as well as Parsivels 02 and 03 are of the same order. The ratio of means between the 2 rain gauges is 0.97 and the correlation coefficient is 0.90.

Table 3.2: Correlation coefficient (ρ) and ratio of means (rm) between rain rate measurements from single instrument. P (TB) denotes Parsivel (TB rain gauge) and the index is the reference of the instrument.

(X,Y)	(P_{01}, P_{02})	(TB_{01}, TB_{02})	(P_{01}, TB_{01})	(P_{01}, TB_{02})	(P_{02}, TB_{01})	(P_{02}, TB_{02})
ρ	0.98	0.90	0.94	0.92	0.94	0.91
$rm = \bar{R}_X / \bar{R}_Y$	0.92	0.97	0.93	0.91	1.01	0.98

Concerning the comparison of rain rate values from a single Parsivel and from a single TB rain gauge, the correlation coefficient is between 0.91 and 0.94 while the bias indicated by the ratio of means is between 1.0 and 9.5%. Figure 3.4 and Figure 3.6 show the very good agreement between Parsivel and TB rain gauge measurements (in particular for Parsivel 02), indicating that Parsivel measurements have limited bias with respect to TB rain gauge measurements. Figure 3.7 presents the difference of rain rate values between the two Parsivels over the 15 months, at a time resolution of 300 s. From March to June 2008, Parsivel 01 provides slightly larger rain rates than Parsivel 02. From July 2008 to February 2009, Parsivel 02 provides larger rain rates than Parsivel 01. Finally, between January and February 2008 as well as between February and April 2009, there is no clear bias between the two Parsivels. Overall, we will consider that the bias between the two Parsivels is negligible and that the difference between the two Parsivels can be correctly described as a white noise with zero mean. Hence, sampling uncertainty, as defined in Section 1, is likely the main source of error in the measurements from the two Parsivels. Spider webs and insects as well as laser inhomogeneity could explain some of the bias although there is no clear reasons for this timing.

These comparisons show that rain rate estimates derived from DSD measurements provided by Parsivel are reliable and the next section is devoted to the quantification of the sampling

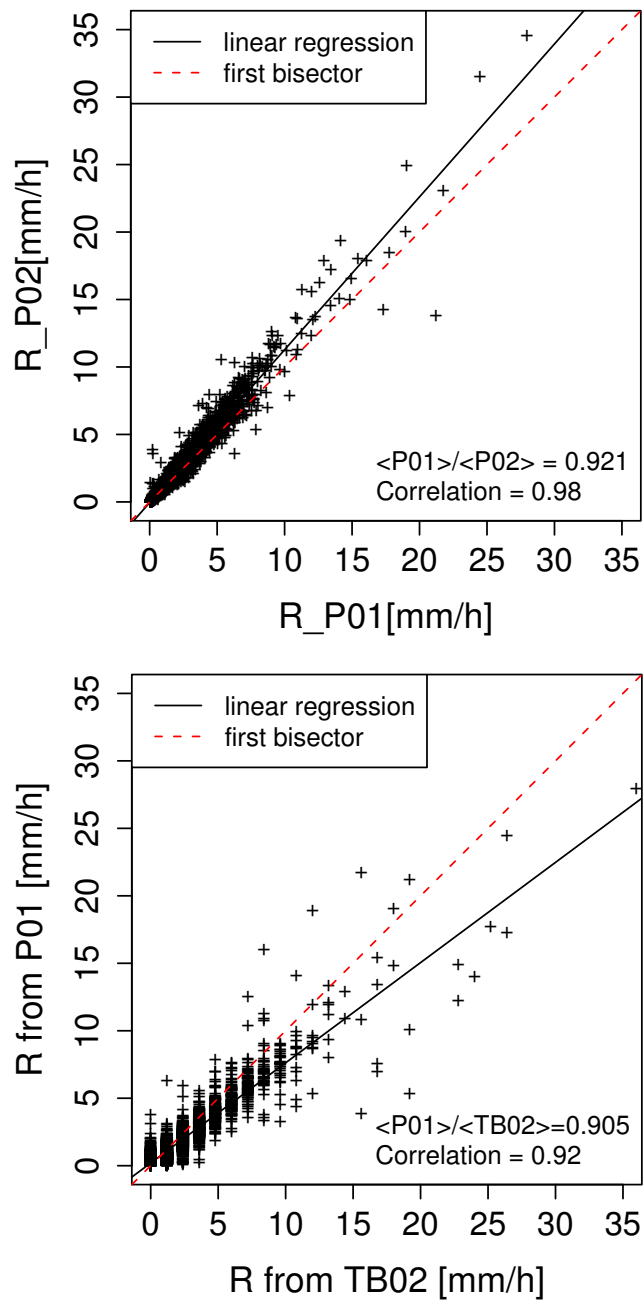


Figure 3.6: Scatterplot of the rain rate recorded by Parsivel 01 and 02 (top) and comparison of rain rates recorded by Parsivel 01 and TB rain gauge 02 at a temporal resolution of 300 s.

uncertainty associated with measurements from a single Parsivel.

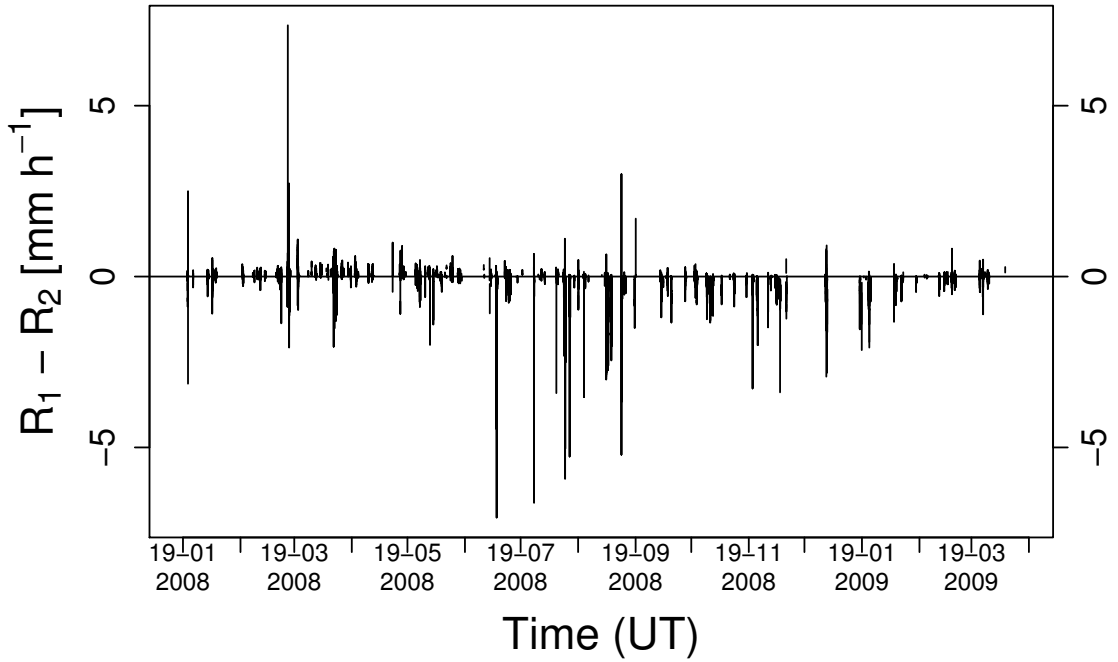


Figure 3.7: Differences between rain rate values recorded by the two Parsivels ($R_{01} - R_{02}$) over the 15 months at a temporal resolution of 300 s.

3.4 Quantification of the sampling uncertainty

3.4.1 Integral quantities related to the DSD

While TB rain gauges provide information only about rain rate, the main benefit of disdrometers is the access to information about the microstructure of rain. For quantitative applications, the statistical moments of the DSD (e.g., rain rate, radar reflectivity) are of major interest. Any analysis based on DSD measurements must take into account the uncertainty induced by the sampling process.

The DSD can be seen as the product of the drop concentration N_t [m^{-3}] and a probability density function f :

$$N(D) = N_t f(D) \quad . \quad (3.2)$$

The total drop concentration N_t is the sum of the DSD over the range of sampled diameters of drops:

$$N_t = \int_{D_{min}}^{D_{max}} N(D) dD \quad . \quad (3.3)$$

Moreover, a quantity commonly used to characterize, at least partly, the probability density f is the median-volume diameter D_0 [mm] which is defined as the 50% quantile of the normalized

Chapter 3. Sampling uncertainty

distribution of liquid water content over all drop diameters:

$$D_0 / \int_{D_{min}}^{D_0} N(D) D^3 dD = \int_{D_0}^{D_{max}} N(D) D^3 dD \quad . \quad (3.4)$$

In other words, drops smaller (respectively larger) than D_0 contribute to half of the total rainwater content in the sampled volume. D_0 is sensitive to the concentration of large drops.

Similarly to Tokay et al. [2005], the rain rate R , the radar reflectivity Z and the differential reflectivity Z_{dr} (the most commonly used moments of the DSD) are considered:

$$R = 6\pi 10^{-4} N_t \int_{D_{min}}^{D_{max}} f(D) v(D) D^3 dD \quad . \quad (3.5)$$

$$Z_{h|v} = \frac{\lambda^4 10^6}{\pi^5 |K|^2} N_t \int_{D_{min}}^{D_{max}} f(D) \sigma_{B,h|v}(D) dD \quad . \quad (3.6)$$

$$Z_{dr} = 10 \log_{10} \left(\frac{Z_h}{Z_v} \right) \quad . \quad (3.7)$$

where v is the drop terminal fall velocity [m s^{-1}], λ is the wavelength [cm], K is the dielectric factor for liquid water [-], D is the equivolumetric diameter [mm] and $\sigma_{B,h|v}$ is the backscattering cross section for horizontal (vertical) polarization [cm^2]. With respect to the DSD, R and Z_h depend on both the drop concentration N_t and the probability density function f , while Z_{dr} only depends on f .

The sampling uncertainty will be quantified for N_t and D_0 , as well as for R , Z_h and Z_{dr} . Because the data set is representative of the local climatology characterized by light to moderate rainfall, the corresponding values of specific attenuation and specific differential phase are low. The sampling uncertainty for these ranges of values is of limited interest, and is hence not considered in the present paper.

3.4.2 Method

Following Tokay et al. [2005], we consider that n collocated sensors sample the same population (the two Parsivels are 50 cm apart). We denote $m_{i,t}$ the variable of interest, derived from the DSD spectrum measured by sensor i at time step t . In the following, S_k denotes a subset of k instruments among n . The arithmetic mean of $m_{i,t}$ for i in S_k at time step t (denoted $\overline{m}_{S_k,t}$) is expressed as

$$\overline{m}_{S_k,t} = \frac{1}{k} \sum_{i \in S_k} m_{i,t} \quad . \quad (3.8)$$

3.4. Quantification of the sampling uncertainty

Similarly, the mean over n sensors at time step t is

$$\bar{m}_{n,t} = \frac{1}{n} \sum_{i=1}^n m_{i,t} \quad . \quad (3.9)$$

As proposed in Chandrasekar and Gori [1991], Gage et al. [2004], Berne and Uijlenhoet [2005a] and Tokay et al. [2005], using the difference between two collocated sampled values of a quantity removes the natural variability and enables the quantification of the sampling variability alone. In order to limit the influence of large absolute uncertainty values and to ease comparison with other sensors, we will consider the relative sampling uncertainty. Assuming that the mean over n instruments is representative of the true value, the normalized difference between Eq 3.8 and Eq 3.9, denoted by $\varepsilon_{S_k,t}$ is defined as

$$\varepsilon_{S_k,t} = \frac{\bar{m}_{S_k,t} - \bar{m}_{n,t}}{\bar{m}_{n,t}} \quad . \quad (3.10)$$

A similar approach based on the relative error has been used previously by Habib et al. [2001b] and Ciach [2003], considering the specific case of one sensor ($k = 1$) among n collocated ones for tipping-bucket rain-gauge measurements.

Moreover, we consider that a given variable related to the DSD spectrum measured by sensor i at time step t can be seen as the sum of the real value of the variable at time t (denoted by M_t), which is of interest but not known, and a sampling uncertainty denoted by $\omega_{i,t}$ associated with the measurement process and considered as a Gaussian white noise.

$$m_{i,t} = M_t + \omega_{i,t} \quad (3.11)$$

Because the considered sensors are identical, the distribution of ω_i is supposed to be identical for all sensors. As a Gaussian white noise, ω_i is supposed to be 0 on average, so the sampling uncertainty is fully characterized by its standard deviation σ_ω . Hence, σ_ω must be derived from the collected data. Replacing Eq 3.8, 3.9 and 3.11 in Eq 3.10 leads to

$$\varepsilon_{S_k,t} = \frac{\frac{1}{k} \sum_{i \in S_k} (M_t + \omega_{i,t})}{\frac{1}{n} \sum_{i=1}^n (M_t + \omega_{i,t})} - 1 \quad . \quad (3.12)$$

As suggested for radar reflectivity measurements [Gage et al., 2004; Berne and Uijlenhoet, 2005a], the relative sampling uncertainty affecting \bar{m}_{S_k} is quantified by $\sigma_{\varepsilon_{S_k}}$, the standard deviation of ε_{S_k} .

Assuming the collocated instruments sample the same DSD population, the relative sampling uncertainty σ_ω^r (r standing for relative) can be calculated from $\sigma_{\varepsilon_{S_k}}$ (see Appendix E for details):

$$\sigma_{\omega}^r = \frac{\sigma_{\omega}}{E[M]} \simeq \sigma_{\varepsilon_{S_k}} \sqrt{\frac{nk}{n-k}} \quad (3.13)$$

Considering that the sampling uncertainty may depend on the value of M , σ_{ω} is estimated for different classes of M , within which M and ω are assumed to be uncorrelated. Figure 3.8 shows the distribution of ε_i values for D_0 between 0.6 and 0.7 mm at a 60 s temporal resolution. For other D_0 classes and temporal resolutions, the distributions of ε_i look similar and therefore the assumption of Gaussian white noise appears reasonable. Nevertheless, outliers cannot

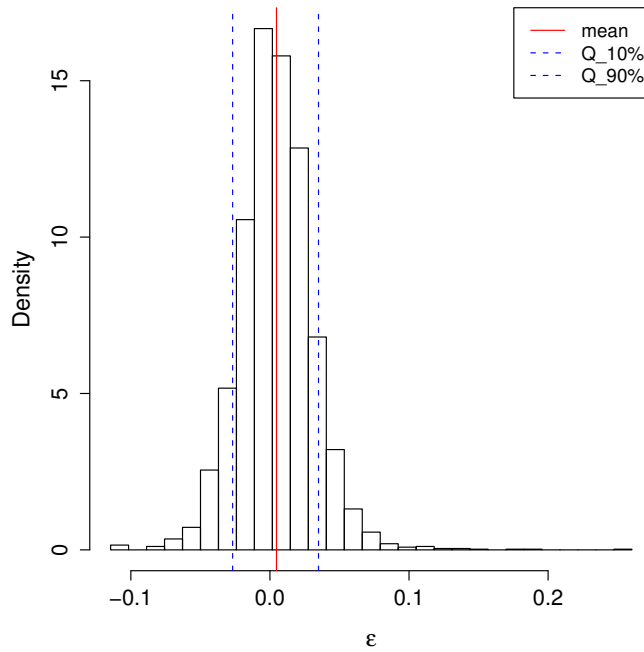


Figure 3.8: Distribution of $\varepsilon_i(D_0)$ values for D_0 between 0.6 and 0.7 mm at a temporal resolution of 60 s. Solid vertical line represents the mean while dashed vertical lines represents the 10% and 90% quantiles.

be excluded especially for classes with low number of ε_i values. The classical estimation of the standard deviation is sensitive to possible outliers, while quantiles are more robust. The difference between quantiles $Q_{90\%}$ and $Q_{10\%}$ corresponds to 80% of the distribution which is in the interval $[-1.28\sigma; +1.28\sigma]$ for a Gaussian distribution. Consequently, a more robust estimation of $\sigma_{\varepsilon_{S_k}}$ can be derived from the quantiles as:

$$\sigma_{\varepsilon_{S_k}} = \frac{Q_{90\%}(\varepsilon_{S_k}) - Q_{10\%}(\varepsilon_{S_k})}{2 \times 1.28} \quad (3.14)$$

As mentioned in Section 3.3, the limited bias between the 2 disdrometers (about 8% in 15 months) is neglected.

3.4. Quantification of the sampling uncertainty

In order to check the validity of Eq 3.13, 4 additional disdrometers were collocated next to the 2 considered ones for a period of about 2 months (all sensors gathered over about 10 m²). Figure 3.9 shows $\sigma_{\varepsilon_{S_k}}^r$ and σ_{ω}^r as functions of the number of sensors for R between 0.1 and 2 mm h⁻¹. As expected, the number of collocated instruments has a significant impact on $\sigma_{\varepsilon_{S_k}}^r$. On the contrary, the relative uncertainty σ_{ω}^r does not significantly depend on the number of sensors deployed. The same computation was performed as well for N_t , D_0 , Z_h and Z_{dr}

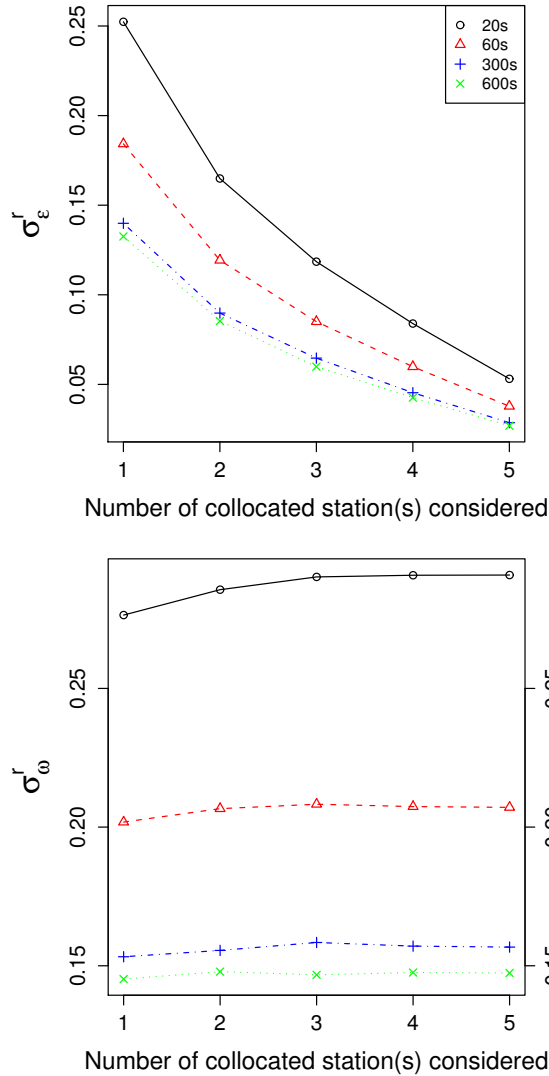


Figure 3.9: Relative sampling uncertainty [-] as a function of the number of collocated disdrometers and the temporal resolution for R values between 0.1 and 2 mm h⁻¹. The number of collocated instrument has a significant impact on $\sigma_{\varepsilon_{S_k}}^r$ (top) while the relative uncertainty σ_{ω}^r does not significantly depend on the number of sensors deployed (bottom).

with similar results. This experimentally demonstrates that Eq 3.13 is valid at least for the local climatology. Because the approximation used in Eq E.2 may cause problems when

the considered number of samples (denoted by n_s) is small [Stuart and Ord, 1994, p.351], this 2-month data set is too limited to check the validity of this approximation for higher R classes (the quantile 95% is about 3 mm h^{-1}). Eq E.2 will nevertheless be assumed to hold for higher R (and other quantities of interest). In order to provide reliable quantification of the relative sampling uncertainty, σ_ω^r is calculated only if there are more than 30 values in a given class ($n_s \geq 30$). Comparison between results obtained by considering data from two or three Parsivels shows that working with only two has a limited effect on the derived sampling errors. Therefore, the analyses are conducted on data from Parsivels 01 and 02 which have the longest record.

Because time resolution has a strong impact, σ_ω^r is estimated at 11 different time resolutions ranging from 20 s to 1 h. The analyses were also conducted for three typical frequencies of weather radar systems: 2.8 GHz (S-band), 5.6 GHz (C-band) and 9.4 GHz (X-band).

The sampling error has been investigated and quantified for TB rain gauges [e.g., Habib et al., 2001b; Ciach, 2003] as well as for Joss-Waldvogel disdrometer [e.g., Chandrasekar and Gori, 1991; Tokay et al., 2005]. Although our approach is similar to these last two (in particular by considering collocated stations as well as by using the standard deviation to quantify the sampling uncertainty), we focus on the relative sampling error per class of the considered quantity. Hence direct comparison with these studies is not possible.

3.4.3 Sampling uncertainty associated with total drop concentration estimates

Because the sampling uncertainty may vary with the total concentration of drops, the range of observed N_t values was divided into 9 non-equidistant classes in order to have a sufficient number of values in each class ($n_s \geq 30$). N_t values range from 0 to 2000 drops per cubic meter. Figure 3.10 presents the relative sampling uncertainty $\sigma_{\omega(N_t)}^r$ associated with N_t estimates from a single Parsivel. The corresponding values of the uncertainty for the different classes and temporal resolutions are provided in Table F.1 in Appendix F.

For N_t estimates, the relative sampling uncertainty is between 3 and 25 %. It is decreasing with increasing N_t classes and increasing time steps. For time steps longer than 300 s, the relative sampling uncertainty is below 10% independently of N_t . The highest values of $\sigma_{\omega(N_t)}^r$ are observed for the first class, i.e., for N_t below 50 drops per cubic meter. For low N_t values, a few missed drops will have a stronger effect on the uncertainty than for larger N_t values independently of the time resolution.

3.4.4 Sampling uncertainty associated with median-volume diameter estimates

Similarly to N_t , 10 non-equidistant classes of D_0 have been defined from 0.6 to 2.5 mm. The map of relative sampling uncertainty associated with D_0 estimates is presented in Figure 3.11 (the corresponding values of $\sigma_{\omega(D_0)}^r$ are provided in Table F.2 in Appendix F) according to the different D_0 classes and temporal resolutions. The relative sampling uncertainty associated

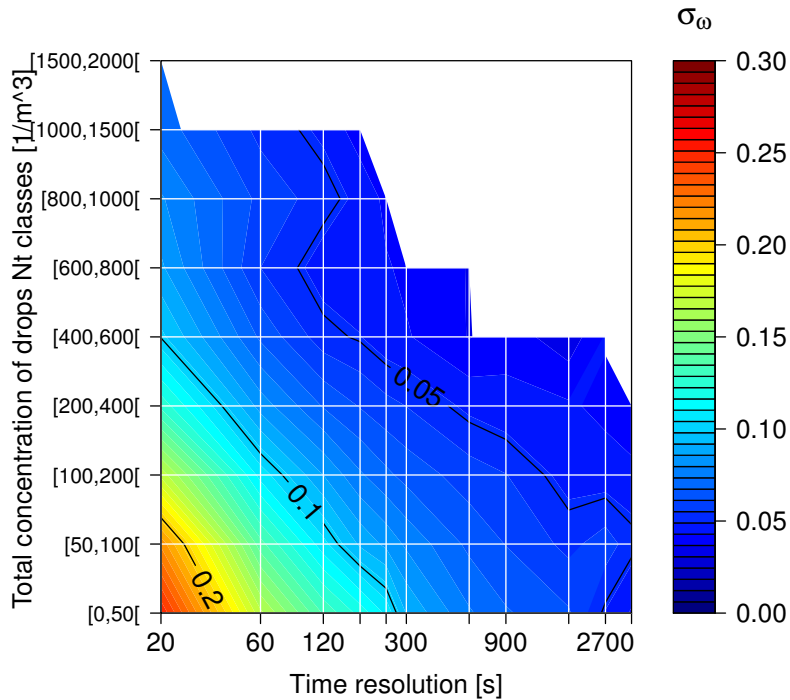


Figure 3.10: Relative sampling uncertainty associated with estimates of total concentration of drops from a single Parsivel as a function of total drop concentration and temporal resolution. The white area corresponds to pixels with less than 30 values to estimate $\sigma_{\omega(N_t)}^r$. X-axis is logarithmic. Note that the color scale stops at 0.30 while contour lines figures the whole range of values.

with D_0 estimates is between 1 and 27%. $\sigma_{\omega(D_0)}^r$ is decreasing for decreasing D_0 and increasing time steps. For D_0 about 1.75 mm and below, the relative sampling uncertainty is below 20% independently of the temporal resolution. Figure 3.12 presents the median of the number of drops with a diameter D larger than D_0 for each D_0 class. This number decreases with increasing D_0 classes, illustrating the decreasing number of big drops (recall that D_0 is sensitive to big drops, see Eq. 3.4). The larger sampling uncertainty for small time steps (i.e., 20 and 60 s) and higher D_0 classes is hence due to the limited number of drops in these classes. Therefore, a few missed big drops will induce a large relative sampling uncertainty.

3.4.5 Sampling uncertainty associated with rain rate estimates

Following the same approach, 9 rainfall intensity classes have been defined from 0.1 mm h^{-1} to 30 mm h^{-1} . Due to the large number of low rain rate values, the first classes are thinner than the higher ones. Figure 3.13 presents the relative sampling uncertainty $\sigma_{\omega(R)}^r$ associated with rain rate measurements from a single sensor for both types of instrument (i.e., Parsivel and TB rain gauges). The corresponding values of the relative sampling uncertainty for the different classes and temporal resolutions are provided in Table F3 in Appendix F.

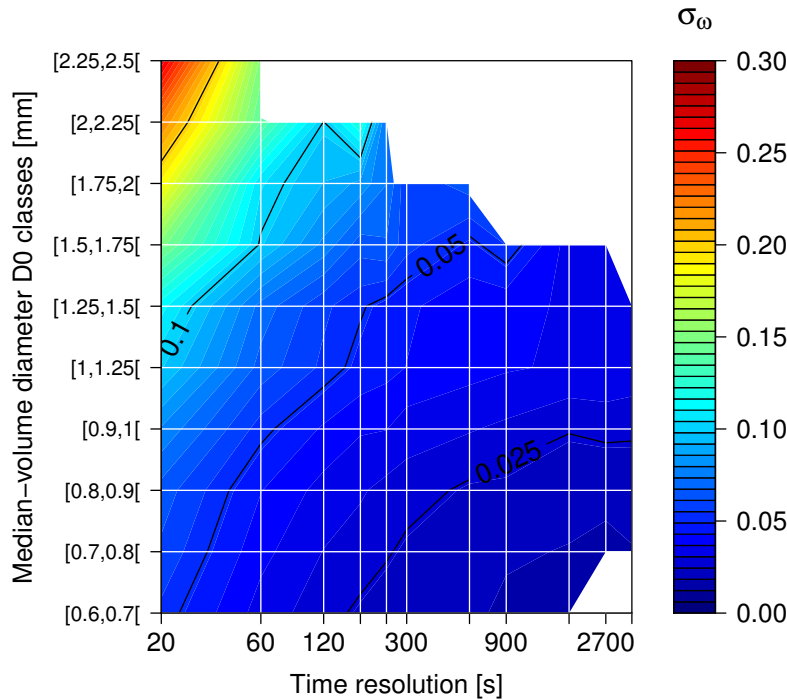


Figure 3.11: Same as Figure 3.10 for the median-volume diameter estimated from a single Parsivel.

For Parsivel measurements, the relative sampling uncertainty is between 7 and 25 %. It is globally decreasing with increasing rain rate classes and increasing time steps. At a temporal resolution of 300 s, the relative sampling uncertainty is below 12% for all R values. At high temporal resolutions, e.g., 20 s, the sampling uncertainty is below 20% for rain rates higher than 6 mm h^{-1} and between 20 and 25% for light rain rates, i.e., below 6 mm h^{-1} . Figure 3.14 presents the median of the number of drops measured as well as the mean diameter as a function of R classes at a 60 s temporal resolution. As expected the measured number of particles is increasing with increasing rain rates. The larger values of sampling uncertainty at high temporal resolutions and for low R values can be related to the lower number of drops measured compared to higher R values. Therefore, $\sigma_{\omega(R)}^r$ is more sensitive to a difference of a few drops for low than for large R values. The slight increase for higher classes is due to the influence of a few big drops (with low concentrations) as illustrated by the increasing mean diameter in Figure 3.14. Similarly, the decrease of $\sigma_{\omega(R)}^r$ for increasing time steps can be related to the larger number of drops for larger time steps (see Table 3.1). The relative sampling uncertainty is then less affected by a few missed drops.

For TB rain gauge measurements, the relative sampling uncertainty is between 4 and 110%. $\sigma_{\omega(R)}^r$ shows a similar pattern with decreasing $\sigma_{\omega(R)}^r$ for increasing rain rate classes and time steps. TB rain gauge measurements are globally affected by a sampling uncertainty larger than Parsivel's one for temporal resolutions below 15 min (e.g., above 25% for R below 4 mm h^{-1} for

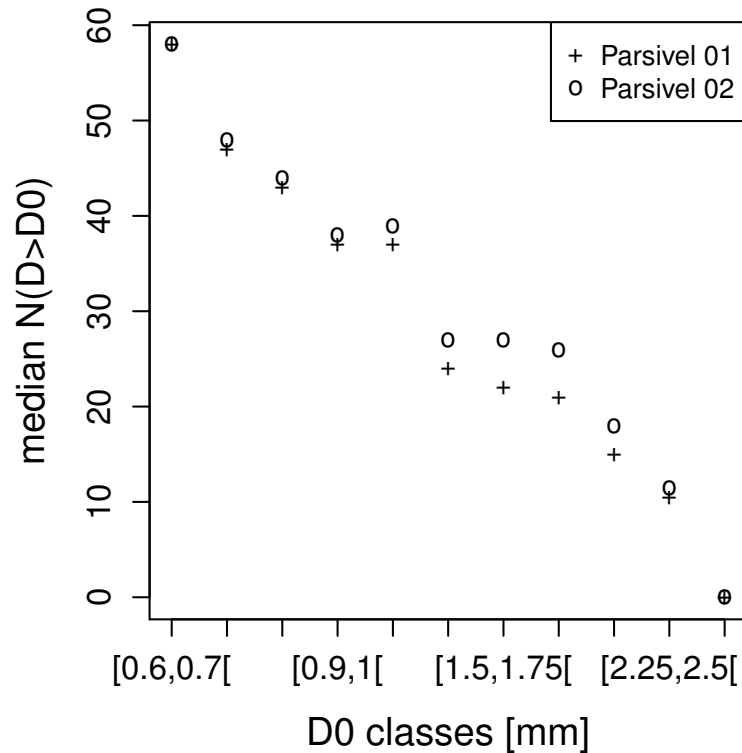


Figure 3.12: Median of the number of drops with $D > D_0$ measured by both Parsivels over the 15 months as a function of D_0 classes. N depends on the sampling area (54 cm^2) and the considered temporal resolution (here 60 s).

temporal resolutions below 5 min). Large sampling uncertainty at low rainfall rates and short integration intervals is directly related to the quantization inherent to the instrument, caused by the discrete volume of its buckets. This strong quantization results in numerous identical values, explaining the identical 110% uncertainty values at short time steps and low R values (quantile estimates are affected by a lot of identical values in the sample). For example, the resolution of a rain rate measurement corresponding to one tip of 0.1 mm is 6 mm h^{-1} for a temporal resolution of 60 s. For temporal resolution about 15 min, the sampling uncertainty affecting Parsivel and TB rain gauge is similar. For time steps about 30 min or larger, TB rain gauge measurements are affected by a smaller sampling uncertainty than Parsivel ones. For instance, at a temporal resolution of 24 h (not shown in Figure 3.13), $\sigma_{\omega(R)}^r$ for Parsivel (8%) is about 4 times higher than the one for TB rain gauges (2%).

3.4.6 Sampling uncertainty associated with radar reflectivity estimates

Z_h is expressed in dBZ in the subsequent analyses. The map of sampling uncertainty according to the different Z_h classes and temporal resolutions is presented in Figure 3.15 and the corresponding values of $\sigma_{\omega(Z_h)}^r$ are provided in Table F4 in Appendix F. For Z_h below 40 dBZ,

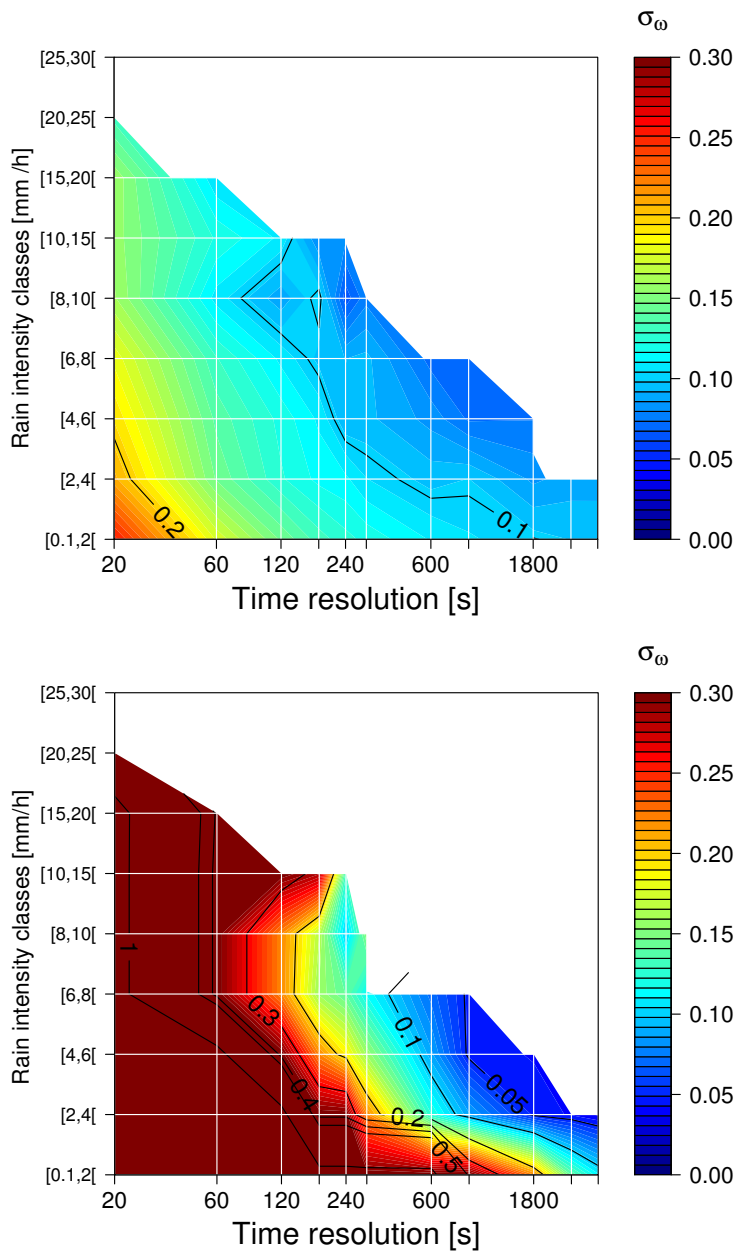


Figure 3.13: Same as Figure 3.10 for rain rate measurements of a single Parsivel (top) and a single TB rain gauge (bottom).

$\sigma_{\omega(Z_h)}^r$ is below 14% for all the investigated temporal resolutions. For Z_h above 40 dBZ, the relative sampling uncertainty is between 3 and 17%. For time steps about 300 s or larger, $\sigma_{\omega(Z_h)}^r$ is below 7% for X-band independently of Z_h values (see Table E4 in Appendix F). The relative sampling uncertainty associated with Z_h estimates is globally decreasing for increasing time steps as well as for increasing Z_h values up to about 30 dBZ. For Z_h values higher than 30 dBZ, $\sigma_{\omega(Z_h)}^r$ increases up to 17%.

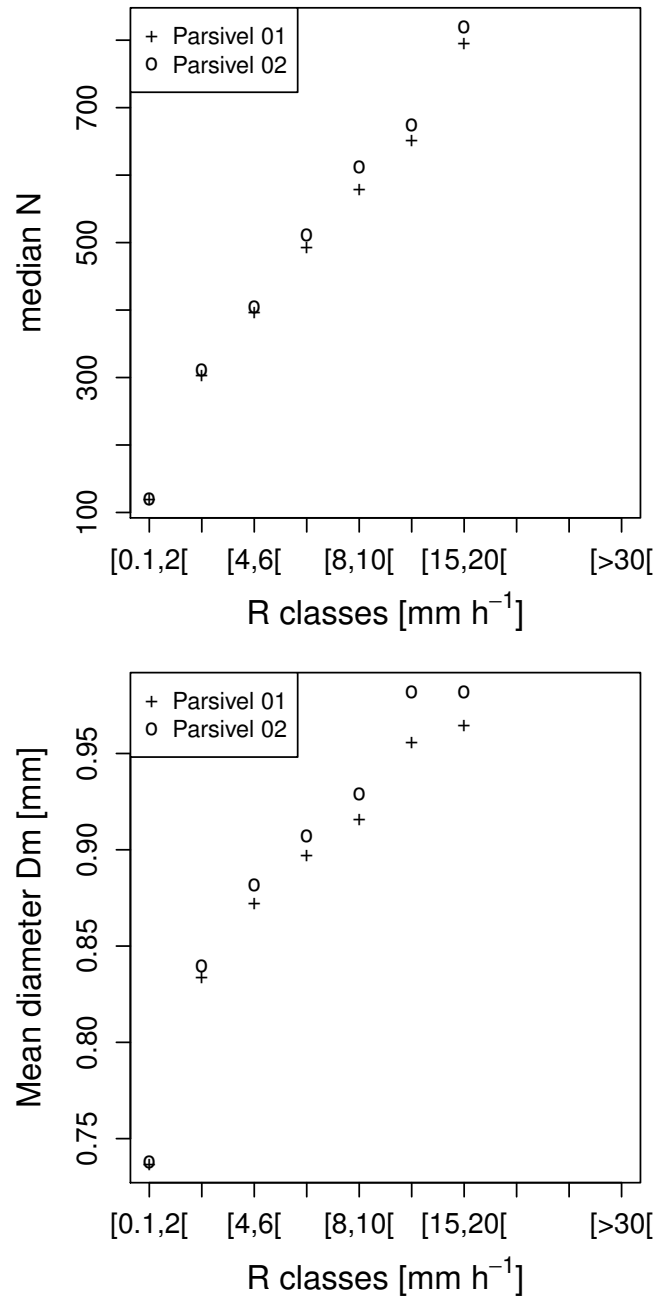


Figure 3.14: Median of the number of drops measured by both Parsivels (top) and mean diameter [mm] (bottom) over the 15 months as a function of R classes. N depends on the sampling area (54 cm^2) and the considered temporal resolution (here 60 s). For consistency with Figure 3.13, statistical descriptors associated with classes characterized by less than 30 measurements are not drawn.

Figure 3.16 presents the median of the number of drops measured over the 15 months as well as the mean diameter as a function of Z_h classes at a temporal resolution of 60 s. Similarly to

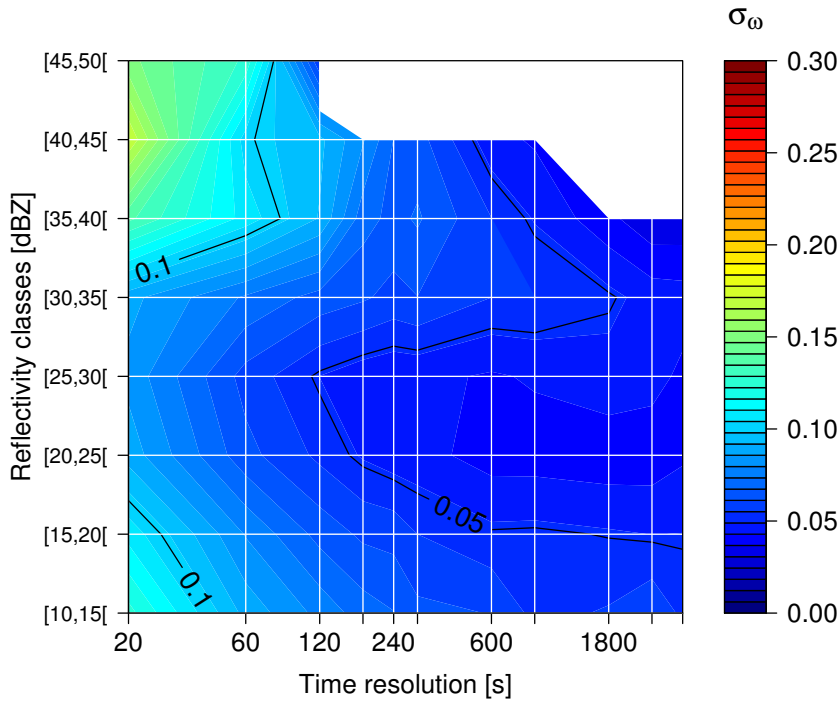


Figure 3.15: Same as Figure 3.10 for the radar reflectivity at horizontal polarization estimated from a single Parsivel at X-band.

R , small Z_h values are affected by a larger relative sampling uncertainty because of the lower number of drops measured by the instrument for low Z_h values (see Figure 3.16). When averaging over longer time steps, the number of drops measured by the instrument is increasing (see Table 3.1). Hence, the relative sampling uncertainty is less sensitive to a few missed drops. Because Z_h is a moment of higher order (~ 6) than R (~ 3.67), it is more sensitive to the very limited number of big drops. The mean diameter according to each Z_h class presented in Figure 3.16 shows the presence of larger drops in higher Z_h classes. Therefore, the increase of the sampling uncertainty for Z_h values above 30 dBZ is due to the influence of a few missed big drops (which have low concentrations).

The pattern of relative sampling uncertainty, presented in Figure 3.15 at X-band, is very similar at C- and S-band, with $\sigma_{\omega(Z_h)}^r$ ranging from 3(2) to 20(12)% for C-(S-)band. All the values are provided in Table F.4 in Appendix F.

3.4.7 Sampling uncertainty associated with differential reflectivity estimates

Polarimetric capabilities have been shown to be of great added-value for weather radar systems [e.g., Bringi and Chandrasekar, 2001]. As explained in Section 3.4, the data set considered in this paper corresponds to limited values of specific attenuation and specific differential phase (even at X-band). The focus will therefore be on the differential reflectivity Z_{dr} . Figure 3.17

3.4. Quantification of the sampling uncertainty

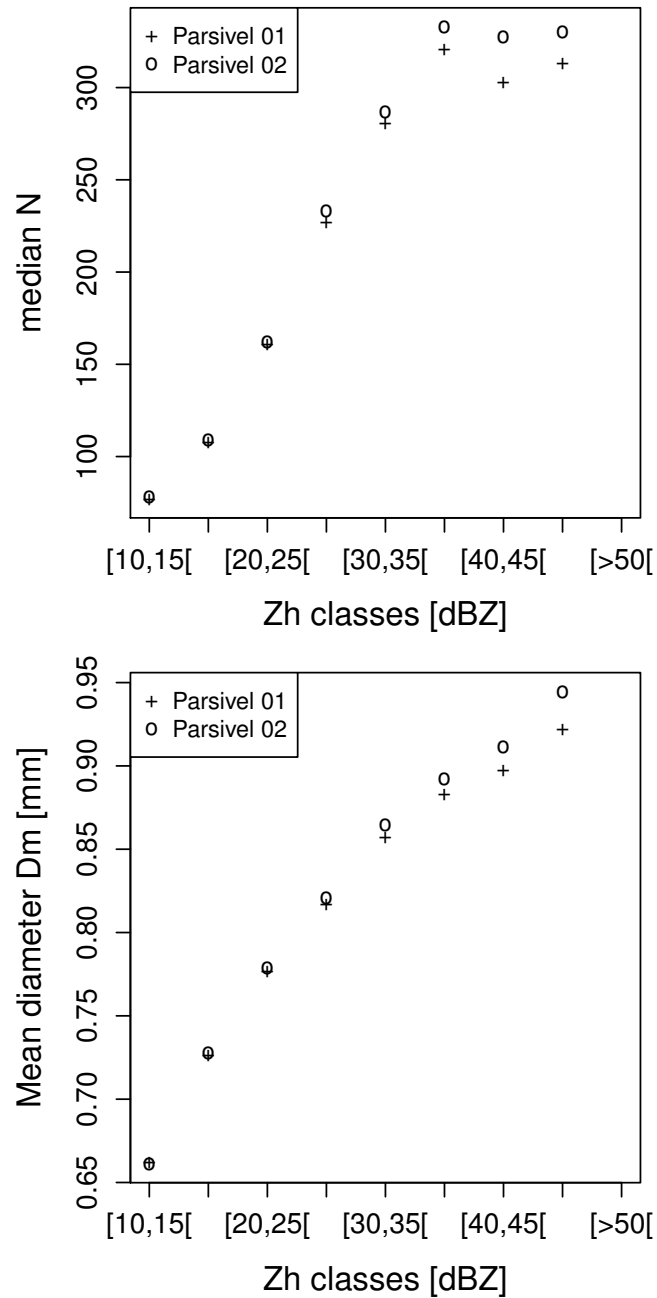


Figure 3.16: Same as Figure 3.14 for Z_h .

presents the relative sampling uncertainty as a function of Z_{dr} classes and the temporal resolutions. The corresponding values are provided in Table E5 in Appendix F. The relative sampling uncertainty associated with Z_{dr} estimates is ranging from 8 to 50%. $\sigma_{\omega(Z_{dr})}^r$ is below 31% for Z_{dr} below 0.5 dB independently of the temporal resolution. For time steps below 5 min and for Z_{dr} higher than 1 dB, $\sigma_{\omega(Z_{dr})}^r$ is above 38%.

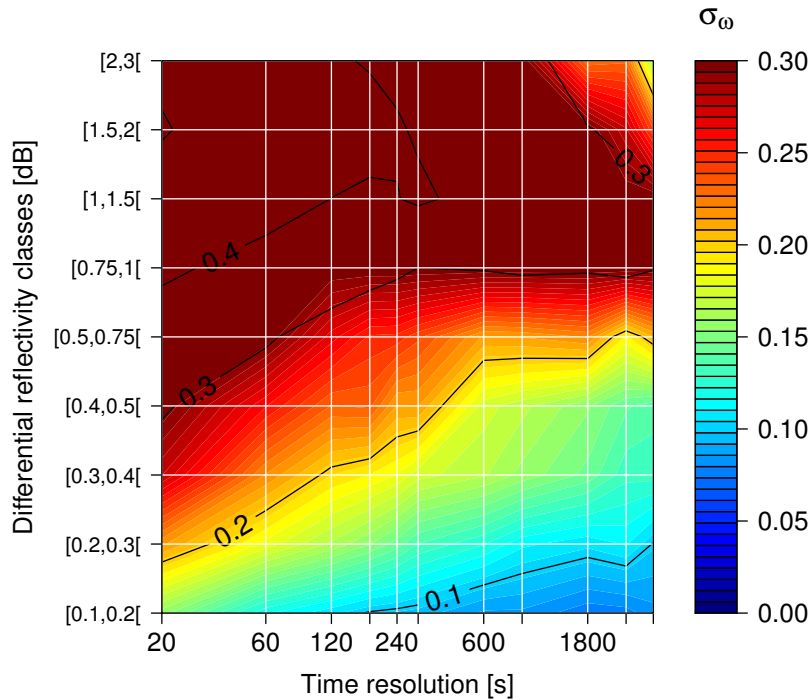
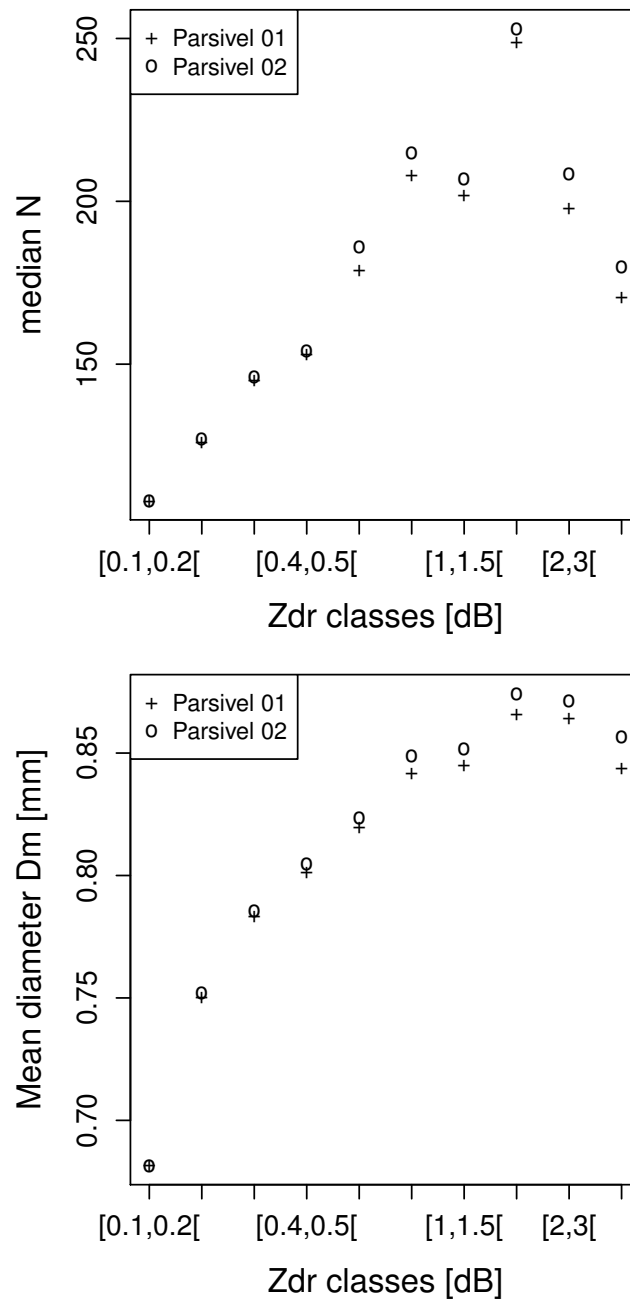


Figure 3.17: Same as Figure 3.10 for the differential reflectivity estimated from a single Parsivel at X-band.

Because the shape of the probability density function is better defined for larger samples, the relative sampling uncertainty on Z_{dr} is decreasing with increasing time steps. The pattern of the relative sampling uncertainty as well as the range of $\sigma_{\omega(Z_{dr})}^r$ values, are clearly different from the ones presented for R and Z_h . Contrary to Z_h , $\sigma_{\omega(Z_{dr})}^r$ is strongly increasing for increasing Z_{dr} classes. The median of the number of drops as well as the mean diameter as a function of Z_{dr} classes are presented in Figure 3.18 at a temporal resolution of 60 s. The increase of the mean diameter associated with the decrease of the median of the number of drops for the higher Z_{dr} classes indicates that large Z_{dr} values are due to big oblate drops which have very low concentrations. Therefore, missing one or a few of these big drops has a strong impact on the the uncertainty in the shape of the empirical probability density function and therefore on the uncertainty in Z_{dr} . The values of $\sigma_{\omega(Z_{dr})}^r$ at C- and S-band are also very similar (see Table E.5 in Appendix F).

3.5 Conclusion

The quantification of the variability of the DSD in time and space is of great interest for many environmental fields and in particular for precipitation estimation using remote sensing. A reliable quantification of the DSD variability must take into account the variability due to the sampling process of DSD measurement. To address this issue for Parsivel measurements,

Figure 3.18: Same as Figure 3.14 for Z_{dr} .

Chapter 3. Sampling uncertainty

two collocated Parsivels as well as two TB rain gauges have been deployed in Lausanne, Switzerland. The experiment ran for 15 months. The difference between the values recorded by both instruments only depends on the sampling process. Using this large data set, the relative sampling uncertainty associated with two quantities characterizing the DSD, namely the total concentration of drops N_t and the median-volume diameter D_0 , is quantified as a function of the temporal resolution and their respective values. Similarly, the sampling uncertainty associated with the estimates of rain rate R , radar reflectivity Z_h and differential reflectivity Z_{dr} (all weighted moments of the DSD) is quantified at different weather radar frequencies (X-, C- and S-band).

The relative sampling uncertainty associated with N_t estimates is below 25% and is globally decreasing with increasing N_t values and increasing time steps. D_0 shows a different pattern of sampling uncertainty with higher values of $\sigma_{\omega(D_0)}^r$ for higher D_0 values and shorter time steps, for which it can reach about 27%. On average, for D_0 smaller than 1 mm, $\sigma_{\omega(D_0)}^r$ is below 8%. It has to be noticed that similar results have been obtained for the mass-weighted diameter D_m . For R estimates, the relative sampling uncertainty associated with Parsivel is below 25% contrary to TB rain gauges for which $\sigma_{\omega(R)}^r$ can reach 110% at high temporal resolution (below 120 s). For both types of instruments, $\sigma_{\omega(R)}^r$ is decreasing for increasing time steps. For temporal resolution of about 30 min or above, TB rain gauge measurements are affected by a smaller sampling uncertainty than Parsivel ones for rain rates higher than 2 mm h⁻¹.

At X-, C- and S-band, the sampling uncertainty associated with Z_h estimates (in dBZ) exhibits a similar pattern to R . For Z_h values lower than 35 dBZ, $\sigma_{\omega(Z_h)}^r$ is below 12% for time steps below 1 h. For Z_h values between 40 and 50 dBZ, $\sigma_{\omega(Z_h)}^r$ is below 17%. Concerning Z_{dr} , its estimates are affected by a larger sampling uncertainty ranging from 8% to about 50%. The increase of $\sigma_{\omega(Z_{dr})}^r$ with Z_{dr} can be related to the strong influence of the very low concentration of big oblate raindrops in the estimation of Z_{dr} . For time steps smaller than 5 min and Z_{dr} values below 0.75 dB, $\sigma_{\omega(Z_{dr})}^r$ is smaller than 36%. For Z_{dr} values above 1 dB, the relative sampling uncertainty is between 16 and 50%.

The quantification of the sampling uncertainty affecting measurements from the Parsivel optical disdrometer is a crucial step to be able to accurately quantify the natural variability of the DSD from Parsivel measurements, in particular at small scales. Because the data set is only representative of light to moderate rainfall in a temperate climate, the present analysis needs to be extended to heavy rain.

4 Spatial structure of the DSD at the radar subgrid scale¹

4.1 Introduction

The estimation of rainfall using remote sensing techniques requires a minimum knowledge of the microstructure of rain (e.g., the concentration, size and shape of raindrops). A statistical tool to summarize some of this information is the (rain)drop size distribution, DSD hereafter, which is the concentration of raindrops according to their respective size in a sampling volume. As the DSD is highly variable in time and space [Jameson and Kostinski, 2001], the understanding of the spatial structure of the DSD, i.e., how the DSD fields are organized (or not) in space, is crucial to be able to quantify the error structure associated with remote sensing of precipitation.

While rain gauges only provide information about some integral quantities of the DSD (namely the rain rate and rain amount), disdrometers provide measurements of the DSD, which allow a deeper insight into rainfall microstructure. Significant work has been done during the last decades focusing on the spatial structure of the rain rate [e.g., Ciach and Krajewski, 2006; Villarini et al., 2008], i.e., the flux of water arriving at a surface during a specific time, which is a quantity derived from the DSD of primary importance for many environmental fields.

During the last decade, the deployment of networks of disdrometers has become a common setup to investigate the spatial structure of the DSD. Miriovsky et al. [2004] have pointed out the difficulty to quantify the variability of the DSD, especially when using disdrometers of different types which are affected by different sampling uncertainties. This issue on sampling errors has been investigated by Krajewski et al. [2006] using collocated measurements. More recently, additional experiments have been reported using four Precipitation Occurrence Sensor Systems (POSS) and radar data [Lee et al., 2009] and three Joss-Waldvogel disdrometers [Tokay and Bashor, 2010]. Nevertheless, the limited spatial distribution of the instruments did not allow to fully characterize the spatial variability of the DSD. A network 16 optical

¹This chapter is adapted from Jaffrain, J. and A. Berne (in press): Quantification of the small-scale spatial structure of the raindrop size distribution from a network of disdrometers. *Journal of Applied Meteorology and Climatology*

disdrometers deployed over 8 sampling locations covering an area of about $4 \times 4 \text{ km}^2$ has recently been presented [Tapiador et al., 2010]. However, the analyses were focused on the rain rate and the radar reflectivity rather than on the DSD itself. Studies focusing on the modelling of the DSD in space have been reported in the literature [e.g., Berne and Uijlenhoet, 2005b; Lee et al., 2007]. More recently, Schleiss et al. [2009] and Schleiss et al. [2011] have proposed a geostatistical simulation framework to generate realistic intermittent DSD fields in time.

The objective of the present paper is to investigate a possible spatial structure of the DSD fields within an operational radar pixel (scale of about $1 \text{ km} \times 1 \text{ km}$) and to quantify it using a geostatistical approach (i.e., using variograms). Section 2 presents the experimental setup and the considered data while the method is detailed in Section 3. The spatial structure of the different quantities of interest (namely the total concentration of drops, the mass-weighted diameter and the rain rate) is presented in Section 4. Finally, Section 5 illustrates how this information can be used to quantify the error associated with the upscaling from point to areal measurements.

4.2 Experimental set up and data set

In order to quantify the spatial structure of the DSD, a network of 16 disdrometers (OTT-Parsivel, first generation) has been deployed in Lausanne, Switzerland, during 16 months over a $1 \text{ km} \times 1 \text{ km}$ area, which is the size of a typical operational weather radar pixel. The network is presented in detail in Chapter 2 and Jaffrain et al. [2011]. According to this configuration, the interdistance between pairs of disdrometers ranges from 85 to 800 m. The network has collected DSD spectra corresponding to 540 h of rain and a total rain amount of about 820 mm. In the following, a rainfall event is defined as a continuous rainy period of at least 15 min surrounded by continuous dry periods of at least 15 min. It has to be noticed that rain events with a rain amount lower than 1 mm are not considered. Among these events, only those for which all the 16 disdrometers collect data are considered. A tipping-bucket rain gauge was collocated with one of the disdrometer (Station 43, see Figure 2.3). Only the rain events for which rain amounts recorded by Station 43 deviate less than 10% from the one recorded by the rain gauge are considered. In the end, 36 rain events of different types are considered, assuming that the bias is also limited for the other stations of the network. From visual inspection of MeteoSwiss radar rainfall maps, these events are classified as convective, frontal or transitional and grouped accordingly. Despite this somehow arbitrary classification, the main goal is to cover a broad range of types of rainfall. For illustration, a typical radar rainfall map for a convective and a frontal rainfall event is presented in Figure 4.1.

Convective type rainfall is usually characterized by strong rainfall with a limited duration in time and a limited extension in space (i.e., few convective cells) while frontal rainfall is characterized by light rainfall widely spread over long durations. This provides three groups of rainfall events for which statistics at a 60-s temporal resolution are provided in Table 4.1. It has to be noticed that all data within a group of rainfall are considered all together. The

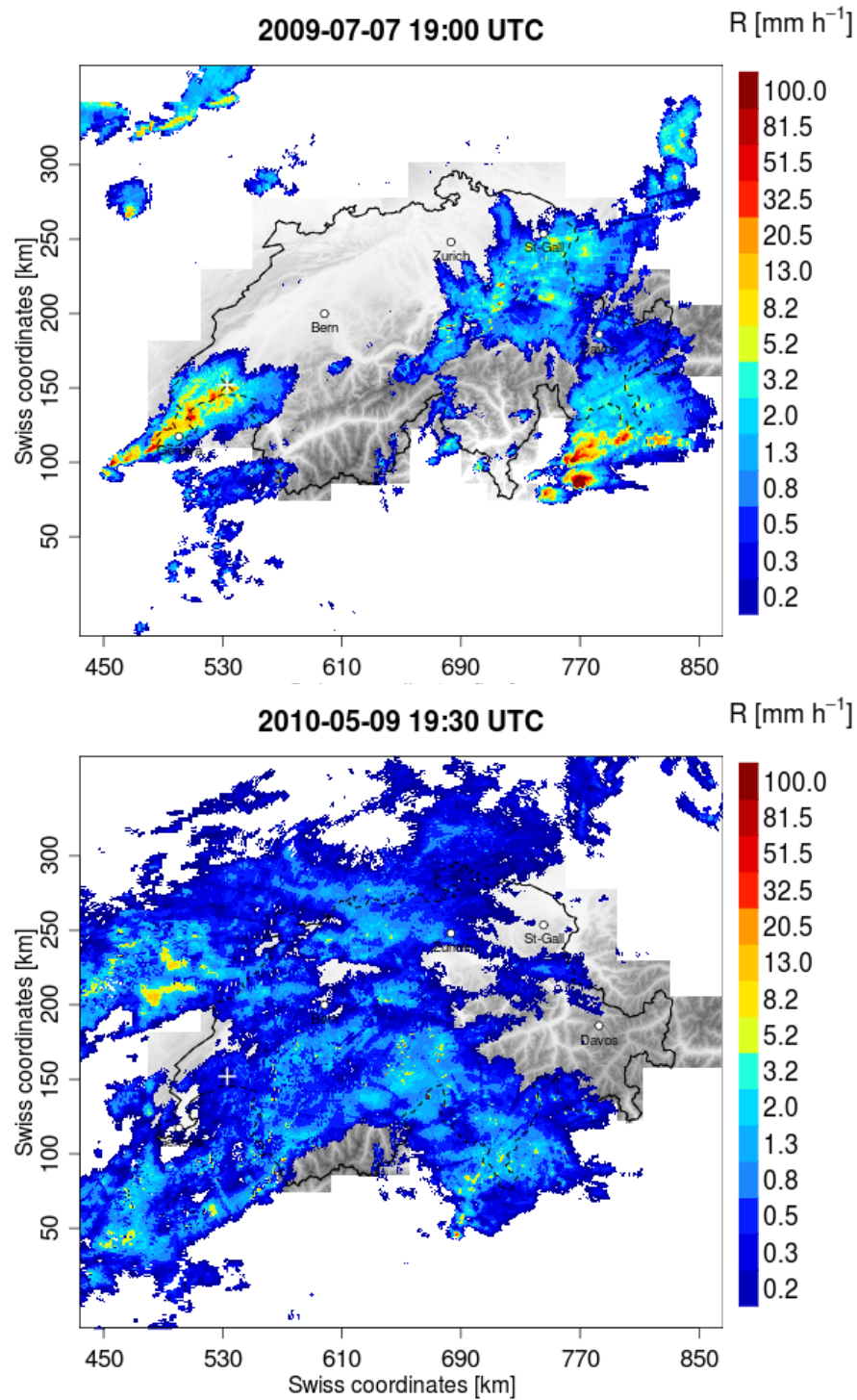


Figure 4.1: Radar rain-rate map to illustrate a convective (top) and a frontal (bottom) rainfall event. The black and white cross (at about X=530 km and Y=150 km) denotes the position of the network of disdrometers.

Chapter 4. Spatial structure of the DSD at the radar subgrid scale

convective, transitional and frontal groups consist of 9, 19 and 8 rainfall events for a total of 643, 3665 and 839 rainy minutes respectively. As expected, quantiles of rain rate values are increasing from frontal to convective rainfall events. For example, the median rain rate value for convective type events is about 2.42 mm h^{-1} while it is about 1.24 and 0.64 mm h^{-1} for transitional and frontal ones respectively. The averaged DSD spectrum of each group is

Table 4.1: Statistics of the three different groups of rainfall events at a 60-s temporal resolution.

	Convective	Transitional	Frontal
Number of events	9	19	8
Number of rainy minutes	643	3665	839
Rain amount averaged over the network [mm]	32.6	113.7	10.5
Mean of the averaged rain rate \bar{R} [mm h^{-1}]	3.05	1.86	0.75
$Q_{10\%}(\bar{R})$ [mm h^{-1}]	0.50	0.33	0.25
$Q_{50\%}(\bar{R})$ [mm h^{-1}]	2.42	1.24	0.64
$Q_{90\%}(\bar{R})$ [mm h^{-1}]	5.98	4.12	1.33

presented in Figure 4.2. It shows that convective rainfall events exhibit higher concentrations of drops larger than 0.8 mm than frontal ones. Moreover, larger drops are recorded in the convective group ($D_{max}=6.5 \text{ mm}$) than in the frontal one ($D_{max}=4.75 \text{ mm}$).

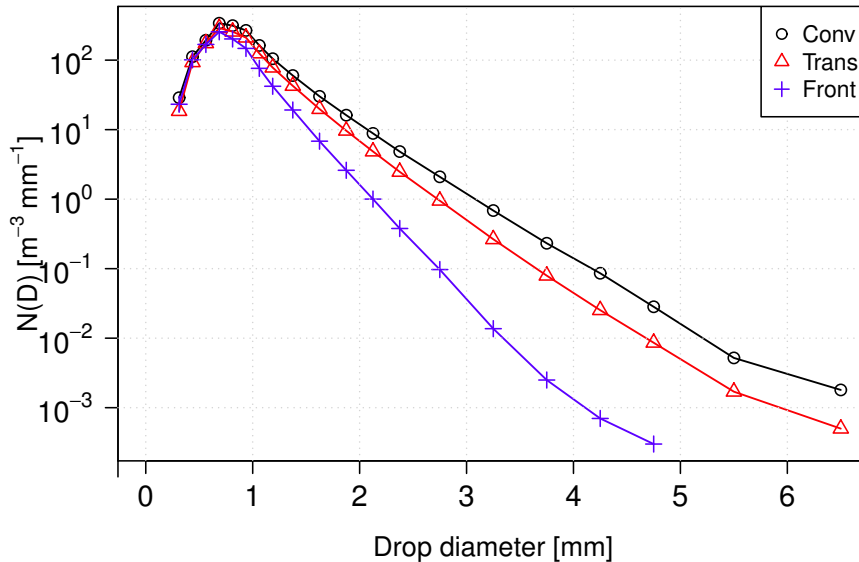


Figure 4.2: Drop size spectra integrated over all events within each group of rainfall types (i.e., convective, transitional and frontal). The symbols indicate the center of Parsivel diameter classes.

4.3 Methods

4.3.1 Framework and Assumptions

Prior to the analyses, the same filtering process as Jaffrain and Berne [2011] is applied on the data set, i.e., the filtered DSDs must satisfy the following conditions (see Section 3.2 for more details):

- all stations must record a rain rate higher than 0.1 mm h^{-1} at the considered temporal resolution
- drops outside $\pm 60\%$ around the terminal fall speed-diameter relationship are removed (see Eq 3.1) to filter out possible artifacts (from e.g., splashing, insects)

The raindrop size distribution, denoted $N(D)$ and expressed in $\text{m}^{-3} \text{mm}^{-1}$, can be defined as the product of the total concentration of drops N_t , which is the sum of all drops over the range of sampled diameters, and a probability density function $f(D)$. A commonly used descriptor of the center of the probability density function $f(D)$ is the mass-weighted diameter D_m which is the ratio of the fourth to the third moment of the DSD. Because it represents a flux of water through a given surface, the rain rate is of primary interest for many hydrological applications. Recall that the rain rate can be expressed as a function of the DSD:

$$R = 6\pi \cdot 10^{-4} \int_{D_{min}}^{D_{max}} N(D) v(D) D^3 dD \quad (4.1)$$

where $v(D)$ is the terminal fall speed (m s^{-1}) of a drop with a diameter D (mm).

The quantities of interest considered in the following (i.e., N_t , D_m and R) are all derived from the filtered DSDs. As highlighted in Figure 4.3 for rain rate values for the convective group, the distributions of the estimates of these quantities, in particular for N_t and R , are highly positively skewed due to a few large values. Classical tools to characterize the spatial structure like autocorrelation and variogram in geostatistics, are well suited for Gaussian-like distributed random fields, because the estimation of the mean is involved.

The logarithmic transform of the estimates of the different quantities helps obtain distributions closer to normality or at least more symmetrical (see Figure 4.3 bottom). Nevertheless, with this approach, the variability of the DSD within the typical weather radar pixel is quantified in the log space and needs to be back-transformed into linear space which is more relevant for environmental applications. Considering a stationary random function $U(x)$, x being a position vector, which has a lognormal distribution and defining $Y(x) = \ln[U(x)]$, the means m_Y and m_U , the variances σ_Y^2 and σ_U^2 and the covariances $C_Y(h)$ and $C_U(h)$ of Y and U are

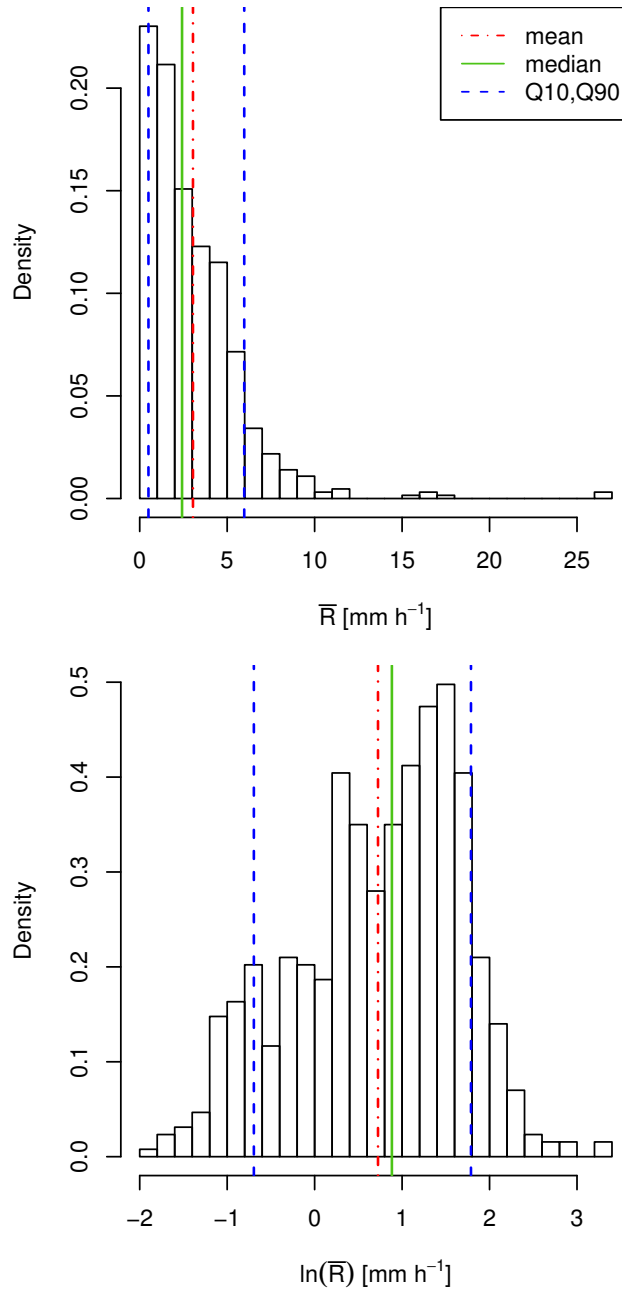


Figure 4.3: Distribution of \bar{R} values (i.e., averaged over the network) in linear space (top) and logarithmic space (bottom) for the convective rainfall group.

related as follows [Chilès and Delfiner, 1999, p. 103]:

$$m_U = \exp\left(m_Y + \frac{1}{2}\sigma_Y^2\right) \quad (4.2)$$

$$\sigma_U^2 = m_U^2 [\exp(\sigma_Y^2) - 1] \quad (4.3)$$

$$C_U(h) = m_U^2 \{\exp[C_Y(h)] - 1\} \quad (4.4)$$

where m_Y and σ_Y are the mean and the standard deviation of the population of Y values and h is a separation vector. We will assume that the statistical descriptors estimated from all Y sample values (i.e., considering all stations and all measurements of the period of interest) are representative of the population values.

4.3.2 Variogram estimation

The (semi)variogram is a key tool used in Geostatistics in order to investigate and quantify the spatial (or temporal) structure of a random function $U(x)$ [Matheron, 1965]. It is expressed as:

$$\gamma(h) = \frac{1}{2} E \{ [U(x+h) - U(x)]^2 \} \quad (4.5)$$

where E denotes the expectation, x is a position vector and h is a distance (or time) separation vector. The definition of the variogram requires $U(x)$ to be an intrinsic random function, i.e., its increments $U(x+h) - U(x)$ should be second-order stationary. From Eq 4.5, it is clear that the units associated with $\gamma(h)$ are the square of the ones associated with $U(x)$. The variogram of a regionalized variable $u(x)$, which is a realization of $U(x)$, can be calculated if the distribution of $u(x)$ values is known at every point of the spatial (or temporal) domain of interest. Because this condition is hard to fulfil in practice, the variogram is estimated from a sample that should be as large as possible for representativeness. The classical widely used sample variogram estimator, sometimes called "Matheron" estimator, is expressed as [Chilès and Delfiner, 1999]:

$$\hat{\gamma}(h) = \frac{1}{2N_h} \sum_{x_\beta - x_\alpha \approx h} \{ [u(x_\beta) - u(x_\alpha)]^2 \} \quad (4.6)$$

where N_h is the number of pairs (x_α, x_β) separated by a distance approximately equal to h . As the mean is involved, the quality of $\hat{\gamma}(h)$ estimates is influenced by the possible skewness of the distribution of the increment values. A more robust estimator based on the quantile variogram $\hat{\gamma}_p(h)$, as defined by Armstrong and Delfiner [1980], can be used:

$$\hat{\gamma}_p(h) = Q_p \left\{ \frac{1}{2} [u(x_\beta) - u(x_\alpha)]^2 \right\}_{x_\beta - x_\alpha \approx h} \quad (4.7)$$

where Q_p denotes the quantile with a probability $p \in]0, 1[$. Quantile variograms are all proportional to the classical variogram with proportionality factors being the quantiles of the distribution of a chi-square variable with one degree freedom χ_1^2 [Chilès and Delfiner, 1999] when U is bi-normal. For robustness, the median variogram estimator is used to estimate the variogram according to:

$$\hat{\gamma}(h) = \frac{\hat{\gamma}_{0.50}(h)}{Q_{0.50}(\chi_1^2)} \quad (4.8)$$

where $Q_{0.50}(\chi_1^2)$ is the median of a χ_1^2 distribution which is equal to 0.455.

The next step consists in back-transforming the variogram estimates from logarithmic space ($\gamma_Y(h)$) into the original space ($\gamma_U(h)$). For a stationary random function $U(x)$, the variogram $\gamma_U(h)$ and the covariance $C_U(h)$ at a distance lag h are linked in the following way:

$$\gamma_U(h) = \sigma_U^2 - C_U(h) \quad (4.9)$$

where σ_U is the standard deviation of U . From Eq 4.9, the covariance of $Y(x)$, with $Y(x) = \ln[U(x)]$, can be estimated from γ_Y at each distance lag h . Hence, the covariance of $U(x)$ can be derived from C_Y estimates using Eq 4.4. Finally, γ_U is derived from C_U estimates for each distance lag h .

In order to test if the spatial structure recorded over the field can be considered as isotropic (that is if it does not depend on the spatial direction), the variogram has been estimated in 4 directions (0, 45, 90 and 135°). The variograms estimated in each direction are similar, which indicates that the observed spatial structure is not dependent on the considered direction. Therefore, the isotropic assumption is hereafter considered as valid. According to the configuration of the network, 120 pairs of disdrometers are available at each time step. 15 classes of distance lag h have been defined ranging from 80 to 800 m with a class width of about 50 m. In the following, the average isotropic variogram for each rainfall group and each quantity of interest is estimated.

As we are considering the averaged variogram for each group of rainfall events, the number of values per interdistance class corresponds to the product between the number of disdrometer pairs in this class and the number of measurements for the considered group of events. Therefore, the number of values per class of distance is a function of the temporal resolution and of the size of the period considered. For instance, at 60 s (1 h) temporal resolution for the convective period, the number of values per class is ranging from 643 (22) for the class centered at $h = 750$ m to 10288 (352) for the class centered at $h = 225$ m. These values are the minimum, and frontal and transitional periods are characterized by larger numbers. It must be noted that the number of independent values is likely lower due to their autocorrelation in time within each rain event. We will assume that there are enough values in each distance class to have representative variogram estimates, as several (independent) events are considered together.

4.3.3 Spatial correlation estimation

As a first step in the estimation of the small-scale variability of the DSD, the Pearson correlation coefficient ($\rho_{i,j}(h)$) is calculated for each pair of disdrometers (i, j). Following Ciach and Krajewski [2006], a modified-exponential parametric model is fitted on the experimental correlation values. This model is expressed as:

$$\hat{\rho}(h) = c_0 \exp \left[- \left(\frac{h}{h_0} \right)^{s_0} \right] \quad (4.10)$$

where h is the separation distance between the two disdrometers, c_0 is the nugget parameter, h_0 is the e-folding distance and s_0 is the correlogram shape parameter. c_0 is the spatial correlation at distance lag zero and can be estimated from collocated measurements. Contrary to Ciach and Krajewski [2006], no collocated measurements are available for this campaign and consequently, three parameters (c_0 , h_0 and s_0) need to be fitted. A nonlinear least-squares method is considered, using the *nls* function of the software R [R Development Core Team, 2011], in order to estimate the three parameters of the empirical spatial correlation. For illustration, Figure 4.4 shows the spatial correlation estimates ($\rho_{i,j}(h)$) and the associated correlation model for R at a 60-s temporal resolution for the convective rainfall group.

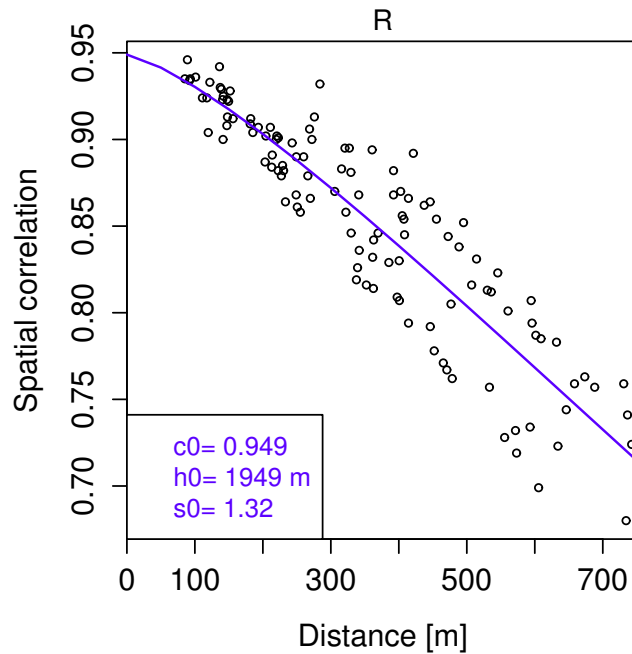


Figure 4.4: Spatial correlation $\rho(h)$ (\circ) and associated empirical model $\hat{\rho}(h)$ (solid line) for R for the convective rainfall types at a 60-s temporal resolution.

Because Pearson's correlation estimates can be affected by significant biases for non-normal data [e.g., Habib et al., 2001a], a logarithmic transformation was applied to the data prior to the calculation of correlation coefficient, as suggested by Stedinger [1981] for the estimation of correlation for multivariate streamflow data. Similarly to the variogram, $\hat{\rho}_{\log}(h)$ is then converted into $\hat{\rho}(h)$ in linear space using Eqs (4.2) to (4.4).

4.4 Results

4.4.1 Spatial correlations

As the correlation coefficient is the most widely used statistical tool in the literature for the quantification of the spatial variability of rainfall [e.g., Ciach and Krajewski, 2006; Villarini et al., 2008; Tapiador et al., 2010; Tokay and Bashor, 2010], this section is devoted to the estimation of $\hat{\rho}(h)$ for comparison purposes. Recently, Tokay and Bashor [2010] investigated the spatial variability of the raindrop size distribution using three Joss-Waldvogel disdrometers with interdistances of about 0.65, 1.05 and 1.7 km. The maximum distance lag of the network in the present study being about 800 m, the obtained characteristics of the spatial structure will nicely complement results from Tokay and Bashor [2010]. To check the consistency between the two studies, spatial correlation estimates can only be compared for the 0.65 km distance lag. In the present configuration of the network, two disdrometer pairs have interdistance closed to 650 m (646 and 658 m). At a 15-min temporal resolution, both studies exhibit similar correlation values for R (0.961 and 0.952 compared to 0.985). At a 60-s time resolution, we have a correlation of about 0.863 and 0.861, while Tokay and Bashor [2010] indicate about 0.945. These discrepancies can be due to the different climates investigated in the two studies, as well as to the fact that different types of disdrometer are used.

Ciach and Krajewski [2006] and Villarini et al. [2008] have estimated the three parameters of the correlation model (c_0 , h_0 and s_0 in Eq.4.10) for different temporal resolutions based on networks of tipping-bucket rain gauges. Villarini et al. [2008] provide a set of parametric equations describing the evolution of these three parameters with the temporal resolution. For illustration, these estimates are presented for 1 and 15 min temporal resolutions in Table 4.2. Our estimates are globally in better agreement with the one of Ciach and Krajewski [2006] than Villarini et al. [2008]. For instance, at a temporal resolution of 15 min, Ciach and Krajewski [2006] show values of about 0.998, 10.5 km and 1.45 while our estimates for transitional rainfall are about 0.988, 5.8 km and 1.61 respectively.

Table 4.2: c_0 , h_0 and s_0 estimates for rain rate R as proposed by Ciach and Krajewski [2006] and Villarini et al. [2008] at 1 and 15 min temporal resolutions. The third column shows the results from the present study for convective, transitional and frontal rainfall events respectively.

		[Ciach and Krajewski, 2006]	[Villarini et al., 2008]	Present study		
1 min	c_0 (-)	~0.996	0.510	0.949	0.953	0.922
	h_0 (km)	7.5	6.3	1.9	4.9	4.1
	s_0 (-)	1.10	0.41	1.32	1.11	1.01
15 min	c_0 (-)	~0.998	0.980	0.983	0.988	0.970
	h_0 (km)	10.5	94.4	2.9	5.8	16.7
	s_0 (-)	1.45	0.92	1.78	1.61	0.94

These differences can have various origins such as: the different types of instruments, the accuracy of the instruments, the configuration of the network (interdistances), the size of

the data set and the different climatologies due to the different locations. Nevertheless, these spatial correlations can be considered to be in reasonable agreement, which shows the consistency of the correlation values estimated from our data set with the ones presented in the literature. The variogram being more general than the covariance and the correlation, we will use the former to investigate the spatial structure of the DSD field.

4.4.2 Variograms

Averaged spatial structure

Isotropic variograms of the different quantities of interest (N_t , D_m and R) are estimated for the different types of rainfall (convective, transitional and frontal). Figure 4.5 presents the sample variogram of N_t for each rainfall type at a 60-s temporal resolution. It is clear that the network is not spatially extended enough to capture the *range* of the variogram (corresponding to the decorrelation distance). This is consistent with previous studies: typical ranges of about 5 km have been reported for radar reflectivity measurements at a 1-min temporal resolution in Mediterranean rainfall [Berne et al., 2004]; in a more recent experiment, based on reflectivities calculated from DSD measurements collected in Spain, the decorrelation distance was not reached at a distance lag of about 4 km [Tapiador et al., 2010]. However, our results also clearly show that there is a spatial structure in the DSD field (i.e., that the field is organized and not randomly varying) even at such a small scale (interdistances below 800 m).

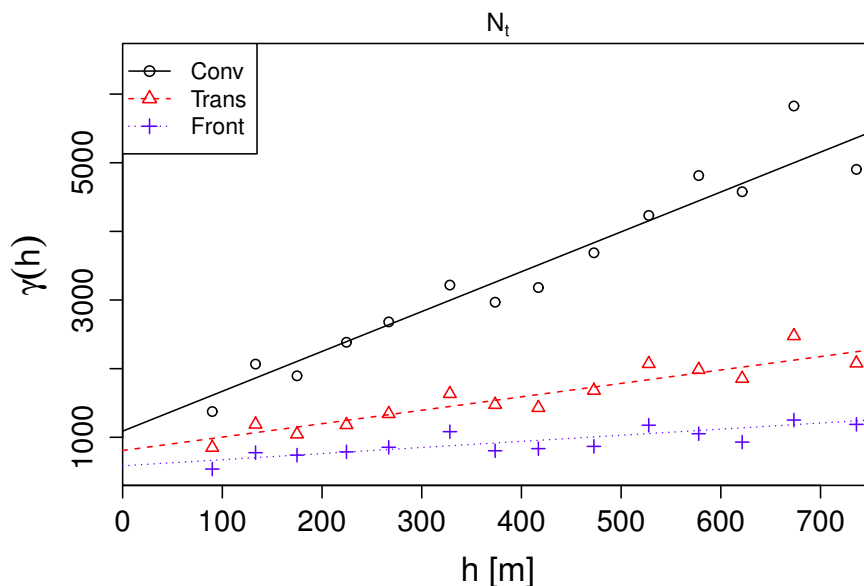


Figure 4.5: Sample variogram and fitted linear variogram model for N_t for the three rainfall types at a 60-s temporal resolution. The units associated with $\gamma(h)$ are m^{-6} . The X axis shows the interdistance h classes (m).

In terms of rainfall types, the variability observed over the monitored area is larger for convec-

tive events than for transitional and for frontal ones. For example, for an interdistance of about $h = 225$ m, the variogram value is about 2384.5, 1181.5 and 787.8 m^{-6} for convective, transitional and frontal type rain events respectively at a 60-s temporal resolution. This corresponds to an average difference of about 48.8, 34.4 and 28 drops per m^{-3} between two locations 225 m away.

To ease the comparison between rainfall events of different types, a variogram model was fitted on each empirical variogram. Because the range is not reached at the scale of the network, a linear variogram model is used. The high values of the coefficient of determination (ρ^2) confirm the goodness of fit of this linear model to the experimental variogram values. For instance, ρ^2 is about 0.91, 0.90 and 0.74 for the rain rate at a 60-s temporal resolution for convective, transitional and frontal rain events, respectively. The linear models are considered valid up to 800 m and the authors recommend not to extrapolate these models to much larger interdistance classes. It has to be noticed that variogram models have been adjusted using the *gstat* package [Pebesma, 2004]. Each linear model is characterized by two parameters: the *nugget* and the *slope*. The *slope* parameter indicates how fast $U(x)$ is varying with the distance lag. The *nugget*, similarly to c_0 for spatial correlation, quantifies the variability at very short distance lags (with respect to the minimum distance lag of the network). The nugget effect is explained by the possible variability of the considered process at interdistances smaller than the minimum interdistance in the network (all micro-scale variability, below 80 m in our case) and/or measurement errors. The linear model fitted on each sample variogram is also plotted in Figure 4.5 and the fitted values of nugget and slope are summarized in Table 4.3. Figures 4.6 and 4.7 show the same information for D_m and R .

Although they can not be directly compared, preliminary analyses show that the sampling uncertainty previously quantified (see Section 3) is consistent with the estimated nugget values. Indeed, the nugget must be larger than the sampling uncertainty because it includes all other sources of error. The sampling uncertainty is about $1/4^{\text{th}}$ of the nugget for N_t and R while for D_m this proportion is larger. Future work will further investigate this issue question.

Figures 4.5-4.7 show that there is a spatial structure at this scale for all the quantities of interest. Moreover and as intuitively expected, the nugget and slope parameters are increasing from frontal to transitional to convective events. For N_t for instance, the nugget (slope) of the transitional and frontal group represents about 74% (34%) and 54% (15%) of the one estimated for the convective group. These percentages for D_m exhibit similar values while the differences between convective and frontal parameters for R are larger. For example, the nugget (slope) parameter for frontal events represents about 4% (1%) of the one for convective events. The nugget explains a larger part of the total variability (interpreted as a stronger influence of the measurement error) for frontal than for transitional and convective events. In order to test if the slopes of the variogram models are significantly different from zero, especially for frontal rainfall which exhibits smaller slope values than convective and transitional rainfall, the p-value probability of a Student t-test has been computed. It shows that, at a 60-s temporal resolution, all the slope values observed for the different quantities are significantly (at a 1%

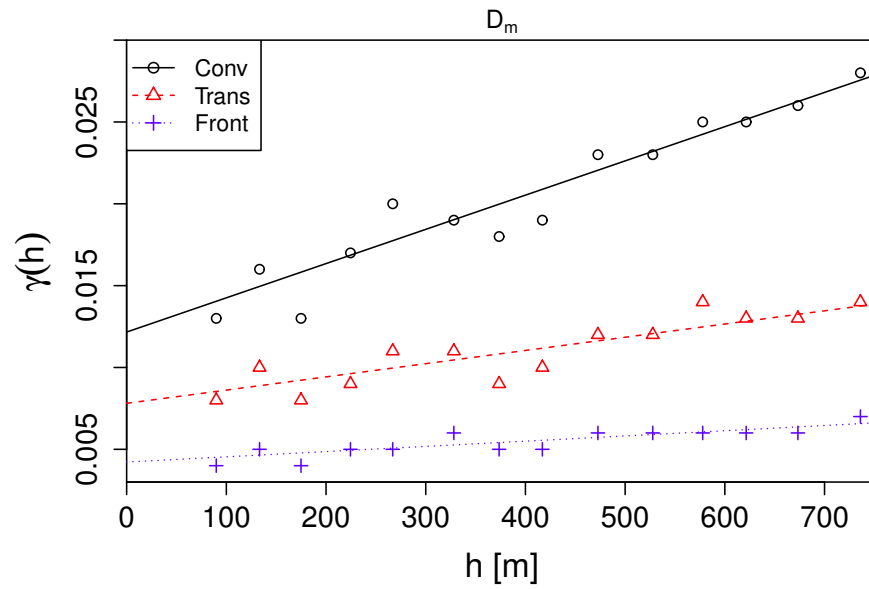


Figure 4.6: Same as Figure 4.5 for D_m . The units associated with $\gamma(h)$ are mm^2 .

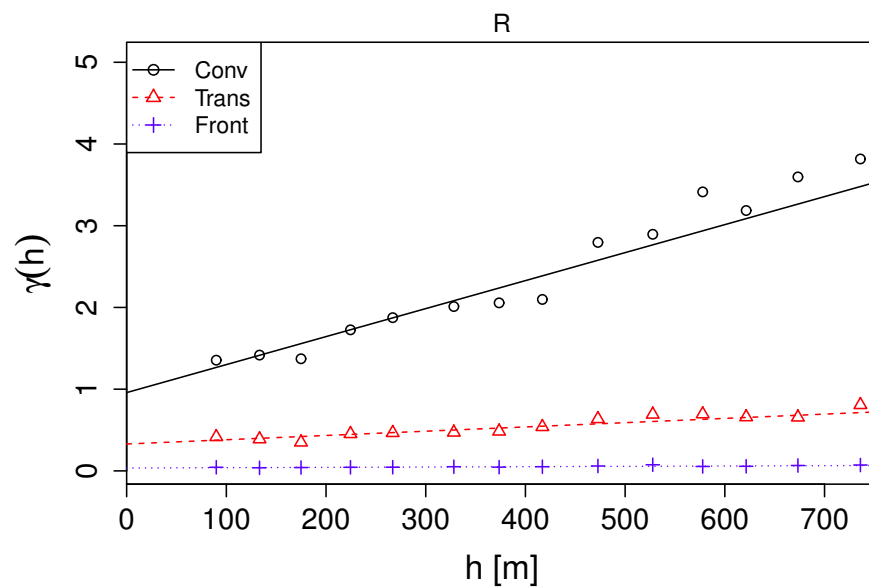


Figure 4.7: Same as Figure 4.5 for R . The units associated with $\gamma(h)$ are $\text{mm}^2 \text{h}^{-2}$.

confidence level) different from zero.

Influence of the temporal resolution

The variogram has been estimated and a linear model has been fitted at 7 temporal resolutions ranging from 60 s to 1 h. The evolution of the fitted nugget and slope values is presented in Figures 4.8, 4.9 and 4.10 for N_t , D_m and R respectively. Independently of the quantity of

Chapter 4. Spatial structure of the DSD at the radar subgrid scale

Table 4.3: Variations of the two parameters (nugget and slope) of the linear variogram model as a function of rainfall type for each quantity of interest at a 60-s temporal resolution. The coefficient of determination ρ^2 between the experimental variogram values and the associated linear model is as well presented. For transitional and frontal groups, values in brackets shows the values of the parameters expressed as a percentage of the ones for the convective group.

	Parameters	Convective	Transitional	Frontal
N_t	Nugget (m^{-6})	1089.47	807.21 (74%)	585.16 (54%)
	Slope ($\text{m}^{-6} \text{m}^{-1}$)	5.81	1.96 (34%)	0.89 (15%)
	ρ^2 (-)	0.93	0.87	0.65
D_m	Nugget (mm^2)	$1.22 \cdot 10^{-2}$	$7.80 \cdot 10^{-3}$ (64%)	$4.22 \cdot 10^{-3}$ (35%)
	Slope ($\text{mm}^2 \text{m}^{-1}$)	$2.09 \cdot 10^{-5}$	$8.07 \cdot 10^{-6}$ (39%)	$3.19 \cdot 10^{-6}$ (15%)
	ρ^2 (-)	0.93	0.79	0.80
R	Nugget ($\text{mm}^2 \text{h}^{-2}$)	0.96	0.33 (34%)	0.04 (4%)
	Slope ($\text{mm}^2 \text{h}^{-2} \text{m}^{-1}$)	$3.43 \cdot 10^{-3}$	$5.22 \cdot 10^{-4}$ (15%)	$4.03 \cdot 10^{-5}$ (1%)
	ρ^2 (-)	0.91	0.90	0.74

interest, there is a strong decrease in the nugget and slope values until a temporal resolution of 600 s, followed by a much more limited decrease. The slope of the variogram decreases with increasing temporal resolution. Slope values significantly different (at 10% significance level) from zero are observed for temporal resolutions up to 600 s (10 min) for D_m and R , and up to 1800 s (30 min) for N_t . The respective evolution of the nugget and of the respective variogram estimates at $h = 800$ m indicates that the influence of the measurement errors is lower for N_t than for D_m and R . This can explain the fact that the slope of the variogram becomes negligible at shorter time steps for D_m and R (about 10 min) compared to N_t (about 30 min). These results show that the DSD fields are correlated up to 10 to 30 min, corresponding to typical temporal scales of rain cells. Berne et al. [2004] found similar temporal scales in the radar reflectivity (although for Mediterranean rainfall).

The observed decrease of the variability for increasing time steps results from the complex interactions between the decrease of the measurement error and the decrease of the natural variability of the DSD due to the smoothing effect from time integration. At temporal resolutions larger than 30 min, the sample variogram is basically flat and the fitted variogram model is a pure nugget model (slope \sim 0) which indicates that the natural variability of the DSD (if any) is below the noise level in the observations. In other words, the integration in time of the DSD measurements tends to remove the variability existing at high temporal resolution, and the remaining (limited) variability is solely due to measurement errors. The pure nugget variograms for large temporal resolutions also confirm the assumption of stationarity of the DSD at the pixel scale, as any trend in the DSD over the domain would result in non-flat variograms.

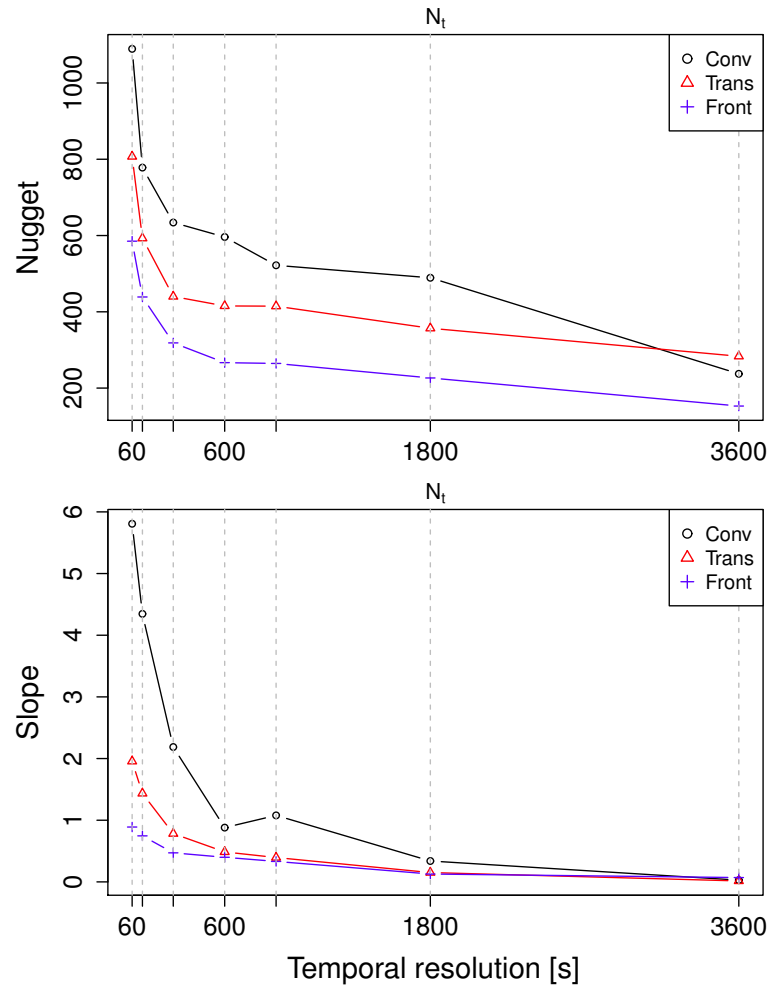


Figure 4.8: Influence of the temporal resolution on the nugget (top) and slope (bottom) parameters of the linear variogram model for the different types of rainfall.

4.5 Applications: the spatial representativity issues

Because of the strong spatial and temporal variability of rainfall, the issue of the representativity is crucial. For example in radar meteorology, the power law used to convert the measured reflectivity into rain rate is usually parameterized using point measurements from disdrometers, but applied at the radar sampling volume scale. Such scale discrepancies introduce uncertainty [Morin et al., 2003; Steiner and Smith, 2004].

In order to investigate the influence of the spatial structure of the DSD when upscaling from point (e.g., disdrometer) to areal measurement (e.g., weather radar pixel), a stochastic simulation approach is considered because there is no sill/range in the fitted variograms so classical quantification of the extension variance cannot be used [e.g., Journel and Huijbregts, 1978, p.54]. For each quantity of interest (N_t , D_m and R), 1000 fields are generated for each type of precipitation in the log space as the data are considered to be log-normal (see Section 4.3.2).

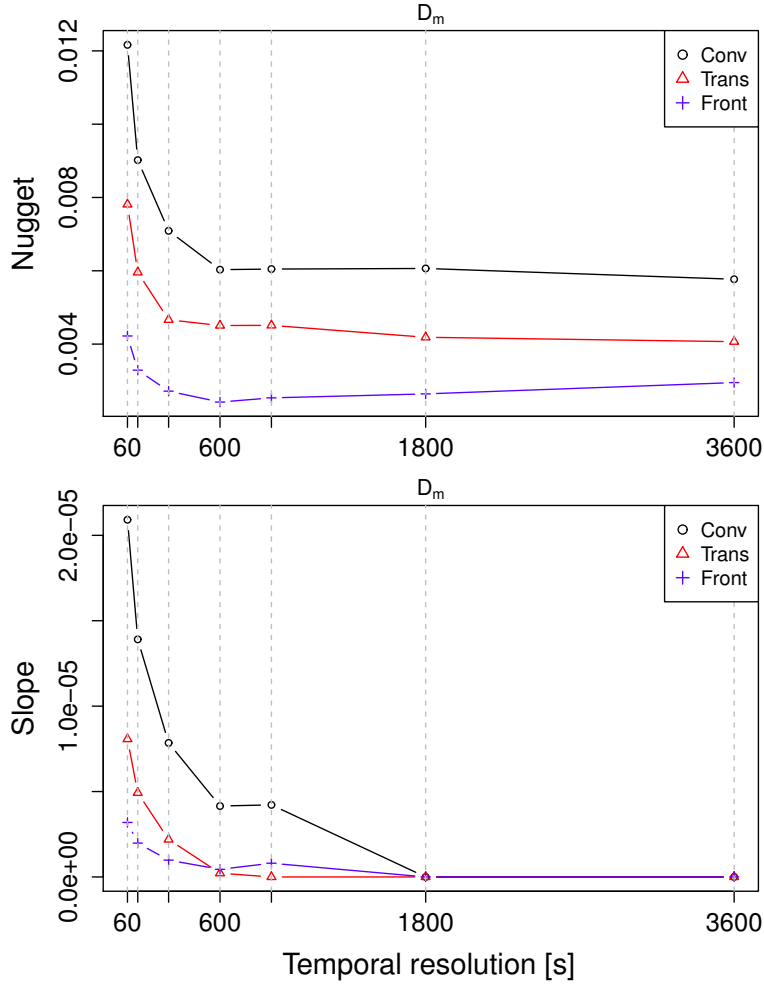


Figure 4.9: Same as Figure 4.8 for D_m .

The simulated 2D fields are constrained by the spatial structure quantified previously (i.e., variogram) and the average value of the quantity observed over the network (considering all measurements from all stations of the period of interest), both in log space. The simulated fields are then transformed into linear space. For each simulated field i , the relative error ε_i^r (r standing for *relative*) between the value simulated at the pixel in the center of the field (M_i^p) and the average value over the domain (M_i^a , a standing for *areal*) is quantified as:

$$\varepsilon_i^r(M) = \frac{M_i^p - M_i^a}{M_i^a} . \quad (4.11)$$

Since $\varepsilon_i^r(M)$ exhibits a Gaussian like distribution with zero mean, the dispersion of $\varepsilon_i^r(M)$ values can be accurately quantified by the standard deviation ($\sigma_{\varepsilon_i^r}$). A sensitivity test was performed to define the number of simulations required and 1000 was shown to be a good

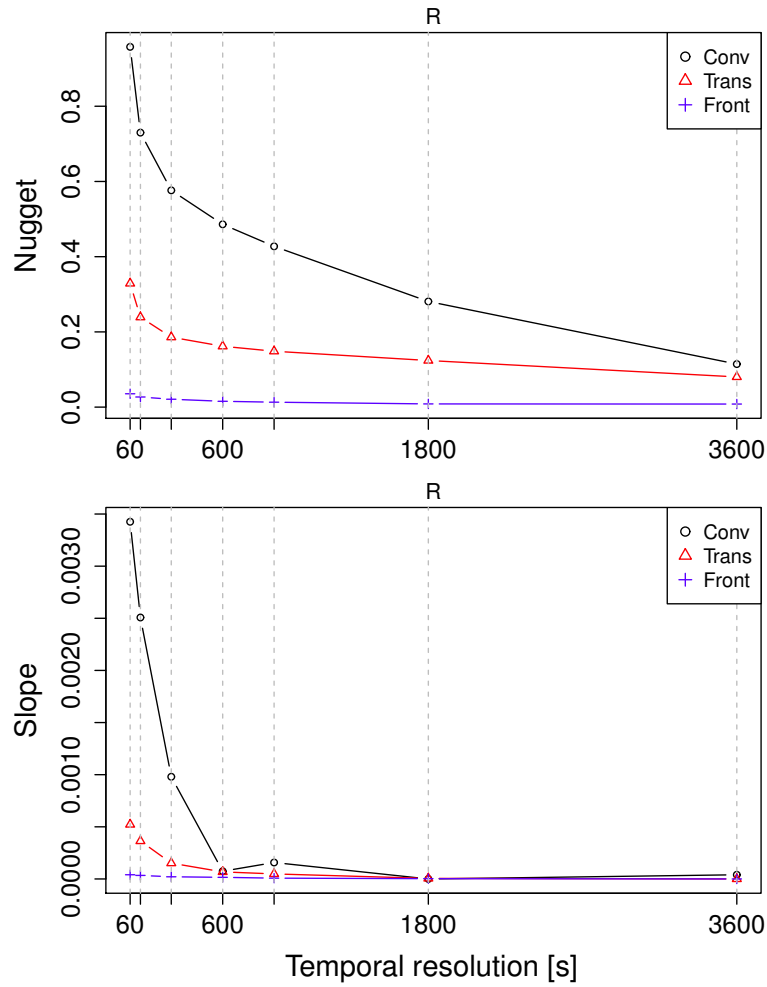


Figure 4.10: Same as Figure 4.8 for R .

trade off between robustness and computation time.

The analyses have been performed for different sizes of domain ranging from 100 m×100 m to 1000 m×1000 m. It should be noticed that two approaches have been considered to define the spatial resolution for each domain: (i) considering a constant number of pixels within the different domains (with the pixel size depending on the size of the domain) and (ii) considering a constant size of pixel (and hence a number of pixels per field varying as a function of the domain size). It appears that the two approaches provide similar results and hence only the results for a constant pixel size of 10 m are presented.

Figure 4.11 presents $\sigma_{\varepsilon_i^r}$ for N_t , D_m and R as a function of the size of the considered domain for the three types of rainfall at a 60-s temporal resolution. It shows that, independently of the quantity of interest and of the type of rainfall, the error associated when considering the value in the center of the field as representative of the domain is globally increasing with the domain size.

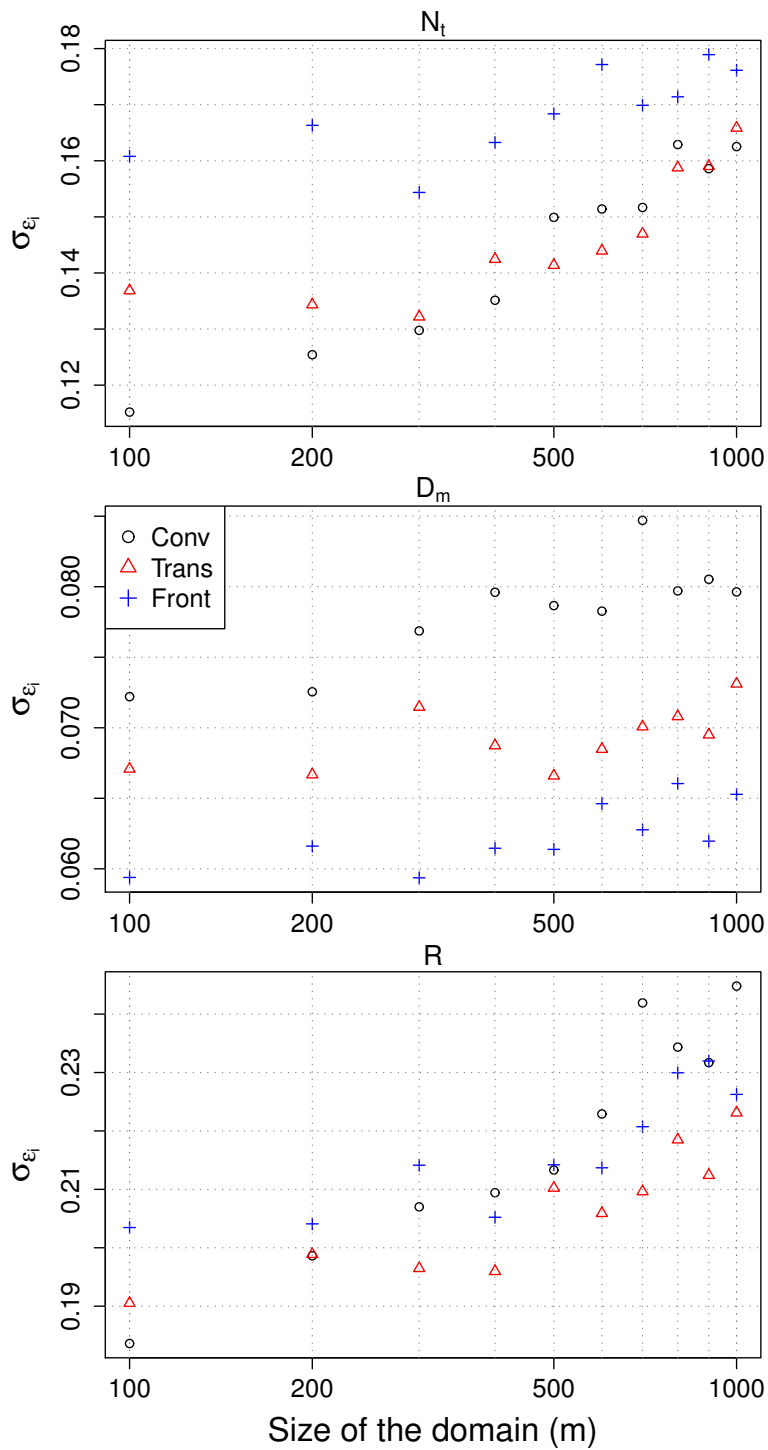


Figure 4.11: Standard deviation of σ_{ϵ_i} for N_t (top), D_m (middle) and R (bottom) as a function of domain size at a 60-s temporal resolution. X axes present the length of the side of the considered square domain.

The error associated with the upscaling of N_t ranges from 11.5% for convective rainfall for a domain of $100 \times 100 \text{ m}^2$ to about 18% for frontal rainfall and a domain of $1000 \times 1000 \text{ m}^2$. N_t exhibits higher values of $\sigma_{\varepsilon_i^r}$ for frontal than for convective and transitional rainfall. Since N_t exhibits a smaller variability for frontal than for convective rainfall, one would expect lower values of $\sigma_{\varepsilon_i^r}$ for frontal than convective rainfall. Because the frontal period is characterized by smaller values of N_t than for the two other types of rainfall (the median of N_t values for convective and transitional periods are respectively about 67% and 27% larger than the one for the frontal period), small differences between point and domain values will have stronger impact for frontal period. For instance, 32% of ε_i^r values are higher than 16.3% (17.6%) for convective (frontal) rainfall events (recall that 68% of a Gaussian distribution is within the interval $\pm 1\sigma$) for a domain of about $1000 \times 1000 \text{ m}^2$.

The standard deviation of $\varepsilon_i^r(D_m)$ is smaller than the one observed for N_t , with values below 8.5%. Globally, convective rainfall exhibits higher $\sigma_{\varepsilon_i^r}$ values than for transitional and frontal ones. The error is ranging from 7.2% (6.0%) to 8.5% (6.6%) for convective (frontal) rainfall with intermediate values for the transitional type.

Concerning R , the distinction of $\sigma_{\varepsilon_i^r}$ between the different types of rainfall as a function of domain size is much more complex. This can be due to the combination of the behaviors observed for N_t and D_m as R is a weighted moment of the DSD depending on both the total concentration of drops and their diameter. The error associated with the upscaling process ranges from about 18.4% (20.3%) to about 24.5% (23.2%) for convective (frontal) rainfall. For instance, for a domain size of about $500 \times 500 \text{ m}^2$ for which $\sigma_{\varepsilon_i^r}$ values between the different types of rainfall are similar, 32% of the differences between point and areal values are larger than 21%.

Furthermore, Figure 4.11 shows that the error associated with the extension of the domain for R corresponds to the combination of the error associated with N_t and D_m . However, further analyses do not show any significant relation between N_t and D_m .

The influence of the sampling resolution on $\sigma_{\varepsilon_i^r}$ is also investigated for 7 temporal resolutions ranging from 60 s to 1 h. As the variability tends to be reduced for increasing time steps (see Section 4.4.2), the error observed between point and areal values is decreasing. At 600-s temporal resolution and for a domain of $1000 \times 1000 \text{ m}^2$, $\sigma_{\varepsilon_i^r}$ is about 16.5% (15.5%) for convective (frontal) rainfall while it is about 24.5% (22.7%) at a 60-s temporal resolution. Similarly to the variograms, for time steps of 30 min and above, $\sigma_{\varepsilon_i^r}$ is no more dependent on the size of the domain, highlighting that $\sigma_{\varepsilon_i^r}$ is mainly dominated by measurement errors.

4.6 Conclusion

Information on the spatial organization of the DSD is of primary importance, especially for quantitative estimation of rainfall using remote sensing techniques. A network of 16 disdrometers has been deployed over $1 \times 1 \text{ km}^2$, which is the typical size of a weather radar

pixel, in Lausanne, Switzerland for about 16 months. Different types of rainfall have been collected and a total of 9, 19 and 8 rainfall events have been selected to illustrate convective, transitional and frontal rainfall types, respectively. Analyses have been performed for N_t , D_m and R . In a first step, the spatial correlation has been calculated and a parametric model has been fitted in order to compare our results with the literature. It globally shows that parameter values are of the same order as the ones presented in previous studies albeit the different studies are using different kinds of instrument in different climatologies. Variograms have been calculated for the different quantities of interest and linear models have been fitted. DSD can be considered as isotropic at the radar pixel scale. The results show that DSD fields are organized and not randomly distributed even at such a small scale (below 800 m). The observed variability is larger for the convective rainfall type than for the transitional and frontal ones. For decreasing temporal resolution, the variability is decreasing, as the integration in time tends to remove the variability existing at high temporal resolution. For time steps larger than 10 min for D_m and R and larger than 30 min for N_t , the variability of the DSD is below the noise level in the observations.

Such information about the spatial structure of the DSD can be used, for instance, to quantify the error associated with the extension of a point measurement as an areal value representing a spatial domain. Analyses have been conducted for different sizes of domain from 100 to 1000 m. It is shown that this error increases with the size of the domain: it is around 7% for D_m , 17% for N_t and around 23% for R , for a domain of $1000 \times 1000 \text{ m}^2$. For D_m , convective type rainfall exhibits larger errors than frontal rainfall, while the opposite is observed for N_t . Distinction between rainfall of different types is much more complex for the rain rate R . The temporal resolution is shown to have an influence on the error associated with the upscaling process. Similarly to the variograms, larger temporal resolutions exhibit smaller errors. For time steps of 30 min and larger, the observed error is mainly dominated by measurement errors and is no more depending on the size of the domain. The spatial structure of the DSD within a radar pixel has also an influence on the representativity of the parameters of the power laws used for radar rain-rate estimation, usually derived from point measurements and applied at the radar pixel. This question is currently investigated and will be addressed in a future publication.

The spatial structure of the DSD quantified in the present study has been obtained from measurements collected in Lausanne, Switzerland, and can be considered to give a relevant order of magnitude for temperate mid latitude climate. The same approach can be used to characterize the spatial structure of the DSD in different climatic regions. Moreover, the experimental setup limited the interdistance to about 1 km, so the spatial structure of the DSD and the error associated with using point measurements as areal estimates at larger scales (e.g., GPM pixel of $5 \times 5 \text{ km}^2$) needs to be investigated.

5 Influence of the variability of the DSD on radar rainfall estimators¹

5.1 Introduction

The rain rate is a quantity of primary importance for various hydrological processes. Rainfall information can be measured using ground-based instruments (e.g., rain gauges) or estimated using remote sensing. Remote sensing has the significant advantage of providing rainfall estimates over large areas with high resolution. However, such techniques do not directly measure rain rate but rather quantities related to the electromagnetic properties of falling hydrometeors such as the radar reflectivity factor Z (for conventional radar) and the specific differential phase shift K_{dp} (for polarimetric radar). It is commonly assumed that both quantities can be related to the rain rate through power laws:

$$Z = aR^b \quad (5.1)$$

$$R = cK_{dp}^d \quad (5.2)$$

where Z is expressed in $\text{mm}^6 \text{m}^{-3}$, R in mm h^{-1} and K_{dp} in $^{\circ} \text{km}^{-1}$. The coefficients a and b (c and d) are usually estimated from rain drop size distribution (DSD hereafter) measurements collected at a unique sampling location. The values $a=200$ and $b=1.6$ proposed by Marshall et al. [1955] about 60 years ago are still widely used. Numerous studies have shown the wide range of a and b values in different climatologies [e.g., Battan, 1973; Doelling et al., 1998; Chapon et al., 2008].

These parameters are influenced by the variability of the DSD [Uijlenhoet, 2001; Lee and Zawadzki, 2005], and consequently by the geographical location and the type of rainfall regime. They are also sensitive to: (1) the DSD sample size [Joss and Gori, 1978]; (2) the type of instrument for data collection [Campos and Zawadzki, 2000]; (3) the method for data analysis [Ciach and Krajewski, 1999; Chapon et al., 2008]; (4) erroneous measurements [Steiner et al., 1999] and measurement uncertainties affecting Z and R or R and K_{dp} [Ciach and Krajewski,

¹This chapter is partly based on a manuscript submitted to *Journal of Applied Meteorology and Climatology*

Chapter 5. Influence on radar rainfall estimators

1999; Campos and Zawadzki, 2000] and (5) the temporal and spatial integration [Morin et al., 2003; Steiner and Smith, 2004]. This last item raises the question of the adequacy of using (a, b) or (c, d) values derived from point measurements to calculate rain rates at the radar sampling volume scale (which is about 10^9 times larger). To the authors' knowledge, no studies have investigated this issue using spatially distributed DSD measurements at the radar pixel scale.

The objective of the present work is to quantify the influence of the spatial variability of the DSD at radar subgrid scale ($1 \times 1 \text{ km}^2$) on Z - R and R - K_{dp} relationships at the point and pixel scales using DSD measurements collected by a network of disdrometers. The sampling uncertainty associated with the disdrometers is taken into account in the analyses. The experimental setup and the data set are presented in Section 5.2 while the methods are detailed in Section 5.3. Section 5.4 presents the results for Z - R and R - K_{dp} relationships. Finally, a summary and conclusive remarks are provided in the last section.

5.2 Experimental set up and data set

A network of 16 optical disdrometers (PARSIVEL, OTT) deployed over an area of approximately $1 \text{ km} \times 1 \text{ km}$ in Lausanne, Switzerland, has collected DSD spectra for about 16 months (see Chapter 2 and Jaffrain et al. [2011]). The same selection of 36 rainfall events than the one presented in Section 4.2 is considered hereafter. Recall that a rainfall event is defined as a continuous rainy period of at least 15 min associated to an average rain amount of at least 1 mm, surrounded by continuous dry periods of at least 15 min. The dataset consists of 9, 19 and 8 rainfall events that have been identified as convective, transitional and frontal ones, corresponding to 571, 3493 and 838 rainy minutes respectively. Statistics of each group of rainfall events are provided in Table 5.1. It has to be noticed that the number of rainy minutes, and consequently the associated statistics, of each type of rainfall is slightly different from the ones presented in Chapter 4 (see Table 4.1). This is due to measurements that have not been considered in the following due to resonance effects especially at C-band (see Section 5.3.2 for details).

Table 5.1: Statistics of the three different groups of rainfall events at a 60-s temporal resolution.

	Convective	Transitional	Frontal
Number of events	9	19	8
Number of rainy minutes	571	3493	838
Rain amount averaged over the network [mm]	25.2	99.7	10.5
Mean of the averaged rain rate \overline{R} [mm h^{-1}]	2.63	1.71	0.75
$Q_{10\%}(\overline{R})$ [mm h^{-1}]	0.47	0.32	0.25
$Q_{50\%}(\overline{R})$ [mm h^{-1}]	2.07	1.16	0.64
$Q_{90\%}(\overline{R})$ [mm h^{-1}]	5.26	3.66	1.33

5.3 Methods

5.3.1 Pre-processing

Similarly to Jaffrain and Berne [2011], analyses are conducted on the different quantities of interest (Z , R and K_{dp}) derived from the DSD measurements. To filter out possible non-natural drops (e.g., from splashing, insects), all drops with a measured fall speed that deviates of more than 60% from the theoretical one given by Beard [1977] are disregarded. For consistency, only time steps for which all the 16 stations have recorded a rain rate R larger than 0.1 mm h^{-1} are considered in the analyses. Such filtering process have been shown to have negligible influence on total rain amounts [Jaffrain and Berne, 2011].

5.3.2 R , Z and K_{dp} calculation

The raindrop size distribution, denoted $N(D)$ and expressed in $\text{m}^{-3} \text{ mm}^{-1}$, is the concentration of drops according to their respective equivolume diameters. The rain rate is related to the DSD through:

$$R = 6\pi \cdot 10^{-4} \int_{D_{min}}^{D_{max}} N(D) v(D) D^3 dD \quad (5.3)$$

where $v(D)$ is the terminal fall speed [m s^{-1}] of a drop with a diameter D [mm]. The radar reflectivity factor at horizontal polarization Z_h [$\text{mm}^6 \text{ m}^{-3}$] and the specific differential phase shift K_{dp} [$^{\circ} \text{ km}^{-1}$] can be expressed as:

$$Z_h = \frac{10^6 \lambda^4}{\pi^5 \left| \frac{m^2 - 1}{m^2 + 2} \right|} \int_{D_{min}}^{D_{max}} \sigma_{B_h}(D) N(D) dD \quad (5.4)$$

$$K_{dp} = \frac{1800\lambda}{\pi} \int_{D_{min}}^{D_{max}} \Re(S_{h,h}(D) - S_{v,v}(D)) N(D) dD \quad (5.5)$$

where λ is the radar wavelength [cm], m is the complex refractive index of water [-], σ_{B_h} is the backscattering cross section at horizontal polarization [cm^2] and $\Re(S_{hh|vv}(D))$ is the real part of the forward scattering amplitudes at horizontal/vertical polarization [m]. All scattering coefficients have been computed using the T-matrix code by Mishchenko et al. [1996] and using the drop shape (axis ratio) from Andsager et al. [1999]. Z and K_{dp} estimates are computed at X-, C- and S-band radar frequencies. Interestingly, Z - R scatterplots exhibit complex patterns at C-band for all types of rainfall, with very high Z values associated with low to moderate R values. Figure 5.1 presents an example of the Z - R scatterplot associated with the transitional rainfall at C-band at a 60-s temporal resolution. The scatterplot shows two groups of shifted Z values that have been linked to the presence in the DSD of at least one

drop in the diameter class centered on 5.5 and 6.5 mm. Figure 5.1 clearly shows that shifted Z values are functions of the drop diameters, with the highest shifted Z values associated with the biggest recorded drops (class [6,7[mm). Similar patterns have been observed for the other stations. At S- and X-band, the influence of such drops is much more limited with slightly shifted Z values than can not be as easily distinguished from the other points of the scatterplot.

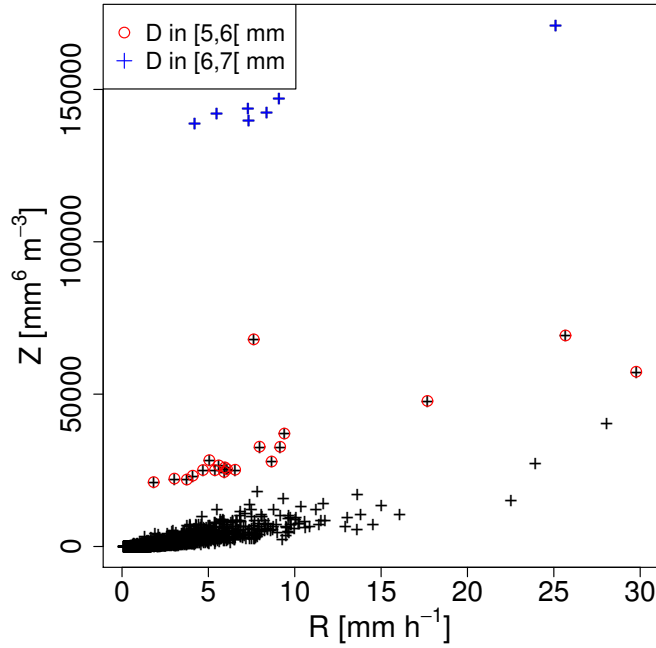


Figure 5.1: Z - R scatterplot from Station 10 for the transitional period at C-band at a 60-s temporal resolution. Blue crosses (red circles) denote time steps during which at least one drop in the diameter class centered on 6.5 (5.5) mm has been recorded.

These high Z values could be explained by resonance effects, which occur in the 5.5-7 mm range at C-band [Keenan et al., 2001; Thurai et al., 2007], and the associated measurements have been removed from the following analyses. Therefore, a total of 72, 172 and 1 measurements have been disregarded for the convective, transitional and frontal group respectively. The statistics presented in Table 5.1 are based on the filtered data.

5.3.3 Power-law fitting

In order to estimate the parameters a and b (c and d), a non-linear least-square regression is performed on Z - R (R - K_{dp}) scatterplots. Consequently, a set of (a,b) and (c,d) parameters have been computed for each sampling point (disdrometer) of the network for each type of rainfall. Considering all the point values as an ensemble (denoted with a subscript P in the following) helps reducing the sampling effect as regressions are performed on 16 times more points. On the other hand, the averaged values of R , Z and K_{dp} over the 16 stations

is supposed to be more representative of the radar values at the pixel scale (subscript A). However, it cannot be considered as representative of the full radar sampling volume because the disdrometers network does not sample the DSD over the full vertical extend.

Because the parameters are sensitive to the chosen independent variable [Ciach and Krajewski, 1999; Chapon et al., 2008], two regressions have been considered for the Z - R relationship. Eq 5.1 shows the more conventional one which considers Z as the dependent variable. As this relationship is devoted to the estimation of rain rates from the observed radar reflectivities, a more appropriate form is:

$$R = \left(\frac{1}{a}\right)^{\frac{1}{b}} Z^{\frac{1}{b}} \quad (5.6)$$

where R is the dependent variable. As an illustration, Figure 5.2 shows the Z_A - R_A scatterplot and the fitted Z_A - R_A and R_A - Z_A relationships for the transitional rainfall type at C-band and at a 60-s temporal resolution. The R_A - Z_A power law exhibits a different behaviour with lower a values and higher b values. Additional analyses have shown that the fitted R - Z power law is more sensitive to the density of point in the scatter (mainly concentrated at R values below 2.5 mm h^{-1}) while the fitted Z - R power law is more sensitive to the large values of Z .

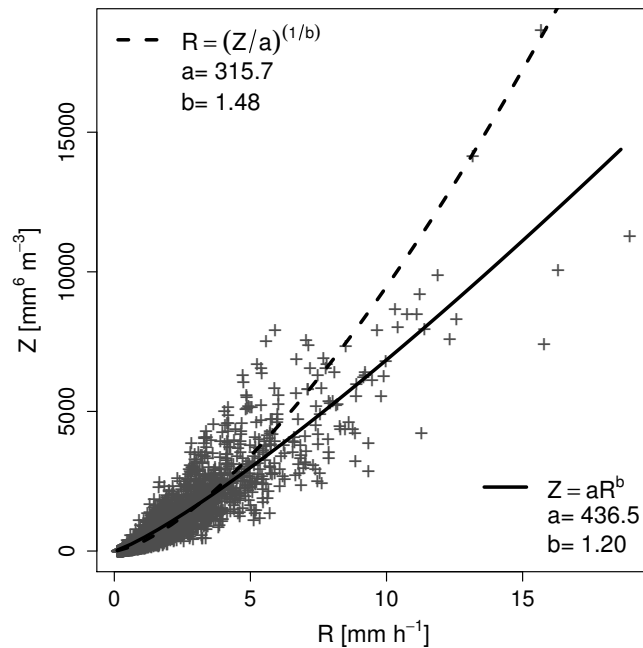


Figure 5.2: Z_A - R_A scatterplot and the fitted Z_A - R_A (solid line) and R_A - Z_A (dashed line) relationships for the transitional rainfall type at C-band and at a 60-s temporal resolution.

5.3.4 Sampling uncertainties

Because it can have significant impact on the estimation of the power-law parameters [Ciach and Krajewski, 1999; Campos and Zawadzki, 2000], the sampling uncertainty associated with R , Z and K_{dp} estimates from Parsivel measurements is taken into account. Jaffrain and Berne [2011] have quantified this sampling uncertainty which is considered as a white noise and hence characterized by its standard deviation σ .

As it can not be assumed uniform over the network, a stochastic simulation approach is considered. In the following, the quantity of interest observed by station i at time step t is denoted $m_{i,t}$. Similarly to Jaffrain et al. [2011] (see Section 2.6.2), for each station and each simulation, a set of $\hat{m}_{i,t}$ values is generated from a normal distribution centered on the observed $m_{i,t}$ with a variance equal to $\sigma_{i,t}^2$. To avoid generating non-physical values (e.g., negative \hat{R}), the distribution is truncated between $\min(m_i)$ and $\max(m_i)$. It provides a set of (a,b) and (c,d) values for each simulation. A sensitivity test has been performed and 500 simulations is a good trade-off between computation time and statistical significance. The uncertainty associated with a , b , c and d parameters due to the sampling process is quantified as the 80% confidence interval of these 500 values. It has to be noticed that the reflectivity values are first calculated in dBZ and then converted to $\text{mm}^6 \text{m}^{-3}$.

5.4 Results

5.4.1 Z-R relationships

As C-band is the most commonly used radar frequency in Europe, and because the Swiss operational network of radars is working at C-band, the focus will be hereafter on this frequency. Figure 5.3 presents the a and b values for the Z - R and R - Z power laws for each type of rainfall at C-band and for a temporal resolution of 60 s. It first shows that, independently of the considered power law, the different rainfall types can clearly be distinguished in terms of a and b values. Moreover, this figure clearly highlights that the observed variability of the parameters a and b of the Z - R relationship at point scale within a radar pixel can not be solely explained by the sampling uncertainty affecting Parsivel measurements. Concerning convective and transitional rain, they are much more distinct in the (a,b) space for the R - Z power law.

Overall, the uncertainty in a and b is smaller for the R - Z than the Z - R regression, and is larger for convective rain. For Z - R (R - Z) power laws fitted on individual station, the relative uncertainty in a is on average about 17%, 9% and 4% (8%, 4% and 3%) while it is about 7%, 5% and 6% (5%, 3% and 4%) for b for convective, transitional and frontal rain respectively. Moreover, independently of the type of rain and of the independent variable, the values of a and b from all point data together (the sample is 16 times larger than for a individual station) and from the pixel (due to the smoothing occurring when the resolution decreases) are affected by smaller uncertainties than values from individual stations.

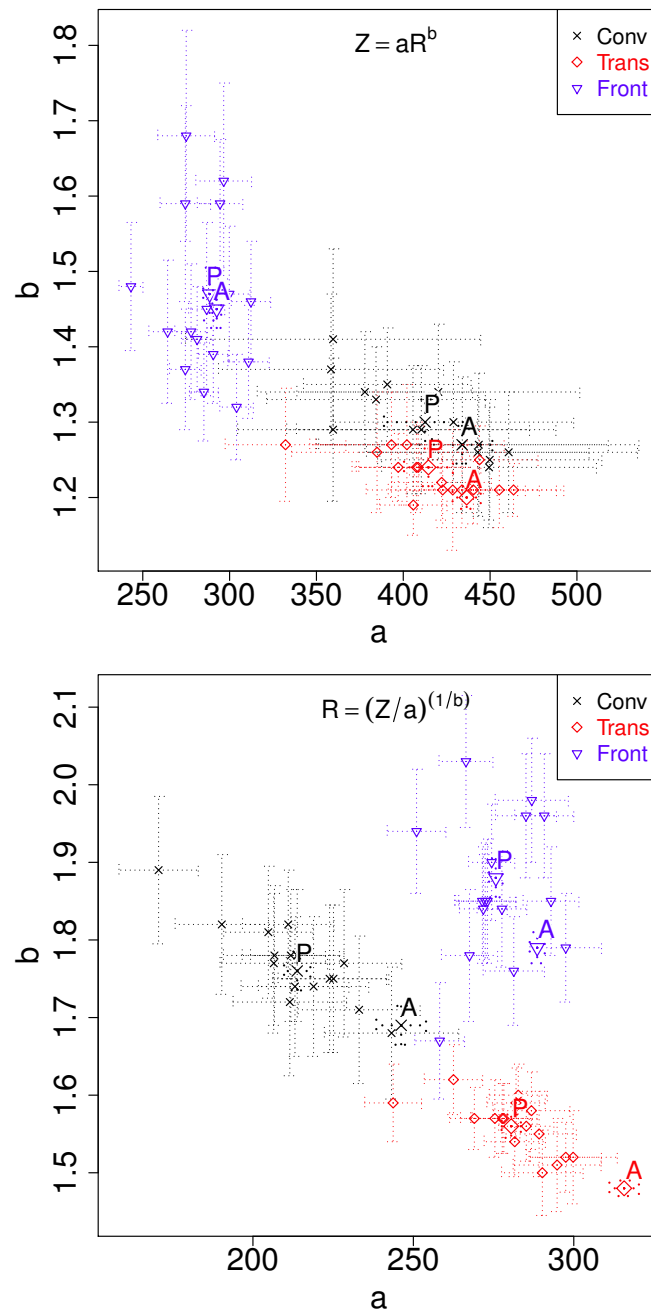


Figure 5.3: Fitted a and b parameters of the Z - R (top) and R - Z (bottom) relationships for the convective (circles), transitional (diamonds) and frontal (triangles) types of rainfall at C-band and at a 60-s temporal resolution. Dotted lines figure the associated uncertainty. The A (P) point denotes the a and b values at the pixel (aggregate of points) scale.

5.4.2 R- K_{dp} relationships

Similarly to Figure 5.3, the values of c and d at a temporal resolution of 60 s for each type of rain are presented at C-band in Figure 5.4. Overall, the observed c values are between 13

and 24 and the d values are between 0.63 and 0.80 at C-band. While d values are similar between the different radar frequencies, the observed c values are larger ($25 \leq c \leq 46$) at S-band and smaller ($10 \leq c \leq 17$) at X-band compared to C-band values. These values are consistent with previously published work (e.g., Tokay et al., 2005 at S-band, Anagnostou et al., 2009 at X-band).

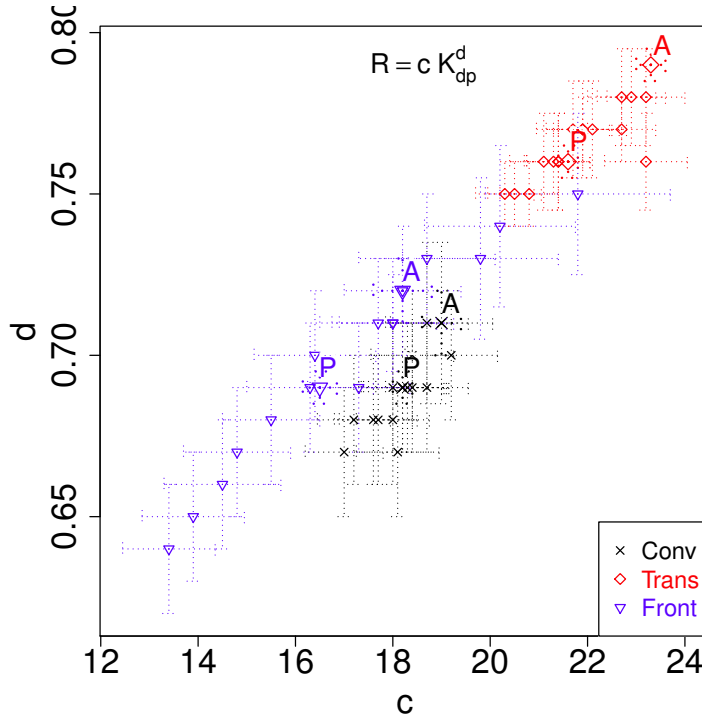


Figure 5.4: Same as Figure 5.3 for the c and d parameters of the $R-K_{dp}$ relationship at C-band.

Convective and transitional rain exhibit distinct c and d ranges of values while frontal rainfall shows a large variability in c and d values. The observed relative (to the areal c_A and d_A values) variability in c and d values for frontal rain is about $[-27\%;+20\%]$ and $[-11\%;+5\%]$ respectively while it is in the order of $[-12\%;+1\%]$ and $[-6\%;-1\%]$ for c and d values for convective and transitional rain. As for the $Z-R$ and $R-Z$ relationships, the uncertainty affecting c and d values is smaller for areal values than individual station estimates. The two parameters of the $R-K_{dp}$ relationship appears to be dependent with increasing c values associated with increasing d values.

Similar behaviours are observed at S-band with similar range of d values while c values are higher ($24 < c < 45$) than for C-band ($13 < c < 24$). At X-band, although the general behaviour is similar to the one at C-band, frontal and convective rainfall are much more distinct. Figure 5.5 presents the ranges of c and d estimates for the $R-K_{dp}$ relationships at X-band.

Interestingly, d values seem "stable" between the different weather radar frequency, i.e., ranging from about 0.65 to 0.85 independently of the type of precipitation. On the other hand,

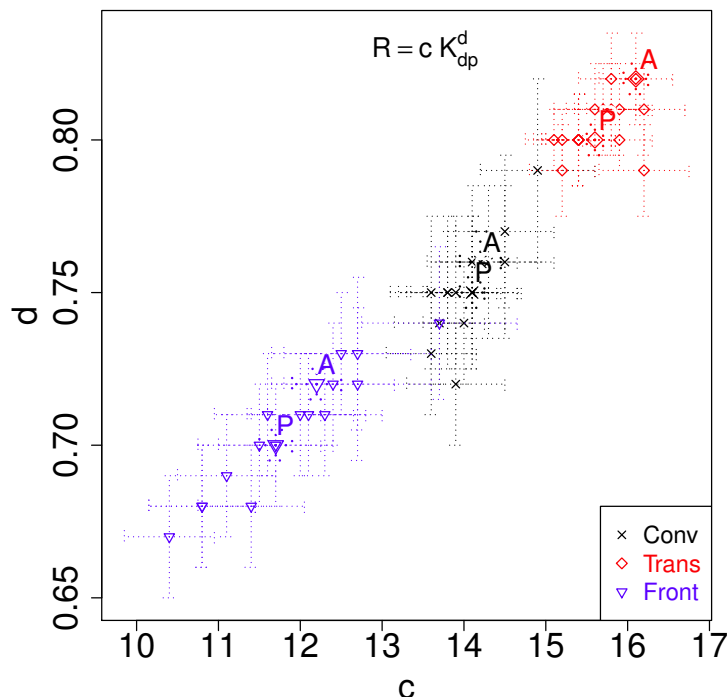


Figure 5.5: Same as Figure 5.4 at X-band.

the prefactor (c) values are increasing for decreasing frequencies indicating that, similarly to the $a_h = \alpha K_{dp}^\beta$ relationship, where a_h is the specific attenuation at horizontal polarization [dB km^{-1}], only the prefactor is significantly influenced by the wavelength [Thurai and Bringi, 2008].

5.4.3 Impacts on rain amount estimation

The observed variability of the parameters of the Z - R and R - K_{dp} relationships within the monitored area ($\sim 1 \text{ km}^2$) can have a significant influence on the estimated rain rate, which is the quantity of interest for many environmental studies. To illustrate this issue, the averaged reflectivity Z_A and the averaged specific differential phase shift $K_{dp,A}$ are considered as representative of the quantities directly measured by a radar. The rain rates are estimated at each station and at the radar pixel scale using the different power laws to convert Z or K_{dp} in R . Finally, the cumulative rain amounts are calculated for each type of rain based on the estimated rain rates. Figure 5.6 presents the rain amounts estimated from the Z - R , R - Z and R - K_{dp} power laws at C-band and for each type of rain. To ease the comparison between the different types of rain, total amounts are expressed as the ratio to the pixel (A) rain amount.

Figure 5.6 shows that the observed variability of the power-law parameters at the point scale can lead to a deviation between -5 and +15% compared to the areal rain amount. The Z - R power law exhibits the highest variability in rain amount estimates independently of the type

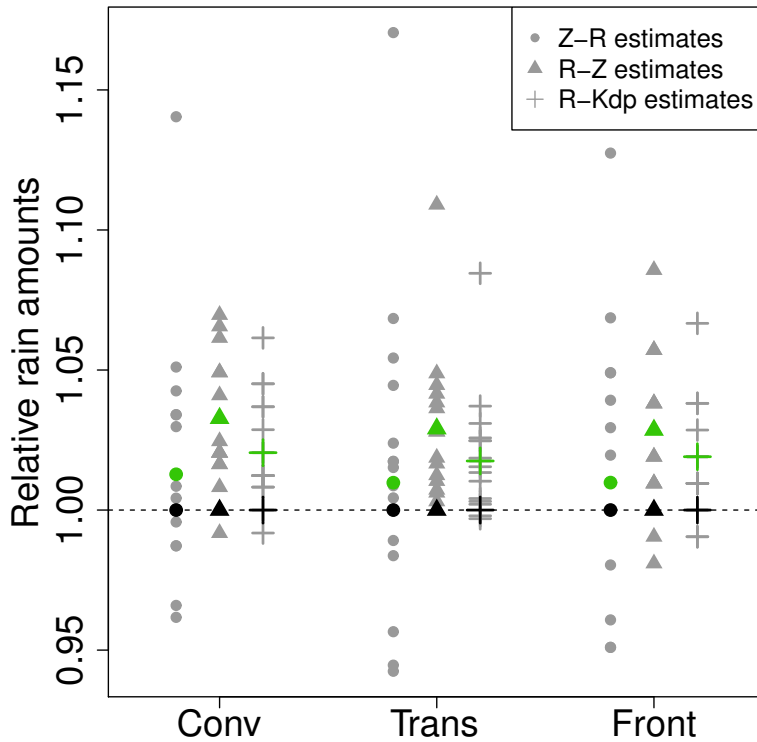


Figure 5.6: Rainfall amounts estimated from Z - R (circles), R - Z (triangles) and R - K_{dp} (crosses) power laws for each type of rain at C-band frequency. For comparison purposes, rain amounts are normalized by the respective areal rain amount. Black (green) symbols denote the rain amounts associated with the average $A(P)$ relationships.

of rain. For R - Z and R - K_{dp} power laws, most point-scale parameter sets (a , b or c , d) tend to overestimate the rain amount compared to the pixel value.

5.4.4 Influence of the temporal resolution

Previous sections have highlighted the significant influence of the spatial variability of the DSD on radar rainfall estimators at a 60-s temporal resolution. As it has been shown in Section 4.4.2 that there is a significant spatial variability of the DSD at 1 km^2 scale at temporal resolution below 30 min the analyses have been performed as well for 5 additional temporal resolutions, namely 2, 5, 10, 15 and 30 min.

Independently of the relationship considered, a significant variability of the a , b , c and d parameters is observed for time steps below 30 min. As the time step increases, the distinction between the estimated parameters for the different types of rainfall is more difficult. For R - K_{dp} relationship, a similar behaviour is observed with closer c and d parameters for all types for rainfall for increasing time steps. At a temporal resolution of 30 min and above, the sampling uncertainty of Parsivel that is propagating into the estimation of the parameters of

the relationships is of the same order of magnitude as the natural variability of the parameters. As an illustration, Figure 5.7 presents the fitted a and b parameters for the R - Z relationship at a temporal resolution of 30 min.

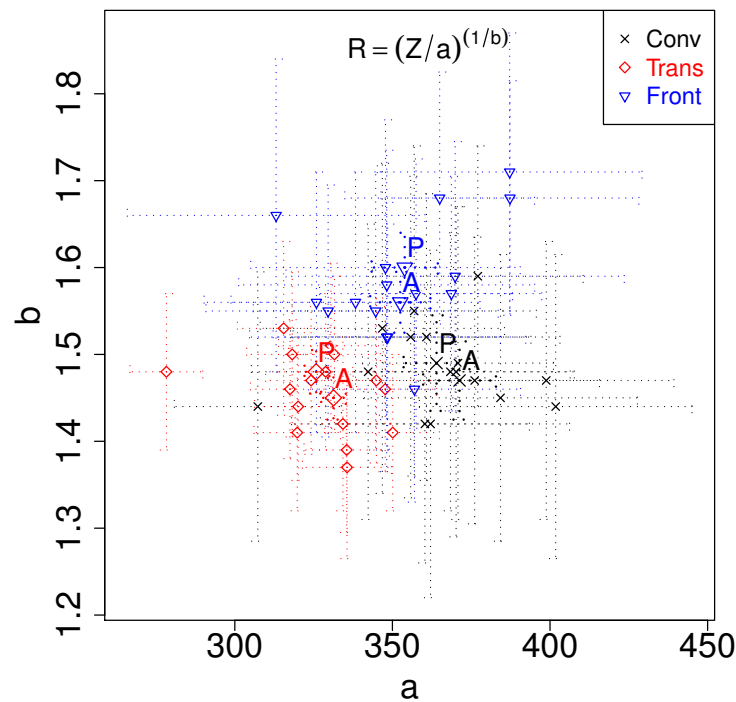


Figure 5.7: Same as Figure 5.3 for R - Z relationship at C-band and a temporal resolution of 30 min.

Interestingly, further investigations have shown that the variability of the power law parameters is not decreasing for larger time steps. While the variability of the DSD is decreasing for increasing time steps (see Section 4.4.2), the variability of a and b estimates seems to be globally independent of the temporal resolution (not shown). However, the sampling uncertainty propagated into the parameter estimates tends to increase for larger time steps. The average (over the 16 stations) relative error (expressed in %) on each parameter derived at point scale is calculated and presented in Figure 5.8 as a function of the temporal resolution. For example, the error on c (d) due to the sampling uncertainty is ranging from about 5% (3%) at 1 min to about 20% (8%) at a temporal resolution of 30 min.

In terms of rain amounts deviation, the time resolution does not appear to have a significant influence, providing similar results for all temporal resolutions.

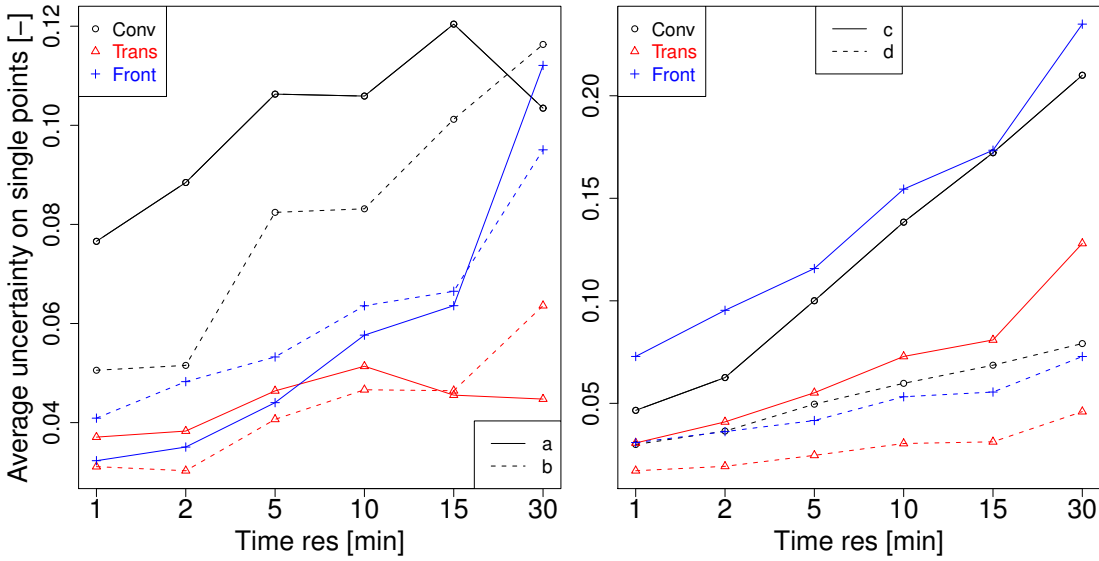


Figure 5.8: Influence of the temporal resolution on the average relative uncertainty of the power law parameters derived at the single point (instrument) scale for R - Z (left) and R - K_{dp} (right) relationships for each type of rainfall. Solid (dashed) line represents the average relative uncertainty on a and c (b and d).

5.5 Summary and conclusion

The significant spatial variability of the DSD has been highlighted in Chapter 4 using DSD measurements collected by a network of 16 disdrometers deployed over a $1 \times 1 \text{ km}^2$ area in Lausanne, Switzerland. This chapter aims at quantifying the propagation of the DSD spatial structure into a variability of the power-law parameters used to estimate rain rates from radar data. Similarly to Chapter 4, the considered data set consists of 36 rainfall events that have been identified and grouped according to their respective type of rainfall (i.e., convective, transitional and frontal).

From DSD measurements, integral quantities of the DSD such as the rain rate R , the radar reflectivity factor Z and the specific differential phase K_{dp} have been calculated. A non-linear least square fitting on the $Z = f(R)$, $R = f(Z)$ and $R = f(K_{dp})$ scatterplots have provided estimates of the different parameters of the Z - R , R - Z and R - K_{dp} relationships, respectively. These parameters have been derived at different spatial scales: (i) for each of the 16 disdrometers, (ii) considering an aggregate of all the 16 point values and (iii) considering the averaged value at each time step over the 16 instruments, which should provide estimates more representative of the covered spatial area. The sampling uncertainty associated with DSD measurements is taken into account and propagated into the power-law parameters through stochastic simulations.

First, it points out the influence of the observed variability of the DSD within a typical weather radar pixel on the parameters of the power laws for R estimation, independently of the type of rain (convective, transitional and frontal). Indeed, the variability of the parameters of the

power laws within the radar pixel can be larger than the sampling uncertainty associated with disdrometer measurements showing that this variability cannot be solely explain by the sampling uncertainty inherent to the instrument. Distinct patterns of a and b (or c and d) values are observed between the different types of rainfall. Moreover, the dependent variable considered (i.e., Z or R) in the Z - R relationship has a strong influence on the parameter estimates and their respective variability.

This variability has been propagated into the radar rain amount estimates from radar power laws. Considering the reflectivity averaged over the 16 disdrometers at each time step as representative of the reflectivity that should be seen by the radar, rain rate are estimated using the power laws parametrized previously (at each station, for the aggregate and for the pixel area). The derived rain amount varies between -5% to +15% of the pixel rain amount. Depending on the application, care must be taken when using power-law parameters derived from point-scale measurements and applied at radar pixel scale.

Finally, the influence of the temporal resolution on the variability of the power law parameters has been investigated in this chapter. The observed variability appears to be significant, i.e., larger than the error associated with the sampling process, for time steps below 30 min. For time steps of 30 min and above, the natural variability of the power law parameters cannot be clearly distinguished from the one induced by the sampling process. Further analyses have pointed that the observed variability is not influenced by the temporal resolution. In addition, the error associated with the estimates, i.e., the variability induced by the sampling uncertainty, is increasing for larger time steps.

6 Perspectives and additional field campaigns

6.1 Introduction

Part of this PhD was devoted to the design and the construction of a network of autonomous disdrometers in collaboration with A. Studzinski. The network has been deployed over a $1 \times 1 \text{ km}^2$ area in Lausanne, Switzerland, for about 16 months from March 2009 to July 2010¹. Based on this data set, it has been shown in Chapters 4 and 5 that the spatial variability of the DSD and its consequences on radar rainfall estimations are significant even at a 1 km^2 scale. Additional field campaigns have been conducted in order to extend the analyses presented in this PhD to larger spatial scales as well as other climatologies. This chapter is presenting some perspectives and issues that might be addressed thanks to this set up of autonomous disdrometers. It has to be noticed that this chapter is illustrating the added value of the network of disdrometers presented in Chapter 2 rather than presenting scientific results.

6.2 Variability of the DSD for Mediterranean region

The Mediterranean region is characterized by complex interactions between the Mediterranean sea, the urbanized coastal areas and the orography. These interactions are still poorly understood especially in the context of natural hazards (extreme rainfall, flash floods, hail events, landslides, ...). In this context, an international project called HYMEX (HYdrological cycle in Mediterranean EXperiment) launched by the french scientific community (more details at <http://www.hymex.org/>) has been set up to address this issue. HYMEX is an international project which includes couples of short-term (i.e., few months) multi-instruments (aircrafts, ground-based C-band radars, mobile X-band radars, disdrometers, ...) field campaigns. The main goal of this huge project is to provide better knowledges of the Mediterranean area in terms of the water budget, the continental hydrological cycle, the natural hazards and the associated societal and economic impacts.

¹This 16-months data set (DSD measurements at 30-s temporal resolution from 16 disdrometers) is easily available for the scientific community. For further information, please visit the Laboratoire de Télédétection Environnemental, EPFL-LTE, Lausanne, Switzerland (<http://lte.epfl.ch>).

Chapter 6. Perspectives and additional field campaigns

Climatological analyses of rainfall data collected by the MétéoFrance operational network of rain gauges on the period 1958-2000 have pointed out significant differences in rain amounts collected by a few rain gauges in the Mediterranean area [G. Molinié, personal communication]. The orography is known to play a major role in Mediterranean precipitation. In this context, a field campaign, called HPicoNet (<http://www.ohmcv.fr/hpiconet/index.html>), has been organized in Ardèche, France, in the neighbouring area of the operational rain gauge reporting the largest yearly and daily rain amounts. The objectives of this campaign are twofold. As a preliminary field campaign to HYMEX, the first goal was to test the technical feasibility for the deployment of a multi-sensors network for monitoring rainfall at a high time resolution. In addition, this campaign should provide the data set required for a better understanding of the local climatology in terms of rainfall.

Figure 6.1 presents the regional situation and the neighbouring orography of the HPicoNet network. Each sampling location has been equipped with a 1000 cm² tipping-bucket rain

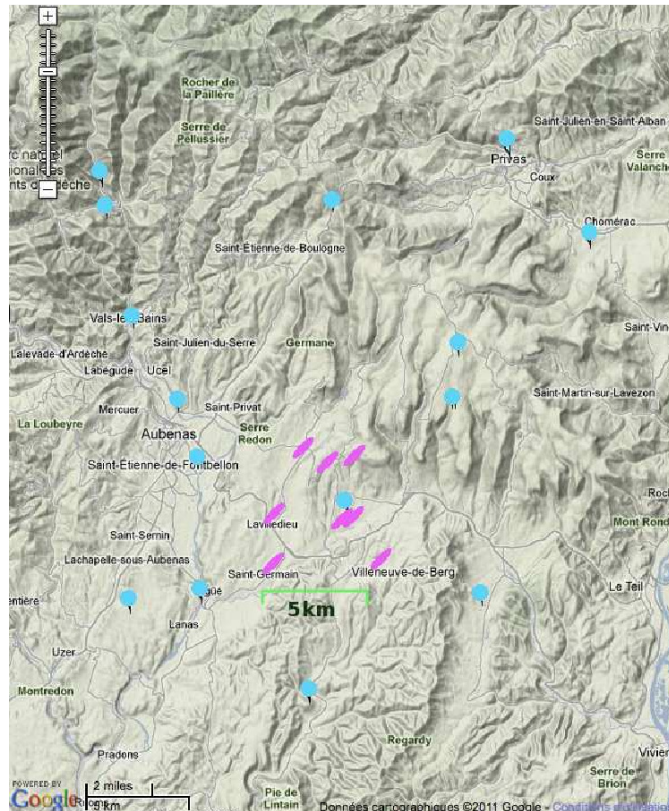


Figure 6.1: Regional situation of the HPicoNet network in Ardèche, France. Blue circles denote the operational rain gauge network while the pink bars present the HPicoNet network. (courtesy of Gilles Molinié, LTHE, Grenoble).

gauge and an optical disdrometer Parsivel. Moreover, at two sampling locations, an induction ring has been deployed providing additional measurements of the electrical charge of raindrops. Figure 6.2 shows a typical setup including the induction ring. Because the distance



Figure 6.2: Example of experimental setup during the HPicoNet campaign on the roof of a school in Lavilledieu, Ardèche, France. The setup consists of a 1000 cm² tipping-bucket rain gauge (left), an optical disdrometer Parsivel (back-right) and an induction ring (front-right).

between a slave and the associated master station can be up to 6 km, the disdrometer stations as presented in Chapter 2, using omni-directional antennas, had to be upgraded for this setup. The use of directional antennas greatly helps improving radio transmission between master and slave stations for slave-master distances larger than 1 km.

The HPicoNet campaign has been initiated by the Laboratoire d'étude des Transferts en Hydrologie et Environnement (LTHE, Grenoble, France) and is a collaboration between LTHE, EPFL-LTE (Lausanne, Switzerland) and the Laboratoire d'Aérodologie (Toulouse, France). The instruments have been deployed in October 2010. For administrative reasons with the custom office, EPFL-LTE disdrometers have been removed in June 2011.

Some preliminary results have been recently presented at the Plinius 2011 conference (*'High-resolution rainfall sampling: the scales of interest'* by G. Molinié et al). A more in depth analysis of this data set is still in progress.

Acknowledgements:

The author acknowledges the various LTHE collaborators for their helps in the deployment and maintenance of the network of disdrometers. The help of André Studzinski (EPFL-LTE), Alexis Berne (EPFL-LTE), Marc Schleiss (EPFL-LTE) and Florian Humair (EPFL-LTE) is greatly acknowledged.

6.3 Variability of the DSD as a function of the altitude

The observed variability of raindrops characteristics (size, shape, terminal fall velocity, ...) is related to the various microphysical processes involve in the formation of precipitation (see Section 1.2). In more complex terrain (i.e., mountainous area), the dynamic of air masses is strongly disturbed by the local topography which increases the complexity of orographic precipitation formation [Roe, 2005]. In addition, rainfall estimation in mountainous area is a challenging task due to strong echoes from ground and shielding of the radar beam by the relief [e.g., Germann et al., 2006] and the presence of solid precipitation (snowflakes, aggregates, ...).

A better knowledge of the DSD variability in mountainous area is crucial to better understand orographic precipitation and reduce the impact of natural hazards. In this framework, a join project between EPFL-LTE and the Swiss Institute for Snow and Avalanche Research (WSL-SLF, Davos) has been launched in 2009. 3 optical disdrometers have been deployed along a slope in Davos, Switzerland in February 2009. The disdrometers' altitudes are 1520, 2276 and 2543 m respectively. Figure 6.3 shows the 3 disdrometers that have been deployed in the Davos area. The disdrometers were collecting DSD measurements at a 30-s time resolution. In terms of technical issues, because the instruments required to be heated for

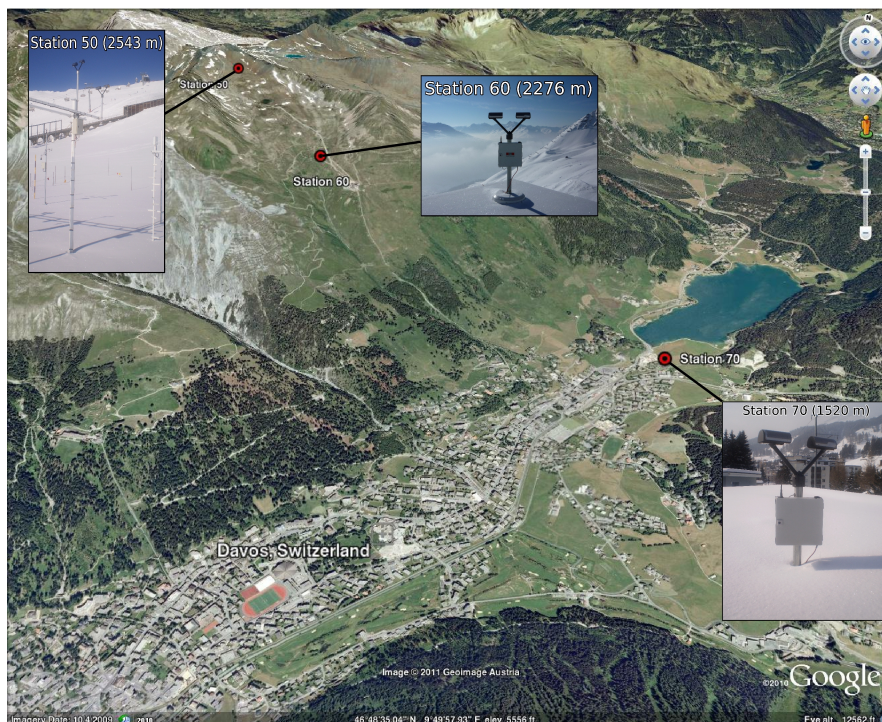


Figure 6.3: The experimental setup deployed in Davos, Switzerland in order to investigate the influence of the altitude on the variability of the drop size distribution.

measurements at high altitude, the disdrometers have been modified for a 24-V functioning. The disdrometer deployed at the top was neighbouring the WSL-SLF experimental site at the

6.4. The use of commercial microwave links for rainfall monitoring in urban area

Weissfluhjoch, providing additional measurements of liquid and solid precipitation. Moreover, to complement the transect of disdrometers, a 2D-Video Disdrometer (2DVD) [Kruger and Krajewski, 2002] has been deployed in September 2009 at the Weissfluhjoch experimental site as illustrated by Figure 6.4. Finally, a mobile X-band weather radar has been installed,

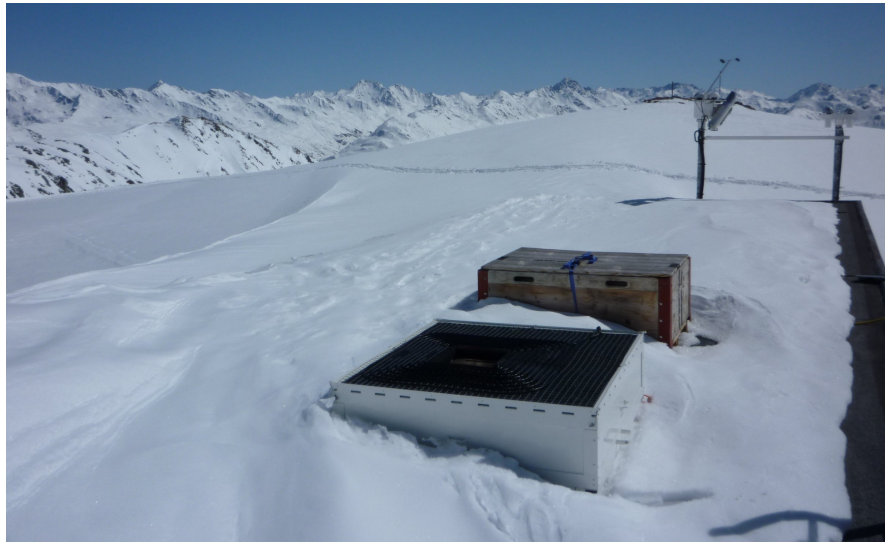


Figure 6.4: The 2D-Video Disdrometer deployed at the Weissfluhjoch experimental site (WSL-SLF) at 2543 m height in Davos, Switzerland.

in September 2009, on the opposite site of the valley in order to scan the Weissfluhjoch experimental site.

This experiment was conducted until July 2011. The transect of disdrometers has been collecting data for about 2.5 years while the 2DVD and X-band radar have been operational for a bit less than 2 years. This campaign has provided a rich and promising data set for the quantification of the variability of the DSD according to the altitude and various investigations on liquid and solid precipitation. Analyses of this data set are currently conducted.

Acknowledgements:

The help of Nick Dawes (SLF, Davos), Florian Pantillon (EPFL-LTE) and Yann Chavaillaz (EPFL-LTE) in the deployment and maintenance of the disdrometers and the 2DVD is herein greatly acknowledged.

6.4 The use of commercial microwave links for rainfall monitoring in urban area

The increase of the anthropogenic activity is associated with the development of urbanized areas, characterized by non-permeable surfaces (buildings, roads, . . .), which considerably

Chapter 6. Perspectives and additional field campaigns

affect the hydrological dynamics of a watershed. Reliable estimation of rainfall in urban areas is crucial for the design and the operation of urban drainage infrastructures (e.g., sewers, rainwater retention tanks) in order to prevent urban floods. Nevertheless, urban water management requires rainfall data at a higher spatial (below 1 km) and temporal (about 1-5 min) resolution than the ones provided by operational weather services [Berne et al., 2004].

The possibility to estimate rainfall from microwave links used in telecommunication has been recently reported [Messer et al., 2006; Leijnse et al., 2007]. The high spatial density of microwave links, especially in urban area, makes it a powerful and promising tool for rainfall monitoring. Due to the range of frequencies considered in telecommunication to transmit the data, the signal is attenuated if rainfall occurs along the path transmitter-receiver. This information can be related to the path-averaged rain rate as soon as the attenuation occurring during dry periods (called *attenuation baseline*) is taken into account. Various approaches have been proposed in the literature to take into account the attenuation baseline [e.g., Rahimi et al., 2003; Upton et al., 2005; Schleiss and Berne, 2010]. Additional analyses have been reported, mainly using links that have been specifically designed for rainfall estimation which makes difficult to integrate these results into an operational telecommunication network.

However, the reported studies have focused the analyses on rain rate retrieval, which is an integral quantity related to the DSD, rather than on the DSD itself. As many challenges remain regarding the processing of microwave link data for DSD retrieval in urban area, a project called COMMON (COmmercial Microwave links for urban rainfall MONitoring) has been initiated. This project is based on a collaboration between the Urban Water Management group of the Center for Aquatic Research (EAWAG-UWM, Dübendorf) and the Environmental Remote Sensing Laboratory (EPFL-LTE, Lausanne). In this framework, a commercial telecommunication microwave link has been deployed over a 1.85 km urbanized straight line as illustrated in Figure 6.5. For ground validation, a set of 5 autonomous disdrometers [Jaffrain et al., 2011] has been deployed at 4 sampling locations along the path of the microwave link. The dual disdrometers set up will help to characterize the sampling uncertainty of the disdrometers [Jaffrain and Berne, 2011] in the analyses. The 4 sampling locations have been chosen as a trade-off between a regular distribution of the instruments, the distance to the microwave-link path, line of sight for data transmission between the different instruments and minimum probability of disturbance. In order to have independent rain rate measurements, 3 of the sampling locations have been in addition completed by a tipping-bucket rain gauge (Précis Mécanique, model 3029) deployed in the nearby vicinity of the disdrometers. This campaign has started on March 2011 and is still collecting data.

Acknowledgements:

The help of André Studzinski (EPFL-LTE), Marc Schleiss (EPFL-LTE), Jörg Rieckermann (EAWAG-UWM) and Zhe Wang (EAWAG-UWM) for the deployment and the constant maintenance of the instruments is acknowledged.

6.4. The use of commercial microwave links for rainfall monitoring in urban area



Figure 6.5: The COMMON field campaign involves a microwave link deployed over a 1.85 km distance, 5 autonomous disdrometers deployed at 4 sampling locations and 3 tipping bucket rain gauges (courtesy of Marc Schleiss, EPFL-LTE).

7 Summary and Conclusions

The quantification of the various impacts of the global warming on the hydrological cycle is a question of primary interest. While the amplitude of future changes is still difficult to estimate, numerous climatic models have pointed out a general increase of the Earth temperature. As it will affect all the Earth system, significant changes in precipitation amounts, intensities, durations and frequencies are expected. A fundamental tool for precipitation estimation is the radar which can be ground based or on-board of a space platform. The main issue in radar techniques is the conversion of the observable parameter (Z for conventional radar, Z_{dr} and K_{dp} for polarimetric ones) into the variable of interest (the rain rate R) for hydrological applications. Various relationships have been presented in the literature for the last 50 years highlighting the strong influence of the DSD variability (in time and space) on the relationships used for conversion in radar processing. In this context, a better understanding of the spatial structure of the DSD is of primary importance to improve radar rainfall estimations.

In order to address this issue using an experimental approach, a network of 16 disdrometers (Parsivel) has been developed and built at EPFL-LTE. The network has been presented in details in Chapter 2. To ease instrument deployment, they have been designed for an autonomous functioning in term of power supply and data transmission. To reduce the cost of the project, the network has been divided into four groups, each group of 4 disdrometers being equipped with only one data logger. The data transmission within each group is based on radio communication (between master and slave stations) and GPRS, a commonly used data service for telecommunication, to transmit the data in real time to a remote web server. The network has been deployed over a typical weather radar pixel ($\sim 1 \times 1 \text{ km}^2$) in order to investigate the small scale variability of the DSD. The deployment lasted for about 16 months and DSD measurements at 30-s temporal resolution for different types of rainfall have been collected. This set up has provided a key data set to investigate the spatial variability of the DSD at radar subgrid scales.

Any measurement of a physical process can be seen as the combination of two signals: the natural signal, of interest but not known, and an artefact signal induced by the sampling process of this natural phenomena. As it has been emphasized in the literature, this artefact

Chapter 7. Summary and Conclusions

signal can be of the same order as the natural one. A quantification of the sampling uncertainty associated with our instrument (Parsivel) is hence crucial for reliable analyses. Consequently, Chapter 3 presents a 15-month experiment that has been conducted involving collocated measurements from 2 disdrometers and 2 tipping-bucket rain gauges (for independent measurement of rain rate). The sampling uncertainty associated with Parsivel measurements has been quantified as a function of the magnitude of the quantity of interest and the temporal resolution considered. Two quantities describing the DSD have been considered, namely the total concentration of drops N_t and the median-volume diameter D_0 . Moreover, the analyses have been conducted as well on integral quantities of the DSD, such as the rain rate R , the radar reflectivity factor Z and the differential reflectivity Z_{dr} . Globally, independently of the time resolution and of the magnitude of the considered quantity, the sampling uncertainty is below 25% for N_t , D_0 and R and is decreasing for increasing time steps. The sampling uncertainty associated with N_t and R estimates is decreasing for increasing magnitude of the quantity of interest. For D_0 , a different pattern is observed, with larger uncertainty values for large D_0 estimates.

Based on the data set presented in Chapter 2, a selection of 36 rainfall events has been considered and classified according to three types of rain from visual inspection of radar rainfall maps. It consists of 9 convective, 19 transitional and 8 frontal rainfall events corresponding to about 643, 3665 and 839 rainy minutes respectively. As the three groups of rainfall are considered as representative of each type of rainfall, each group of events is considered as an homogeneous ensemble to illustrate the average spatial structure associated with each type of rainfall.

A geostatistical approach has been used in Chapter 4 to quantify the spatial structure of the different quantities of interest. The analyses have been focused on N_t , D_m and R . Because classical tools to characterize the spatial structure are well suited for Gaussian-like distributions, which is not a fulfilled condition as the quantities of interest exhibit positively skewed distributions, a logarithm transform has been considered. A sample variogram based on quantiles, similar to the classical Matheron sample variogram, has been calculated on the log transforms for each quantity of interest and each type of rainfall. The estimated semi-variance ($\hat{\gamma}(h)$) values are then back-transformed into linear space. Independently of the quantity considered, the average sample variograms clearly show that DSD fields are organized and not randomly distributed within a typical radar pixel. The observed variability is larger than the *nugget* of the variogram, which can be seen as an estimation of the measurement errors in the analyses. Linear variogram models are well suited to represent the different sample variograms for distance lags up to 800 m (which is the maximum interdistance of the network). The influence of the temporal resolution on the spatial structure of the DSD is also addressed in Chapter 4. It is shown that there is a spatial structure in the DSD field at a $1 \times 1 \text{ km}^2$ scale for temporal resolution below 10 min for D_m and R and 30 min for N_t . Globally, for time steps of 30 min and larger, the observed variability is within the noise level inherent to the measuring process.

Finally, Chapter 4 illustrates a possible application of such information about the spatial structure of the DSD, namely the spatial representativity issue when upscaling from point (instrument) to areal (radar pixel) measurements. Because there is no sill/range in the fitted variograms, a stochastic simulation approach has been chosen. 1000 2D-fields are generated and constrained by the spatial structure previously observed. For each simulation, the value at the center of the field is compared to the value averaged over the pixel. The standard deviation of the 1000 simulations is an appropriate indicator of the average error due to the upscaling. Globally, the error associated with the upscaling is increasing with increasing domain size. For instance, the error associated with the upscaling of $N_t(R)$ for convective tape rainfall is ranging from 12% (18%) to 16% (24%) for domain size of $100 \times 100 \text{ m}^2$ and $1000 \times 1000 \text{ m}^2$ respectively.

It has been shown that the DSD fields are spatially organized within an area of about 1 km^2 , which can have a strong impact on the use at radar pixel scale of relationships derived at point scale (Chapter 4). This raises the question of the influence of this variability on radar rainfall estimators. This issue is addressed in Chapter 5 focusing on two particular power laws commonly used for radar rainfall estimations: the $Z-R$ (for conventional radar) and the $R-K_{dp}$ (for polarimetric radar) relationships. The power law parameters (a and b or c and d) are estimated from a non-linear regression of $Z-R$ and $R-K_{dp}$ scatterplots. The influence of the independent variable considered for regression (i.e., Z or R) is also investigated for the $Z-R$ relationship. Power law relationships are estimated at different spatial scales: using data from each instrument (point), using data from all point measurements (aggregate of points) and finally using the data averaged at each time step between the 16 instruments which provides a reliable estimate of the radar pixel. For robustness, the part of variability of the parameters induced by the sampling uncertainty associated with Parsivel has to be taken into account. As the sampling uncertainty associated with Parsivel measurements can not be assumed uniform over the network (recall that the sampling uncertainty is function of the magnitude of the quantity of interest), a stochastic simulation approach is considered to propagate the sampling uncertainty into the parameter estimation. For each of the 500 simulations and each station, a normal distribution centered on the value of the quantity measured with its standard deviation equal to the corresponding uncertainty value is generated. The power law parameters are estimated for each simulation and the 80% confidence interval of these 500 values provides an estimate of the propagation of the sampling uncertainty of Parsivel in the power law parametrization.

At a 60-s temporal resolution, the results show distinct groups of a and b (c and d) values according to the type of rainfall. Moreover, the variability of the power law parameters is significant even at $1 \times 1 \text{ km}^2$ area, i.e., the observed variability of the parameters is larger than the one due to the sampling process. As expected, the error associated with the estimates is lower for the aggregate of points and the pixel value than the single point estimates.

The influence of this variability on radar rainfall estimation is investigated. Considering the average reflectivity (over the 16 stations) as the one that should be seen by the radar, the rain rates and rain amounts theoretically estimated from a radar using the previously parametrized

Chapter 7. Summary and Conclusions

power laws are calculated. Globally, independently of the power law considered, it shows a deviation of single point estimates between -5 and + 15% from the one estimated for the pixel. Finally, the analyses show that the observed variability of the power law parameters is significant for temporal resolution below 30 min. For time steps of 30 min and above, the natural variability can not be clearly distinguished from the noise induced by the sampling process. Additional investigations have shown that the variability of these parameters seems 'stable' between the different temporal resolutions while the error associated with power law parameters estimates is strongly increasing for larger time steps.

The data set collected by the network of autonomous disdrometers during these 16 months have highlighted a significant variability of the DSD at the 1 km² scale. As this data set is far from being completely explored, it is easily available for the scientific community. In the same time, additional campaigns have been conducted in order to investigate the spatial variability of the DSD at different scales and for different climatologies. These campaigns have been briefly presented in Chapter 6 in order to illustrate different applications of the network of autonomous disdrometers. As a part of the HYMEX international project (HYdrological cycle in Mediterranean EXperiment), a preliminary field campaign has been conducted in Ardèche, France called *HPicoNet* focusing on high resolution sampling of Mediterranean rainfall. This campaign has involved 8 autonomous stations that have been deployed at 7 sampling locations so that a sampling location is equipped with a dual disdrometer setup for sampling uncertainty issues. Moreover, TB rain gauges have been collocated to the disdrometers. Finally, in order to provide information on the electrical charge of raindrops, an induction ring is completing the setup at two sampling locations. The experiment lasted for about 10 months and has collected DSD data for about 65 rainfall events. This promising setup should provide a powerful tool to better understand the spatial and temporal variability of the DSD in Mediterranean regions. In addition, in order to quantify the variability of the DSD as a function of the altitude, a field campaign has been conducted in Davos, Switzerland. 3 disdrometers have been deployed along a slope at different altitudes ranging from 1520 m to about 2550 m. The disdrometers have been tuned (higher voltage, heating) for working in difficult weather conditions. At the top of the transect of disdrometers, a 2DVD has been deployed in order to have additional information on the 2D shape of falling hydrometeors. The experiment lasted for 2.5 years and has collected DSD spectra for about 300 precipitation (liquid and solid) events. Finally, as microwave links used for telecommunication purpose have been shown to be a promising tool for rainfall monitoring, a campaign has been conducted in Dübendorf, Switzerland. The experiment involves a microwave link deployed over a 1.85 km path, 5 autonomous stations deployed at 4 sampling locations for ground validation and 3 TB rain gauges. This campaign has started on March 2011 and is still collecting data.

Main contributions of this work

In summary, the main contributions of this work are:

- During this PhD, the work has been first devoted to the design and the set up of an autonomous network of disdrometers that can be easily deployed in different locations (autonomous in term of power supply and data transmission) and different configurations (flexibility in the structure and the number of stations in the network).
- The sampling uncertainty associated with the disdrometer measurements has been quantified using an experimental approach based on measurements from collocated disdrometers for about 15 months. The sampling uncertainty has been estimated for quantities that can describe the DSD (i.e., N_t and D_m) as well as integral quantities of the DSD (i.e., R , Z and Z_{dr}).
- Using a selection of 36 rainfall events in the 16-month data set, that has been split up according to 3 different types of rainfall (i.e., convective, transitional and frontal), a geostatistical approach was considered (through variograms) to quantify the spatial structure of the DSD within the $1 \times 1 \text{ km}^2$ monitored area. Analyses show that the DSD fields are spatially organized and not randomly distributed. The observed structure of the DSD is significant for temporal resolutions below 30 min from which the natural variability of the DSD is within the noise associated by the sampling process.
- The influence of this variability on radar rainfall estimators has been investigated focusing the analyses on the Z - R (for conventional radar) and the R - K_{dp} (for polarimetric radar) relationships. As the sampling uncertainty associated with the instruments is propagated into the analyses, it shows that this variability of the DSD produces a significant variability, i.e., larger than the one induced by the sampling process, of the radar power law parameters. In terms of rain amount, this variability can induce deviations in rain amounts estimated from the radar between -5 and +15% the one estimated at the pixel scale (which is more representative of the pixel area).

Perspectives

The presented results are opening various perspectives, such as:

1. The usefulness of the developed *disdrometric station* is demonstrated by the different field campaigns in which some disdrometers are involved.
2. The collected data set is far from being explored as the analyses presented in this thesis have been conducted on a selection of 36 rainfall events. The considered rainfall events have been selected for their good agreements (deviation of less than 10% in term of rain amount) between Parsivel Station 43 and 2 collocated TB rain gauges. It would be

Chapter 7. Summary and Conclusions

of interest to extend the presented analyses on the whole liquid precipitation events collected in the 16-month data set to see if the results are (or not) similar to the one observed for the subset of 36 rainfall events.

3. In 2013, the Global Precipitation Measurement (GPM) satellite, devoted to the measurement of solid and liquid precipitation using a combination of active and passive sensing techniques, will be launched. The deployment of the network of 20 disdrometers (this is the maximum number of stations managed by this network in this configuration) over a GPM footprint (about $5 \times 5 \text{ km}^2$) should provide relevant data to investigate various issues related to precipitation estimation from space satellites such as, for instance, the spatial structure within the radar footprint, the influence of non-uniform beam filling and the disaggregation¹ of rainfall fields.
4. In addition, such network of disdrometers can be a useful tool for ground validation of numerical weather models. By comparing between spatially distributed measurements and simulations can help improving precipitation monitoring and forecasting.
5. In order to catch the decorrelation distance (if any) in the DSD fields, the deployment of the disdrometer network over a larger area (e.g., $25 \times 25 \text{ km}^2$) would be appropriate. This would also nicely complement the data set collected at the radar pixel scale and presented in this thesis.
6. Finally, the capability to use radio modem to gather information from slave stations and to then send it in real time to a safe archiving system via the mobile phone network can certainly be adapted to the monitoring of other environmental variables.

¹ *disaggregation* is generic term to describe techniques used to generate higher spatial resolution from a coarse resolution

A Electronic diagram: Solar control

(kindly provided by A. Studzinski)

As the voltage provided by the solar panel can be up to 17 V (depending on the sunlight and the altitude), the battery can not be directly connected to the solar panel. To increase battery's lifetime, an electronic circuit (connected between the solar panel and the battery) is controlling in real time the battery's voltage (denoted hereafter U_{bat}). The charge cycles of the battery are defined according to the following modes:

- $U_{bat} \leq 13.8$ V: full load charge mode.
- $13.8 < U_{bat} \leq 14.9$ V: reduced load charge (30% duty cycle).
- $U_{bat} > 14.9$ V: floating charge (7% duty cycle)

Figure A.1 presents a picture of this electronic circuit and the associated diagram is provided in the next page.

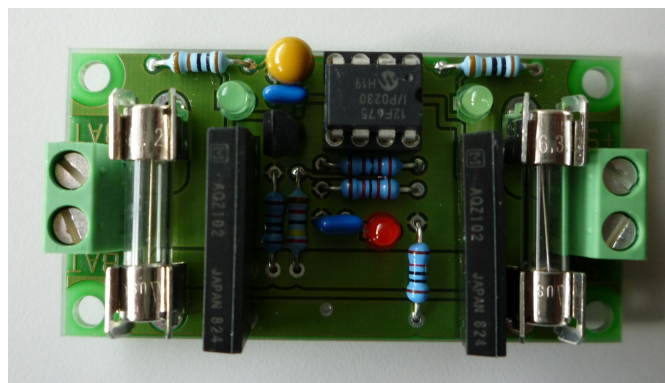
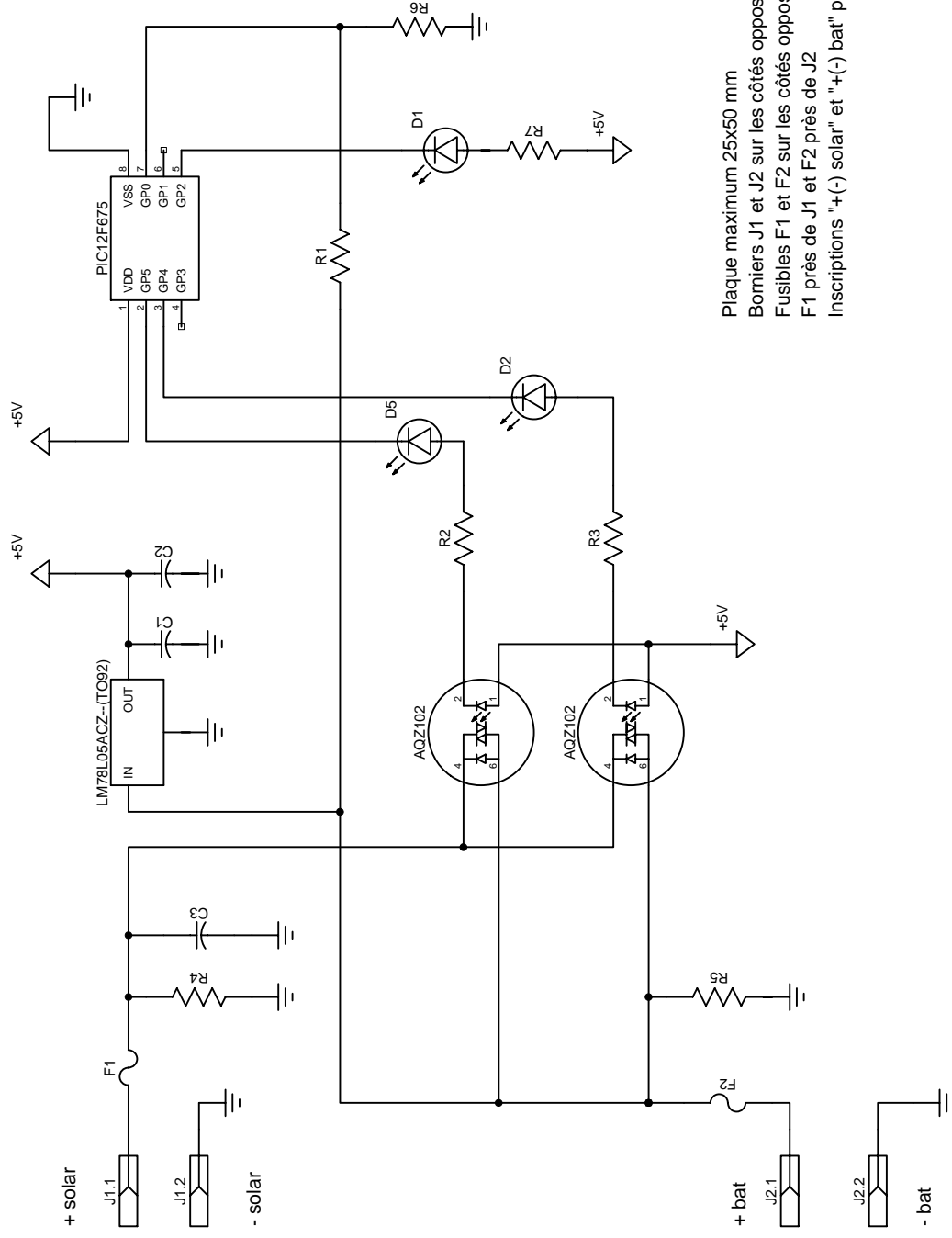


Figure A.1: Picture of the electronic circuit controlling the power provided by the solar panel to the battery.



Plaque maximum 25x50 mm

Borniers J1 et J2 sur les côtés opposés de la plaque

Fusibles F1 et F2 sur les côtés opposés de la plaque

F1 près de J1 et F2 près de J2

Inscriptions "+(-) solar" et "+(-) bat" près des bornes respectives

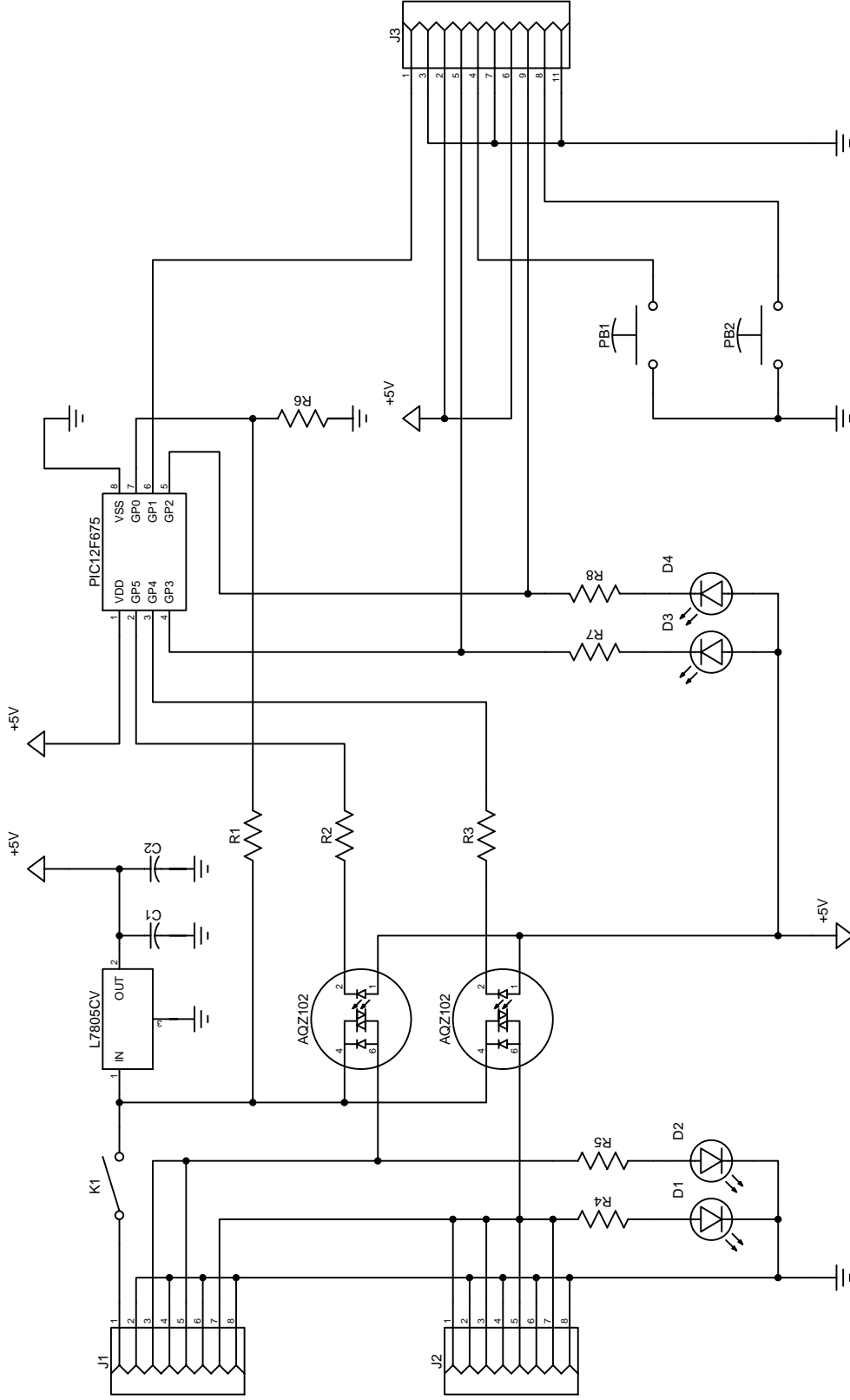
LPAS	Load controller of lead battery for solar systems	
Designed by A.-P. Studzinski	Checked by	Date 28.06.08
All capacitors: 2,54 mm Resistors, diodes: 10,16 mm LED: 2,54 mm J1, J2 grid 5,08 mm Ø 1,3 mm (Compona) Fuses (6x20mm): 2 holes Ø 1,3 mm, distance 22,1 mm		Scale 1:1
Edition 0		Sheet 1/1

B Electronic diagram: Station power control (kindly provided by A. Studzinski)

To prevent from possible default and malfunctioning of the station due to low voltage, the incoming voltage is controlled in real time. For the first switch on of a station, the voltage should be higher than 11 V. For an operating station, the electronic circuit switch off the station as soon as the voltage reach 10.5 V. The station is switch on again only after a dead time of 1 h (in order to prevent from hysteresis phenomenon) and if the power supply provided by the battery is above 12 V.

Moreover, the '*station power control*' circuit reset the station (switch off, 5 min break and switch on) if one of the following condition is fulfilled:

- Radio communication problem: no one of the 3 slave stations is providing data for 6 h
- Parsivel communication default (for each station)
- GPRS communication default



LPAS Power control device for Parsivel installation

Designed by
A.-P. Studzinski

Checked by

Date
28.07.07

Scale
1:1

All capacitors: 2,54 mm
J1, J2, J3: 2,54 mm
Resistors: 10,16 mm
LED: 2,54 mm

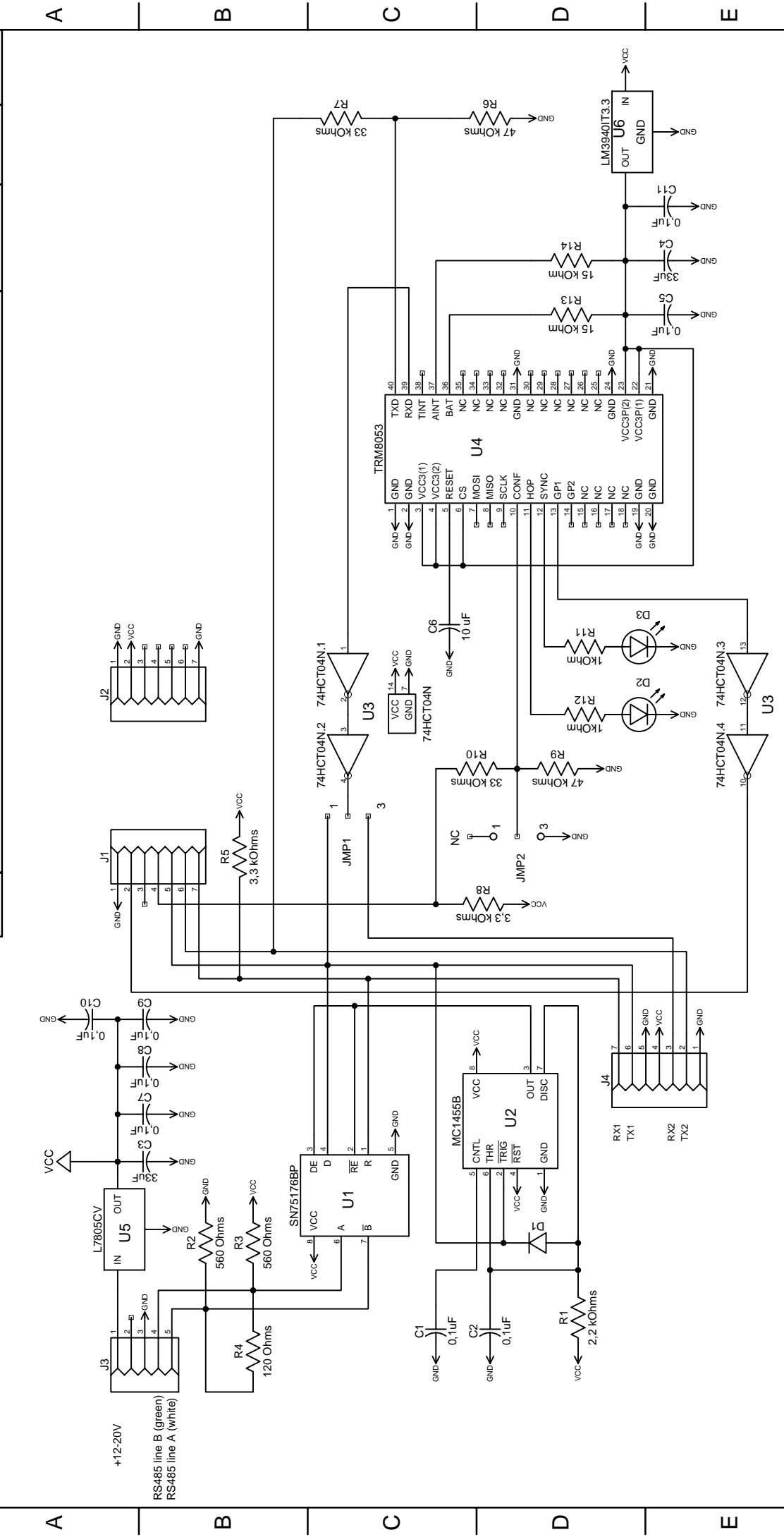
Edition
0

Sheet
1/1

C Electronic diagram: RS485 to RS232TTL converter

(kindly provided by A. Studzinski)

As Parsivel output is RS485 while campbell data loger input is RS232TTL, a converter have been designed and connected between Parsivel and the logger. The converter is equipped with a long range radio modem in order to query data for the slave stations. The electronic diagram of the RS485 to RS232TTL converter is presented hereafter.

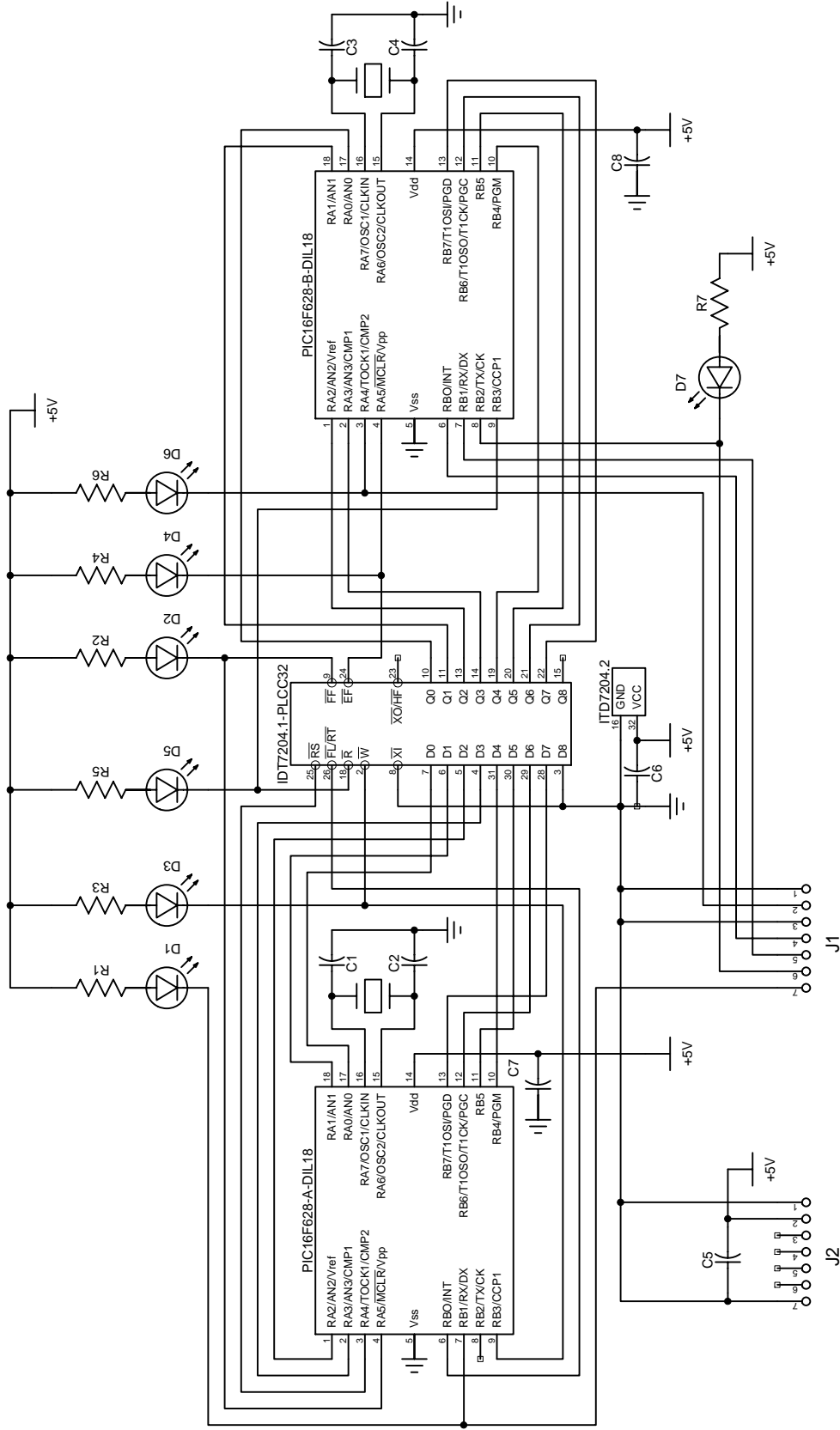


File: RS485-TRM8053.DCH		Date	Scale
Designed by A..P. Studzinski		12.05.08	1:1
R1, R2... D1	7,62 mm	RS485 – UART – Radiomodem (Y-Lynx) converter	
D2, D3, C1, C2...	2,54 mm		
J1, J2, J3, J4	2,54 mm grid (In Line)		
JMP1, JMP2	2,54 mm grid (In Line)		
Edition		Sheet	
0		1/1	

D Electronic diagram: FIFO

(kindly provided by A. Studzinski)

Because radio disturbances during data transmission can happen, the system have been designed to repeat the data transmission up to 8 times per slave station if necessary. During the time required to repeat data transmission, the data collected by Parsivel is stored in a buffer memory denoted FIFO (First In First Out). This FIFO is as well the electronic component that provide the address (and hence the associated range of frequency considered) to the slave station. The electronic diagram of the FIFO is presented hereafter.



LPAS	Fifo for communication between an USART and radiomodem device	
Designed by A.-P. Studzinski	Checked by	Date 28.07.07
C1, C2, C3, C4: 2,54 mm C5, C6, C7, C8: 5,08 mm J1, J2: 2,54 mm LEDs: 2,54 mm Crystal 5,08 mm Resistors: 10,16 mm		Scale 1:1
Edition 0		Sheet 1/1

E Calculation of the relative sampling uncertainty

Taking $X = \overline{m}_{S_k} = \frac{1}{k} \sum_{i \in S_k} (M + \omega_i)$ and $Y = \overline{m}_n = \frac{1}{n} \sum_{i=1}^n (M + \omega_i)$, we have according to Eq (3.12):

$$\sigma_{\varepsilon_{S_k}}^2 = \text{Var} \left[\frac{X}{Y} \right] . \quad (\text{E.1})$$

X and Y being two strictly positive random variables, we have according to Stuart and Ord [1994, p.351]:

$$\text{Var} \left[\frac{X}{Y} \right] = \frac{\text{E}^2[X]}{\text{E}^2[Y]} \left(\frac{\text{Var}[X]}{\text{E}^2[X]} - 2 \frac{\text{Cov}(X, Y)}{\text{E}[X]\text{E}[Y]} + \frac{\text{Var}[Y]}{\text{E}^2[Y]} \right) + o(n_s^{-1}) \quad (\text{E.2})$$

with n_s the number of samples (time steps) considered in the class of interest ($n_s \geq 30$). All collocated sensors are supposed to sample the same population of DSDs.

$$\text{E}[X] = \text{E} \left[\frac{1}{k} \sum_{i \in S_k} (M + \omega_i) \right] = \text{E} \left[\frac{1}{k} \sum_{i \in S_k} M \right] + \text{E} \left[\frac{1}{k} \sum_{i \in S_k} \omega_i \right] \quad (\text{E.3})$$

The sampling error ω_i is assumed to be a Gaussian white noise, consequently

$$\text{E}[\omega_i] = 0 \quad \forall i \in n \quad (\text{E.4})$$

$$\text{Cov}[\omega_i, \omega_j] = 0 \quad \forall i \neq j . \quad (\text{E.5})$$

Therefore we have:

$$\text{E}[X] = \text{E}[Y] = \text{E}[M] . \quad (\text{E.6})$$

Assuming in addition that M and ω are not correlated within the classes of the considered quantity related the DSD ($\text{Cov}[M, \omega_i] = 0$) and that the sampling uncertainty has a similar

Appendix E. Calculation of the relative sampling uncertainty

distribution for all sensors ($\sigma_{\omega_i} = \sigma_{\omega_j} = \sigma_{\omega} \quad \forall i, j$), we have:

$$\text{Var}[X] = \text{Var}[\bar{m}_{S_k}] = \sigma_M^2 + \frac{1}{k}\sigma_{\omega}^2 \quad (\text{E.7})$$

$$\text{Var}[Y] = \text{Var}[\bar{m}_n] = \sigma_M^2 + \frac{1}{n}\sigma_{\omega}^2 \quad (\text{E.8})$$

$$\text{Cov}[X, Y] = \text{Var}[Y] = \sigma_M^2 + \frac{1}{n}\sigma_{\omega}^2 \quad (\text{E.9})$$

Substituting Eq(E.6), (E.7), (E.8) and (E.9) in Eq(E.2), the variance of ε_{S_k} is approximated as

$$\text{Var}[\varepsilon_{S_k}] \simeq \frac{\sigma_{\omega}^2}{E^2[M]} \left(\frac{1}{k} - \frac{1}{n} \right) . \quad (\text{E.10})$$

Then, the relative sampling uncertainty σ_{ω}^r can be calculated from $\sigma_{\varepsilon_{S_k}}$

$$\sigma_{\omega}^r = \frac{\sigma_{\omega}}{E[M]} \simeq \sigma_{\varepsilon_{S_k}} \sqrt{\frac{nk}{n-k}} . \quad (\text{E.11})$$

F Experimental values of the sampling uncertainty σ_{ω}^r

The sampling uncertainty σ_{ω}^r have been expressed as a function of the temporal resolution and the variable intensity classes. The following values correspond to the ones presented in Figure 3.10, 3.11, 3.13, 3.15 and 3.17.

Table F.1: Relative sampling uncertainty associated with N_t estimates.

	Classes [m ⁻³]	Δt										
		20 s	60 s	120 s	180 s	240 s	300 s	600 s	900 s	1800 s	2700 s	3600 s
N_t	[0,50[0.25	0.17	0.13	0.12	0.11	0.09	0.07	0.07	0.06	0.05	0.04
	[50,100[0.22	0.14	0.11	0.09	0.08	0.08	0.07	0.06	0.05	0.06	0.05
	[100,200[0.17	0.11	0.09	0.07	0.07	0.07	0.06	0.06	0.05	0.05	0.05
	[200,400[0.13	0.08	0.07	0.06	0.06	0.06	0.05	0.04	0.04	0.04	0.04
	[400,600[0.10	0.07	0.05	0.05	0.05	0.04	0.04	0.04	0.03	0.04	-
	[600,800[0.09	0.06	0.05	0.05	0.04	0.04	0.04	-	-	-	-
	[800,1000[0.08	0.06	0.05	0.05	0.04	-	-	-	-	-	-
	[1000,1500[0.07	0.05	0.05	0.04	-	-	-	-	-	-	-
	[1500,2000[0.07	-	-	-	-	-	-	-	-	-	-

Table F.2: Relative sampling uncertainty associated with D_0 estimates.

	Classes [mm]	Δt										
		20 s	60 s	120 s	180 s	240 s	300 s	600 s	900 s	1800 s	2700 s	3600 s
D_0	[0.6,0.7[0.05	0.03	0.03	0.02	0.02	0.02	0.02	0.02	0.01	-	-
	[0.7,0.8[0.06	0.04	0.03	0.03	0.03	0.02	0.02	0.02	0.02	0.02	0.02
	[0.8,0.9[0.06	0.04	0.03	0.03	0.03	0.03	0.02	0.02	0.02	0.02	0.02
	[0.9,1[0.08	0.05	0.04	0.04	0.04	0.03	0.03	0.03	0.03	0.03	0.03
	[1,1.25[0.10	0.06	0.05	0.05	0.04	0.04	0.04	0.04	0.04	0.04	0.03
	[1.25,1.5[0.11	0.07	0.06	0.05	0.05	0.04	0.04	0.04	0.04	0.03	0.03
	[1.5,1.75[0.15	0.10	0.08	0.06	0.07	0.06	0.05	0.06	0.03	0.03	-
	[1.75,2[0.19	0.10	0.09	0.08	0.07	0.06	0.06	-	-	-	-
	[2,2.25[0.22	0.14	0.10	0.12	0.07	-	-	-	-	-	-
	[2.25,2.5[0.27	0.15	-	-	-	-	-	-	-	-	-

Appendix F. Experimental values of the sampling uncertainty

Table F3: Relative sampling uncertainty associated with R estimates.

	R Classes [mm h ⁻¹]	Δt										
		20 s	60 s	120 s	180 s	240 s	300 s	600 s	900 s	1800 s	2700 s	3600 s
P a r s i v e l	[0,1,2[0.25	0.18	0.15	0.13	0.12	0.12	0.11	0.10	0.10	0.10	0.09
	[2,4[0.21	0.15	0.12	0.11	0.11	0.10	0.10	0.10	0.08	0.09	0.09
	[4,6[0.20	0.14	0.12	0.11	0.09	0.09	0.08	0.07	0.07	-	-
	[6,8[0.18	0.13	0.11	0.10	0.09	0.09	0.07	0.07	-	-	-
	[8,10[0.16	0.11	0.09	0.10	0.06	0.08	-	-	-	-	-
	[10,15[0.16	0.12	0.11	0.08	0.08	-	-	-	-	-	-
	[15,20[0.16	0.10	-	-	-	-	-	-	-	-	-
	[20,25[0.13	-	-	-	-	-	-	-	-	-	-
	[25,30[0.13	-	-	-	-	-	-	-	-	-	
T B g a u g e	[0,1,2[1.10	1.10	1.10	1.10	1.10	1.10	1.10	0.37	0.22	0.14	0.11
	[2,4[1.10	1.10	1.10	0.37	0.37	0.22	0.12	0.09	0.05	0.04	0.04
	[4,6[1.10	1.10	0.37	0.22	0.19	0.16	0.09	0.05	0.04	-	-
	[6,8[1.10	0.37	0.22	0.16	0.14	0.11	0.07	0.05	-	-	-
	[8,10[1.10	0.37	0.22	0.17	0.10	0.15	-	-	-	-	-
	[10,15[1.10	0.37	0.33	0.28	0.13	-	-	-	-	-	-
	[15,20[1.10	0.39	-	-	-	-	-	-	-	-	-
	[20,25[0.74	-	-	-	-	-	-	-	-	-	-
	[25,30[0.69	-	-	-	-	-	-	-	-	-	

Table F4: Relative sampling uncertainty associated with Z_h estimates (in dBZ) at X- (9.4 GHz), C- (5.6 GHz) and S-band (2.8 GHz) respectively.

	Classes [dBZ]	Δt											
		20 s	60 s	120 s	180 s	240 s	300 s	600 s	900 s	1800 s	2700 s	3600 s	
X	[10,15[0.12	0.09	0.08	0.07	0.07	0.06	0.06	0.05	0.06	0.06	0.05	
	[15,20[0.11	0.08	0.07	0.06	0.06	0.06	0.05	0.05	0.05	0.05	0.05	
	[20,25[0.09	0.06	0.05	0.05	0.05	0.05	0.04	0.04	0.04	0.04	0.04	
	b	[25,30[0.08	0.06	0.05	0.05	0.04	0.04	0.04	0.04	0.05	0.05	0.04
	a	[30,35[0.09	0.07	0.06	0.06	0.06	0.06	0.06	0.06	0.05	0.05	0.05
	n	[35,40[0.14	0.11	0.09	0.07	0.07	0.07	0.06	0.05	0.04	0.03	0.03
	d	[40,45[0.17	0.10	0.09	0.08	0.07	0.06	0.05	0.04	-	-	-
	[45,50[0.15	0.13	0.06	-	-	-	-	-	-	-	-	
C	[10,15[0.12	0.09	0.08	0.07	0.07	0.06	0.06	0.05	0.06	0.06	0.05	
	[15,20[0.11	0.08	0.07	0.06	0.06	0.06	0.05	0.05	0.05	0.05	0.05	
	[20,25[0.09	0.07	0.06	0.05	0.05	0.05	0.04	0.04	0.04	0.03	0.03	
	b	[25,30[0.09	0.06	0.05	0.04	0.04	0.04	0.04	0.03	0.03	0.03	0.03
	a	[30,35[0.09	0.06	0.04	0.04	0.04	0.04	0.03	0.03	0.04	0.03	0.03
	n	[35,40[0.08	0.05	0.04	0.04	0.04	0.04	0.04	0.05	0.07	0.06	0.06
	d	[40,45[0.06	0.11	0.06	0.13	0.13	0.13	0.09	-	-	-	-
	[45,50[0.17	0.19	0.20	-	-	-	-	-	-	-	-	
S	[10,15[0.12	0.09	0.08	0.07	0.07	0.06	0.06	0.05	0.06	0.06	0.06	
	[15,20[0.11	0.08	0.07	0.06	0.06	0.06	0.05	0.05	0.05	0.05	0.05	
	[20,25[0.09	0.07	0.06	0.05	0.05	0.05	0.04	0.04	0.04	0.04	0.04	
	b	[25,30[0.09	0.06	0.05	0.04	0.04	0.04	0.04	0.04	0.03	0.03	0.03
	a	[30,35[0.09	0.06	0.05	0.04	0.04	0.04	0.03	0.04	0.03	0.03	0.03
	n	[35,40[0.09	0.06	0.05	0.04	0.04	0.04	0.03	0.04	0.03	0.02	0.02
	d	[40,45[0.09	0.08	0.07	0.06	0.05	0.04	-	-	-	-	-
	[45,50[0.11	0.04	-	-	-	-	-	-	-	-	-	

Appendix F. Experimental values of the sampling uncertainty

Table F5: Relative sampling uncertainty associated with Z_{dr} estimates (in dB) at X- (9.4 GHz), C- (5.6 GHz) and S-band (2.8 GHz) respectively.

	Classes [dBZ]	Δt										
		20 s	60 s	120 s	180 s	240 s	300 s	600 s	900 s	1800 s	2700 s	3600 s
X band	[0.1,0.2[0.16	0.12	0.11	0.10	0.10	0.10	0.08	0.08	0.08	0.08	0.08
	[0.2,0.3[0.22	0.18	0.16	0.15	0.14	0.13	0.12	0.11	0.11	0.11	0.10
	[0.3,0.4[0.28	0.22	0.20	0.19	0.18	0.17	0.17	0.16	0.14	0.13	0.13
	[0.4,0.5[0.31	0.26	0.23	0.23	0.21	0.21	0.17	0.17	0.15	0.14	0.14
	[0.5,0.75[0.36	0.31	0.27	0.25	0.25	0.24	0.21	0.21	0.22	0.19	0.21
	[0.75,1[0.41	0.37	0.35	0.32	0.31	0.30	0.30	0.31	0.31	0.32	0.30
	[1,1.5[0.47	0.43	0.40	0.39	0.40	0.41	0.38	0.35	0.32	0.35	0.32
	[1.5,2[0.50	0.46	0.44	0.43	0.41	0.39	0.36	0.34	0.30	0.28	0.24
[2,3[0.49	0.44	0.41	0.39	0.38	0.32	0.31	0.35	0.23	0.23	0.16	
C band	[0.1,0.2[0.16	0.12	0.11	0.10	0.10	0.10	0.08	0.08	0.08	0.08	0.08
	[0.2,0.3[0.22	0.18	0.17	0.15	0.15	0.14	0.12	0.11	0.11	0.11	0.10
	[0.3,0.4[0.28	0.22	0.20	0.19	0.18	0.17	0.17	0.15	0.14	0.13	0.14
	[0.4,0.5[0.30	0.26	0.23	0.23	0.21	0.20	0.17	0.16	0.16	0.13	0.12
	[0.5,0.75[0.35	0.29	0.25	0.23	0.21	0.20	0.18	0.18	0.15	0.14	0.15
	[0.75,1[0.39	0.33	0.27	0.24	0.24	0.25	0.21	0.17	0.19	0.19	0.19
	[1,1.5[0.44	0.37	0.33	0.32	0.28	0.27	0.25	0.25	0.21	0.21	0.23
	[1.5,2[0.50	0.42	0.41	0.41	0.42	0.37	0.37	0.39	-	-	-
[2,3[0.53	0.50	0.47	0.49	0.51	0.47	0.53	0.56	-	-	-	
S band	[0.1,0.2[0.16	0.12	0.11	0.10	0.10	0.10	0.08	0.08	0.08	0.08	0.08
	[0.2,0.3[0.22	0.18	0.17	0.15	0.15	0.14	0.12	0.11	0.11	0.11	0.10
	[0.3,0.4[0.28	0.22	0.20	0.19	0.19	0.18	0.17	0.16	0.14	0.13	0.14
	[0.4,0.5[0.30	0.26	0.23	0.23	0.21	0.21	0.17	0.16	0.16	0.14	0.13
	[0.5,0.75[0.35	0.29	0.26	0.23	0.22	0.21	0.19	0.18	0.16	0.14	0.15
	[0.75,1[0.39	0.33	0.27	0.25	0.24	0.26	0.23	0.20	0.21	0.22	0.20
	[1,1.5[0.43	0.38	0.35	0.33	0.31	0.29	0.27	0.28	0.25	0.21	0.22
	[1.5,2[0.49	0.43	0.41	0.40	0.40	0.38	0.38	0.38	0.36	-	-
[2,3[0.50	0.47	0.42	0.43	0.43	0.37	0.26	0.29	0.17	0.25	-	

Bibliography

- Agassi, M., D. Bloem, and M. Benhur, 1994: Effect of drop energy and soil and water chemistry on infiltration and erosion. *Water Resour. Res.*, **30** (4), 1187–1193.
- Anagnostou, M. N., J. Kalogiros, E. N. Anagnostou, M. Tarolli, A. Papadopoulos, and M. Borga, 2009: Performance evaluation of high-resolution rainfall estimation by x-band dual-polarization radar for flash flood applications in mountainous basins. *J. Hydrol.*, **394** (1-2), 4–16, doi:10.1016/j.jhydrol.2010.06.026.
- Andsager, K., K. V. Beard, and N. F. Laird, 1999: Laboratory measurements of axis ratios for large rain drops. *J. Atmos. Sci.*, **56** (15), 2673–2683.
- Armstrong, M. and P. Delfiner, 1980: Towards a more robust variogram: A case study on coal. Technical Report N-671, Centre de Géostatistique, Fontainebleau, France.
- Assouline, S., 2009: Drop size distributions and kinetic energy rates in variable intensity rainfall. *Water Resour. Res.*, **45**, doi:10.1029/2009WR007927.
- Atlas, D., C. W. Ulbrich, F. D. Marks, E. Amitai, and C. R. Williams, 1999: Systematic variation of drop size and radar-rainfall relations. *J. Geophys. Res.*, **104** (D6), 6155–6169.
- Barry, R. G. and R. J. Chorley, 2003: *Atmospheric, Weather and Climate*. Routledge, London and New York, 421 pp.
- Battaglia, A., E. Rustemeier, A. Tokay, U. Blahak, and C. Simmer, 2010: PARSIVEL Snow Observations: A Critical Assessment. *J. Atmos. Oceanic Technol.*, **27** (2), 333–344, doi: 10.1175/2009JTECHA1332.1.
- Battan, L. J., 1973: *Radar observation of the atmosphere*. University of Chicago Press, 324 pp.
- Beard, K. V., 1977: Terminal velocity adjustment for cloud and precipitation drops aloft. *J. Atmos. Sci.*, **34** (8), 1293–1298.
- Berne, A., G. Delrieu, J.-D. Creutin, and C. Obled, 2004: Temporal and spatial resolution of rainfall measurements required for urban hydrology. *J. Hydrol.*, **299** (3-4), 166–179.
- Berne, A. and R. Uijlenhoet, 2005a: Quantification of the radar reflectivity sampling error in non-stationary rain using paired disdrometers. *Geophys. Res. Lett.*, **32** (19), L19813, doi: 10.1029/2005GL024030.

Bibliography

- Berne, A. and R. Uijlenhoet, 2005b: A stochastic model of range profiles of raindrop size distributions: application to radar attenuation correction. *Geophys. Res. Lett.*, **32** (10), L10803, doi:10.1029/2004GL021899.
- Blumenfeld, K. A. and R. H. Skaggs, 2011: Using a high-density rain gauge network to estimate extreme rainfall frequencies in minnesota. *Appl. Geogr.*, **31**, 5–11, doi:10.1016/j.apgeog.2010.03.013.
- Bringi, V. N. and V. Chandrasekar, 2001: *Polarimetric doppler weather radar*. Cambridge University Press, 662 pp.
- Brutsaert, W., 2005: *Hydrology: An Introduction*. Cambridge University Press, 605 pp.
- Campos, E. and I. Zawadzki, 2000: Instrumental uncertainties in Z-R relations. *J. Appl. Meteor.*, **39** (7), 1088–1102.
- CH2011, 2011: *Swiss Climate Change Scenarios CH2011*. C2SM, MeteoSwiss, ETH, NCCR Climate, and OcCC, Zurich, Switzerland, 88 pp.
- Chandrasekar, V. and E. G. Gori, 1991: Multiple disdrometer observations of rainfall. *J. Appl. Meteor.*, **30**, 1514–1520.
- Chapon, B., G. Delrieu, M. Gosset, and B. Boudevillain, 2008: Variability of rain drop size distribution and its effect on the Z-R relationship: a case study for intense Mediterranean rainfall. *Atmos. Res.*, **87** (1), 52–65.
- Chilès, J.-P. and P. Delfiner, 1999: *Geostatistics: Modeling spatial uncertainty*. Probability and statistics, Wiley, 695 pp.
- Chvíla, B. and B. Sevruk, 2008: Intercomparison measurements by ground level and elevated disdrometer. INSTRUMENTS AND OBSERVING METHODS 96, World Meteorological Organization, 6 pp., Geneva. Available on CD-Rom.
- Ciach, G. J., 2003: Local random errors in tipping-bucket rain gauge measurements. *J. Atmos. Oceanic Technol.*, **20** (5), 752–759, doi:10.1175/1520-0426(2003)20<752:LREITB>2.0.CO;2.
- Ciach, G. J. and W. F. Krajewski, 1999: Radar-rain gauge comparisons under observational uncertainties. *J. Appl. Meteor.*, **38** (10), 1519–1525, doi:10.1175/1520-0450(1999)038<1519:RRGCUO>2.0.CO;2.
- Ciach, G. J. and W. F. Krajewski, 2006: Analysis and modeling of spatial correlation structure in small-scale rainfall in central Oklahoma. *Adv. Water Resour.*, **29** (5), 1450–1463, doi:10.1016/j.advwaters.200511.003.
- Confalonieri, U., B. Menne, R. Akhtar, K. L. Ebi, R. S. Hauengue, M. and Kovats, B. Revich, and A. Woodward, 2007: Human health. *Climate Change 2007: Impacts, Adaptation and Vulnerability. Contribution of Working Group II to the Fourth Assessment Report of the Intergovernmental Panel on Climate Change*, M. L. Parry, O. F. Canziani, J. P. Palutikof,

- P. J. van der Linden, and C. E. Hanson, Eds., Cambridge University Press, Cambridge, UK, 391–431.
- Doelling, I. G., J. J., and R. J., 1998: Systematic variations of Z-R-relationships from drop size distributions measured in northern germany during seven years. *Atmos. Res.*, **48**, 635–649.
- Easterling, W. E., et al., 2007: Food, fibre and forest products. *Climate Change 2007: Impacts, Adaptation and Vulnerability. Contribution of Working Group II to the Fourth Assessment Report of the Intergovernmental Panel on Climate Change*, M. L. Parry, O. F. Canziani, J. P. Palutikof, P. J. Van der Linden, and C. E. Hanson, Eds., Cambridge University Press, Cambridge, UK, 273–313.
- Eckhardt, K. and U. Ulbrich, 2003: Potential impacts of climate change on groundwater recharge and streamflow in a central european low mountain range. *J. Hydrol.*, **284**, 244–252, doi:10.1016/j.jhydrol.2003.08.005.
- Egli, L., T. Jonas, and R. Meister, 2009: Comparison of different automatic methods for estimating snow water equivalent. *Cold Regions Science and Technology*, **57**, 107–115, doi:10.1016/j.coldregions.2009.02.008.
- Feingold, G. and Z. Levin, 1986: The lognormal fit to raindrop spectra for convective clouds in Israel. *J. Climate Appl. Meteor.*, **25**, 1346–1363.
- Frei, C., C. Schär, D. Lüthi, and H. C. Davies, 1998: Heavy precipitation processes in a warmer climate. *Geophys. Res. Lett.*, **25 (9)**, 1431–1434, doi:10.1029/98GL51099.
- Gage, K. S., W. L. Clark, C. R. Williams, and A. Tokay, 2004: Determining reflectivity measurement error from serial measurements using paired disdrometers and profilers. *Geophys. Res. Lett.*, **31**, L23107, doi:10.1029/2004GL020591.
- Germann, U., G. Galli, M. Boscacci, and M. Bolliger, 2006: Radar precipitation measurement in a mountainous region. *Q. J. Roy. Meteor. Soc.*, **132 (618)**, 1669–1692, doi:10.1256/qj.05.190.
- Gertzman, H. S. and D. Atlas, 1977: Sampling errors in the measurement of rain and hail parameters. *J. Geophys. Res.*, **82 (31)**, 4955–4966.
- Groisman, P. Y., R. W. Knight, D. R. Easterling, T. R. Karl, G. C. Hegerl, and V. N. Razuvaev, 2005: Trends in intense precipitation in the climate record. *J. Climate*, **18 (9)**, 1326–1350, doi:10.1175/JCLI3339.1.
- Habib, E., W. F. Krajewski, and G. J. Ciach, 2001a: Estimation of rainfall interstation correlation. *J. Hydrometeor.*, **2 (6)**, 621–629, doi:10.1175/1525-7541(2001)002<0621:EORIC>2.0.CO;2.
- Habib, E., W. F. Krajewski, and A. Kruger, 2001b: Sampling errors of tipping-bucket rain gauge measurements. *J. Hydrol. Eng.*, **6 (2)**, 159–166, doi:10.1061/(ASCE)1084-0699(2001)6:2(159).
- Henson, W., G. Austin, and H. Oudenhoven, 2004: Development of an inexpensive raindrop size spectrometer. *J. Atmos. Oceanic Technol.*, **21**, 1710–1717.

Bibliography

- Huffman, G. J., R. F. Adler, M. Morrissey, D. T. Bolvin, S. Curtis, R. Joyce, B. McGavock, and J. Susskind, 2001: Global Precipitation at one-degree daily resolution from multi-satellite observations. *J. Hydrometeor.*, **2**, 36–50.
- Huntington, T. G., 2006: Evidence for intensification of the global water cycle: Review and synthesis. *J. Hydrol.*, **319** (1-4), 83–95, doi:10.1016/j.jhydrol.2005.07.003.
- IPCC, 2007: *Climate Change 2007: Impacts, Adaptation and Vulnerability. Contribution of Working Group II to the Fourth Assessment Report of the Intergovernmental Panel on Climate Change*. Cambridge University Press ed., M.L. Parry, O.F. Canziani, J.P. Palutikof, P.J. van der Linden and C.E. Hanson, Cambridge, UK, 976 pp.
- Jaffrain, J. and A. Berne, 2011: Experimental quantification of the sampling uncertainty associated with measurements from Parsivel disdrometers. *J. Hydrometeor.*, **12** (3), doi: 10.1175/2010JHM1244.1.
- Jaffrain, J., A. Studzinski, and A. Berne, 2011: A network of disdrometers to quantify the small-scale variability of the raindrop size distribution. *Water Resour. Res.*, **47**, doi:10.1029/2010WR009872.
- Jameson, A. R. and A. B. Kostinski, 2001: What is a raindrop size distribution? *Bull. Amer. Meteor. Soc.*, **82** (6), 1169–1177.
- Jones, P. D., T. J. Osborn, and K. R. Briffa, 1997: Estimating sampling errors in large-scale temperature averages. *J. Climate*, **10** (10), 2548–2568.
- Joss, J. and E. Gori, 1978: Shapes of raindrop size distributions. *J. Appl. Meteor.*, **17**, 1054–1061.
- Joss, J. and A. Waldvogel, 1967: Ein spektrograph für niederschlagstropfen mit automatischer auswertung / a spectrograph for raindrops with automatic interpretation. *Pageoph*, **68**, 240–246.
- Joss, J. and A. Waldvogel, 1969: Raindrop size distribution and sampling size errors. *J. Atmos. Sci.*, **26**, 566–569.
- Journel, A. G. and C. J. Huijbregts, 1978: *Mining geostatistics*. Academic Press, London, 600 pp.
- Keenan, T. D., L. D. Carey, D. S. Zrnić, and P. T. May, 2001: Sensitivity of 5-cm wavelength polarimetric radar variables to raindrop axial ratio and drop size distribution. *J. Appl. Meteor.*, **40** (3), 526–545, doi:10.1175/1520-0450(2001)040<0526:SOCWPR>2.0.CO;2.
- Keim, R. F., A. E. Skaugset, and M. Weiler, 2006: Storage of water on vegetation under simulated rainfall of varying intensity. *Adv. Water Resour.*, **29** (7), 974–986, doi:10.1016/j.advwatres.2005.07.017.
- Krajewski, W. F. and J. A. Smith, 2002: Radar hydrology: rainfall estimation. *Adv. Water Resour.*, **25** (8-12), 1387–1394, doi:10.1016/j.advwatres.2005.03.018.

- Krajewski, W. F., et al., 2006: DEVEX-disdrometer evaluation experiment: basic results and implications for hydrologic studies. *Adv. Water Resour.*, **29**, 807–814, doi:10.1016/j.advwatres.2005.03.018.
- Kruger, A. and W. F. Krajewski, 2002: Two-dimensional video disdrometer: a description. *J. Atmos. Oceanic Technol.*, **19** (5), 602–617.
- Kundzewicz, Z. W., et al., 2007: Freshwater resources and their management. *Climate Change 2007: Impacts, Adaptation and Vulnerability. Contribution of Working Group II to the Fourth Assessment Report of the Intergovernmental Panel on Climate Change*, M. L. Parry, O. F. Canziani, J. P. Palutikof, P. J. Van der Linden, and C. E. Hanson, Eds., Cambridge University Press, Cambridge, UK, 173–210.
- Lee, C. K., G. Lee, I. Zawadzki, and K. Kim, 2009: A preliminary analysis of spatial variability of raindrop size distributions during stratiform rain events. *J. Appl. Meteor. Climate*, **48** (2), 270–283, doi:10.1175/2008JAMC1877.1.
- Lee, G., A. W. Seed, and I. Zawadzki, 2007: Modeling the variability of drop size distributions in space and time. *J. Appl. Meteor. Climate*, **46** (7), 742–756, doi:10.1175/JAM2505.1.
- Lee, G. and I. Zawadzki, 2005: Variability of drop size distributions: time-scale dependence of the variability and its effects on rain estimation. *J. Appl. Meteor.*, **44** (2), 241–255, doi:10.1175/JAM2183.1.
- Leijnse, H., R. Uijlenhoet, and J. N. M. Stricker, 2007: Rainfall measurement using radio links from cellular communication networks. *Water Resour. Res.*, **43** (3), W03 201, doi:10.1029/2006WR005631.
- Löffler-Mang, M. and U. Blahak, 2001: Estimation of the equivalent radar reflectivity factor from measured snow size spectra. *J. Appl. Meteor.*, **40**, 843–849.
- Löffler-Mang, M. and J. Joss, 2000: An optical disdrometer for measuring size and velocity of hydrometeors. *J. Atmos. Oceanic Technol.*, **17**, 130–139.
- Mapiam, P. P., N. Sriwongsitanon, S. Chumchean, and A. Sharma, 2009: Effects of rain gauge temporal resolution on the specification of a z–r relationship. *J. Atmos. Oceanic Technol.*, **26** (7), 1302–1314, doi:10.1175/2009JTECHA1161.1.
- Marshall, J. S., W. Hitschfeld, and K. L. S. Gunn, 1955: Advances in radar weather. *Adv. Geophys.*, **2**, 1–56.
- Marshall, J. S. and W. M. Palmer, 1948: The distribution of raindrops with size. *J. Meteor.*, **5**, 165–166.
- Matheron, G., 1965: *Les variables régionalisées et leur estimation*. Masson et Cie, Paris, 305 pp.
- Matrosov, S. Y., C. Campbell, D. Kingsmill, and E. Sukovich, 2009: Assessing snowfall rates from x-band radar reflectivity measurements. *J. Atmos. Oceanic Technol.*, **26** (11), 2324–2339.

Bibliography

- Messer, H., A. Zinevich, and P. Alpert, 2006: Environmental monitoring by wireless communication networks. *Science*, **312**, 713, doi:10.1126/science.1120034.
- Michaelides, S., V. Levizzani, E. Anagnostou, P. Bauer, T. Kasparis, and J. Lane, 2009: Precipitation: Measurement, remote sensing, climatology and modeling. *Atmos. Res.*, **94**, 512–533, doi:10.1016/j.atmosres.2009.08.017.
- Milly, P. C. D., R. T. Wetherald, K. A. Dunne, and T. L. Delworth, 2002: Increasing risk of great floods in a changing climate. *Nature*, **415**, 514–517, doi:10.1038/415514a.
- Miriovsky, B., et al., 2004: An experimental study of small-scale variability of radar reflectivity using disdrometer observations. *J. Appl. Meteor.*, **43** (1), 106–118.
- Mishchenko, M. I., L. D. Travis, and D. W. Mackowski, 1996: T-matrix computations of light scattering by nonspherical particles: A review. *J. Quant. Spectrosc. Radiat. Transfer*, **55** (5), 535–575.
- Morin, E., W. F. Krajewski, D. C. Goodrich, X. G. Gao, and S. Sorooshian, 2003: Estimating rainfall intensities from weather radar data: the scale-dependency problem. *J. Hydrometeorol.*, **4** (5), 782–797.
- Nanko, K., Y. Onda, A. Ito, S. Ito, S. Mizugaki, and H. Moriwaki, 2010: Variability of surface runoff generation and infiltration rate under a tree canopy: indoor rainfall experiment using Japanese cypress (*Chamaecyparis obtusa*). *Hydrol. Processes*, **24** (5), 567–575.
- Nystuen, J. A., 2001: Listening to raindrops from underwater: An acoustic disdrometer. *J. Atmos. Oceanic Technol.*, **18**, 1640–1657, doi:10.1175/1520-0426(2001)018<1640:LTRFUA>2.0.CO;2.
- Orlanski, I., 1975: A rational subdivision of scales for atmospheric processes. *Bull. Amer. Meteor. Soc.*, **56**, 527–530.
- Pebesma, E. J., 2004: Multivariate geostatistics in S: the gstat package. *Comput. Geosci.*, **30** (7), 683–691, doi:10.1016/j.cageo.2004.03.012.
- Peters, G., B. Fisher, H. Münster, M. Clemens, and A. Wagner, 2005: Profiles of raindrop size distributions as retrieved by Microrain Radars. *J. Appl. Meteor.*, **44** (12), 1930–1949.
- Prat, O. P. and A. P. Barros, 2009: Exploring the transient behavior of Z-R relationships: Implications for radar rainfall estimation. *J. Appl. Meteor. Climate*, **48** (10), 2127–2143, doi:10.1175/2009JAMC2165.1.
- Pruppacher, H. R. and R. L. Klett, 1997: *Microphysics of clouds and precipitation*. 2d ed., No. 18 in Atmospheric and Oceanographic Sciences Library, Kluwer Academic Press, 954 pp.
- R Development Core Team, 2011: *R: A Language and Environment for Statistical Computing*. Vienna, Austria, R Foundation for Statistical Computing, URL <http://www.R-project.org>, ISBN 3-900051-07-0.

- Rahimi, A. R., G. J. G. Upton, A. R. Holt, and R. J. Cummings, 2003: Use of dual-frequency microwave links for measuring path-averaged rainfall. *J. Geophys. Res.*, **108** (D15), 4467, doi:10.1029/2002JD003202.
- Ramanathan, V., P. J. Crutzen, J. T. Kiehl, and D. Rosenfeld, 2001: Aerosols, climate, and the hydrological cycle. *Science*, **294** (5549), 2119–2124, doi:10.1126/science.1064034.
- Roe, G. H., 2005: Orographic precipitation. *Ann. Rev. Earth Planet Sci.*, **33**, 645–671.
- Rosenfeld, D., 2000: Suppression of rain and snow by urban and industrial air pollution. *Science*, **287**, 1793–1796, doi:10.1126/science.287.5459.1793.
- Rosenfeld, D., U. Lohmann, G. B. Raga, C. D. O’Dowd, M. Kulmala, S. Fuzzi, A. Reissell, and M. O. Andreae, 2008: Flood or drought: how do aerosols affect precipitation? *Science*, **321** (5894), 1309–1313, doi:10.1126/science.1160606.
- Ryzhkov, A. V., T. J. Schuur, D. W. Burgess, P. L. Heinselman, S. E. Giangrande, and D. S. Zrnic, 2005: The joint polarization experiment, polarimetric rainfall measurements and hydrometeor classification. *Bull. Amer. Meteor. Soc.*, **86** (6), 809–824, doi:DOI:10.1175/BAMS-86-6-809.
- Salles, C. and J. D. Creutin, 2003: Instrumental uncertainties in z-r relationships and raindrops fall velocities. *J. Appl. Meteor.*, **42** (2), 279–290.
- Salles, C., J. Poesen, and D. Sempere-Torres, 2002: Kinetic energy of rain and its functional relationship with intensity. *J. Hydrol.*, **257** (1-4), 256–270.
- Schleiss, M. and A. Berne, 2010: Identification of dry and rainy periods using telecommunication microwave links. *IEEE Geosci. Remote Sens. Lett.*, **7** (3), 611–615, doi:10.1109/LGRS.2010.2043052.
- Schleiss, M., A. Berne, and R. Uijlenhoet, 2009: Geostatistical simulation of 2d fields of raindrop size distributions at the meso- γ scale. *Water Resour. Res.*, **45**, W07415, doi:10.1029/2008WR007545.
- Schleiss, M., J. Jaffrain, and A. Berne, 2011: Stochastic Simulation of Intermittent DSD Fields in Time. *J. Hydrometeor.*, doi:10.1175/JHM-D-11-018.1, in press.
- Sevruk, B., M. Ondrás, and B. Chvíla, 2009: The WMO precipitation measurement intercomparisons. *Atmos. Res.*, **92** (3), 376–380, doi:10.1016/j.atmosres.2009.01.016.
- Sheppard, B. E., 1990: Measurement of raindrop size distributions using a small Doppler radar. *J. Atmos. Oceanic Technol.*, **7** (2), 255–268.
- Sheppard, B. E. and P. I. Joe, 1994: Comparison of raindrop size distribution measurements by a joss-waldvogel disdrometer, a pms 2dg spectrometer, and a poss doppler radar. *J. Atmos. Oceanic Technol.*, **11** (4), 874–887.

Bibliography

- Sieck, L. C., S. J. Burges, and M. Steiner, 2007: Challenges in obtaining reliable measurements of point rainfall. *Water Resour. Res.*, **43** (W01420), 1–23, doi:10.1029/2005WR004519.
- Smith, J. A. and W. F. Krajewski, 1993: A modeling study of rainfall rate-reflectivity relationships. *Water Resour. Res.*, **29** (8), 2505–2514.
- Smith, P. L. and D. V. Kliche, 2005: The bias in moment estimators for parameters of drop size distribution functions: sampling from the exponential distributions. *J. Appl. Meteor.*, **44** (8), 1195–1205, doi:10.1175/JAM2258.1.
- Smith, P. L., Z. Liu, and J. Joss, 1993: A study of sampling-variability effects in raindrop size observations. *J. Appl. Meteor.*, **32**, 1259–1269.
- Stedinger, J. R., 1981: Estimating Correlations in Multivariate Streamflow Models. *Water Resour. Res.*, **17** (1), 200–208.
- Steiner, M., T. L. Bell, Y. Zhang, and E. F. Wood, 2003: Comparison of two methods for estimating the sampling-related uncertainty of satellite rainfall averages based on a large radar dataset. *J. Climate*, **16** (22), 3759–3778.
- Steiner, M. and J. A. Smith, 2004: Scale dependence of radar-rainfall rates - an assessment based on raindrop spectra. *J. Hydrometeorol.*, **5** (6), 1171–1180, doi:10.1175/JHM-383.1.
- Steiner, M., J. A. Smith, S. J. Burges, C. V. Alonso, and R. W. Darden, 1999: Effect of bias adjustment and rain gauge data quality control on radar rainfall estimation. *Water Resour. Res.*, **35** (8), 2487–2503.
- Steiner, M., J. A. Smith, and R. Uijlenhoet, 2004: A Microphysical interpretation of Radar Reflectivity-Rain Rate relationship. *J. Atmos. Sci.*, **61** (10), 1114–1131, doi:10.1175/1520-0469(2004)061<1114:AMIORR>2.0.CO;2.
- Stuart, A. and J. K. Ord, 1994: *Kendall's advanced theory of statistics*, Vol. 1. Sixth ed., Arnold & Oxford University press Inc., London, 676 pp.
- Sun, Y., S. Solomon, A. Dai, and R. W. Portmann, 2005: How often does it rain? *J. Climate*, **19** (6), 916–934, doi:10.1175/JCLI3672.1.
- Tapiador, F. J., R. Checa, and M. De Castro, 2010: An experiment to measure the spatial variability of rain drop size distribution using sixteen laser disdrometers. *Geophys. Res. Lett.*, **37**, L16803, doi:10.1029/2010GL044120.
- Testik, F. Y. and A. P. Barros, 2007: Toward elucidating the microstructure of warm rainfall: a survey. *Rev. Geophys.*, **45** (2), doi:10.1029/2005RG000182.
- Thurai, M. and V. N. Bringi, 2005: Drop axis ratios from a 2D video disdrometer. *J. Atmos. Oceanic Technol.*, **22** (7), 966–978, doi:10.1175/JTECH1767.1.

- Thurai, M. and V. N. Bringi, 2008: Rain microstructure from polarimetric radar and advanced disdrometers. *Precipitation: Advances in Measurement, Estimation and Prediction*, Springer, 233–284.
- Thurai, M., G. J. Huang, V. N. Bringi, W. L. Randeu, and M. Schönhuber, 2007: Drop shapes, model comparisons, and calculations of polarimetric radar parameters in rain. *J. Atmos. Oceanic Technol.*, **24** (6), 1009–1032, doi:10.1175/JTECH2051.1.
- Tokay, A. and P. G. Bashor, 2010: An experimental study of small-scale variability of raindrop size distribution. *J. Appl. Meteor. Climate*, **49** (11), 2348–2365, doi:10.1175/2010JAMC2269.1.
- Tokay, A., P. G. Bashor, and V. L. McDowell, 2010: Comparison of rain gauge measurements in the mid-atlantic region. *J. Hydrometeorol.*, **11** (2), 553–565, doi:10.1175/2009JHM1137.1.
- Tokay, A., P. G. Bashor, and K. R. Wolff, 2005: Error characteristics of rainfall measurements by collocated Joss-Waldvogel disdrometers. *J. Atmos. Oceanic Technol.*, **22** (5), 513–527.
- Tokay, A., A. Kruger, and W. F. Krajewski, 2001: Comparison of drop size distribution measurements by impact and optical disdrometers. *J. Appl. Meteor.*, **40** (11), 2083–2097.
- Tokay, A. and D. A. Short, 1996: Evidence from tropical raindrop spectra of the origin of rain from stratiform versus convective clouds. *J. Appl. Meteor.*, **35** (3), 355–371.
- Tokay, A., D. B. Wolff, K. R. Wolff, and P. Bashor, 2003: Rain gauge and disdrometer measurements during the keys area microphysics project (kamp). *J. Atmos. Oceanic Technol.*, **20** (11), 1460–1477.
- Tokay, A., et al., 2007: Disdrometer derived Z-S relations in south central ontario, canada. 33rd *Int. Conf. On Radar Meteorology*, AMS, Cairns, Australia.
- Trenberth, K. E., A. Dai, R. M. Rasmussen, and D. B. Parsons, 2003: The changing character of precipitation. *Bull. Amer. Meteor. Soc.*, **84** (9), 1205–1217, doi:10.1175/BAMS-84-9-1205.
- Trenberth, K. E., et al., 2007: Observations: Surface and atmospheric climate change. *Climate Change 2007: The Physical Science Basis. Contribution of Working Group I to the Fourth Assessment Report of the Intergovernmental Panel on Climate Change*, S. Solomon, D. Qin, M. Manning, Z. Chen, M. Marquis, K. B. Averyt, M. Tignor, and H. L. Miller, Eds., Cambridge University Press, Cambridge, UK and New York, USA.
- Uijlenhoet, R., 2001: Raindrop size distributions and radar reflectivity-rain rate relationships for radar hydrology. *Hydrol. Earth Syst. Sci.*, **5** (4), 615–627.
- Uijlenhoet, R., J. M. Porrà, D. Sempere Torres, and J.-D. Creutin, 2006: Analytical solutions to sampling effects in drop size distribution measurements during stationary rainfall: estimation of bulk rainfall variables. *J. Hydrol.*, **328**, 65–82, doi:10.1016/j.jhydrol.2005.11.043.

Bibliography

- Uijlenhoet, R., J. A. Smith, and M. Steiner, 2003a: The microphysical structure of extreme precipitation as inferred from ground-based raindrop spectra. *J. Atmos. Sci.*, **60** (10), 1220–1238.
- Uijlenhoet, R., M. Steiner, and J. A. Smith, 2003b: Variability of raindrop size distributions in a squall line and implications for radar rainfall estimation. *J. Hydrometeor.*, **44** (4), 43–61.
- Ulbrich, C. W., 1983: Natural variations in the analytical form of the raindrop-size distribution. *J. Climate Appl. Meteor.*, **22** (10), 1764–1775.
- Upton, G. J. G., A. R. Holt, R. J. Cummings, A. R. Rahimi, and J. W. F. Goddard, 2005: Microwave links: the future for urban rainfall measurements? *Atmos. Res.*, **77** (1-4), 300–312.
- Villarini, G., P. V. Mandapaka, W. F. Krajewski, and R. J. Moore, 2008: Rainfall and sampling uncertainties: A rain gauge perspective. *J. Geophys. Res.*, **113** (D11102), doi:10.1029/2007JD009214.
- Vörösmarty, C. J., P. Green, J. Salisbury, and R. B. Lammers, 2000: Global water resources: Vulnerability from climate change and population growth. *Science*, **289** (5477), doi:10.1126/science.289.5477.284.
- Vuerich, E., C. Monesi, L. Lanza, L. Stagi, and E. Lanzinger, 2009: WMO Field intercomparison of rainfall intensity gauges. INSTRUMENTS AND OBSERVING METHODS 99, World Meteorological Organization, Geneva.
- Wetherald, R. T. and S. Manabe, 2002: Simulation of hydrologic changes associated with global warming. *J. Geophys. Res.*, **107** (D19), doi:10.1029/2001JD001195.
- Whitehead, P. G., R. L. Wilby, R. W. Battarbee, M. Kernan, and A. J. Wade, 2009: A review of the potential impacts of climate change on surface water quality. *Hydrol. Sci. J.*, **54** (1), 101–123.
- Willis, P. T., 1984: Functional fits to some observed drop size distributions and parameterization of rain. *J. Atmos. Sci.*, **41** (9), 1648–1661.
- WMO, 2008: *Guide to Meteorological Instruments and Methods of Observation*. 7th ed., WMO-No.08, World Meteorological Organization, Geneva, 681 pp., available at: http://www.wmo.int/pages/prog/www/IMOP/publications/CIMO-Guide/CIMO_Guide-7th_Edition-2008.html.
- Yuter, S. E., D. E. Kingsmill, L. B. Nance, and M. Löffler-Mang, 2006: Observations of precipitation size and fall speed characteristics within coexisting rain and wet snow. *J. Appl. Meteor. Climate*, **45** (10), 1450–1464.

Joël JAFFRAIN

Environmental Eng.

route d'Oron 19
1041 Poliez-Pittet

+41 (0)78 805 12 57

✉ joel.jaffrain@gmail.com

<http://people.epfl.ch/joel.jaffrain>



Personal information

Age 28
Nationality French

Skills

general

- Project manager (conception, administrative and financial tasks)
- Management of network of instruments (instrument deployment and maintenance) and data acquisition (transmission and storage)
- Skills in the search of innovative solutions
- Information synthesis, technical reports
- Results diffusion and popularization: international conferences, teaching, interview
- Objective and critical analysis of documents (reports, scientific papers)
- Autonomous working and ease of integration within a team

specific

- Geology, hydrology and hydrogeology
- Analyses of meteorological and climate data
- Statistical analyses, Geostatistics (spatial analyses)

computer

Platform	Linux, Windows, MacOSX	Programming	R, shell, matlab, C++
Web	html, php, MySQL	GIS	ArcGIS, QuantumGIS
Office	Microsoft Office, OpenOffice, LaTeX	Proj. manag.	GanttProject, OpenProj

Experience

Vocational

2007–present **PhD**, EPFL-LTE, Lausanne, Switzerland.
Project manager, international conference, manager of various instruments data, statistical and geostatistical analyses, reviewer for technical and scientific reports.

2007–present **Teaching Assistant**, EPFL-LTE, Lausanne, Switzerland.
Teaching assistant for the Geostatistical course (M.Sc) of Prof. A. Berne: help during exercise sessions, correction of exercise sessions.

Miscellaneous

2009–present **Bike mechanic**, Sport-XX, Slow-Up.
Bike mechanic during sports events promoting gentle mobility (Slow-Up).

2001–2006 **Various student jobs**.
Agri-food worker, truck loading, walls demolition, ...

Education

- 2007–present **PhD in Environment**, *École Polytechnique Fédérale de Lausanne*, Lausanne, Switzerland.
PhD student in the Environmental Remote Sensing Lab. (LTE)
- 2007 **M.Sc. thesis**, *Institut de Recherche pour le Développement (IRD) - GREAT-ICE lab.*, Maison des Sciences de l'Eau, Montpellier, France.
Climatic and statistical analyses of a 100-year rainfall data set from South America, trends detection.
- 2005–2007 **M.Sc. in Water and Environment**, *Université des Sciences et Techniques du Languedoc*, Montpellier, France.
Skills in hydro(geo)logy, environmental (geo)chemistry, management of water resources, water treatment.
- 2002–2005 **Bachelor in Geology**, *Université Henri-Poincaré*, Nancy, France.
Skills in seismic, petrographic analyses, palaeontology, mineralogy, tectonic.

Publications

- 2011 J. Jaffrain, A. Studzinski and A. Berne, "A network of disdrometers to quantify the small-scale variability of the raindrop size distribution", *Water Resour. Res.*, 47, 2011.
- 2011 J. Jaffrain and A. Berne, "Experimental quantification of the sampling uncertainty associated with measurements from Parsivel disdrometers", *J. Hydrometeor.*, 12(3), 2011.
- 2011 M. Schleiss, J. Jaffrain and A. Berne, "Statistical analysis of rainfall intermittency at small spatial and temporal scales", *Geophys. Res. Lett.*, 38, 2011.
- In press J. Jaffrain and A. Berne, "Quantification of the small-scale spatial structure of the raindrop size distribution from a network of disdrometers", *J. Appl. Meteor. Climate*.
- In press M. Schleiss, J. Jaffrain and A. Berne, "Stochastic Simulation of Intermittent DSD Fields in Time", *J. Hydrometeor.*.
- In press A. Berne, J. Jaffrain and M. Schleiss, "Scaling analysis of the variability of the rain drop size distribution at small scale", *Adv. Water Resour.*.
- In revision J. Jaffrain and A. Berne, "Influence of the subgrid variability of the raindrop size distribution on radar rainfall estimators", *J. Appl. Meteor. Climate*, submitted in August 2011.

Academic activities

Scientific papers

- 2011-present **Reviewer** for *Journal of Hydrometeorology*.

Conferences as presenting author

- 2011 35th AMS Conference on Radar Meteorology, Pittsburgh (PA), USA, 26-30 Sept 2011.
- 2010 6th European Conference on Radar in Meteorology and Hydrology (ERAD), Sibiu, Romania, 6-10 Sept 2010.
- 2010 10th International Precipitation Conference (IPC), Coimbra, Portugal, 23-25 June 2010.
- 2009 34th AMS Conference on Radar Meteorology, Williamsburg (VA), USA, 5-9 Oct 2009.
- 2009 European Geosciences Union congress (EGU), Vienna, Austria, 5-9 Apr 2009.
- 2008 5th European Conference on Radar in Meteorology and Hydrology (ERAD), Helsinki, Finland, June 2008.

Awards

- 2011 Runner up for the **Spiros G. Geotis Prize** during the *35th AMS Conference on Radar Meteorology*, Pittsburgh (PA), USA, 26-30 Sept 2011.
Prize for the best student paper.

Languages

French	Native	
English	Fluent	<i>working language since 2007</i>
Portuguese	A1 Level	<i>in progress</i>
German	Basic knowledges	

Interests

Activities	Do-it-yourself, gardening, mechanic, electronic.
Sports	Running, badminton, climbing, tennis.
Music	Playing guitar.
Nature	Hiking, promenade, mountain bike.
Community life	5 years in the organizing comity of the Tennis club of Albestroff (France).